

Copyright
by
Todd Charles Monson
2012

The Dissertation Committee for Todd Charles Monson Certifies that this is the approved version of the following dissertation:

Study of Anomalous Behavior in Solution Synthesized Iron Nanoparticles

Committee:

James L. Erskine, Supervisor

Dale L. Huber, Co-Supervisor

Alexander A. Demkov

Zhen Yao

Maxim Tsoi

Llewellyn K. Rabenberg

**Study of Anomalous Behavior in Solution Synthesized Iron
Nanoparticles**

by

Todd Charles Monson, B.S.; M.A.

Dissertation

Presented to the Faculty of the Graduate School of

The University of Texas at Austin

in Partial Fulfillment

of the Requirements

for the Degree of

Doctor of Philosophy

The University of Texas at Austin

May 2012

Dedication

To my son Caleb who I look forward to meeting very soon.

Acknowledgements

It would not have been possible for me to complete this dissertation without the support and guidance of so many individuals far too numerous to mention. I am sincerely grateful for all the friendships and interactions I have had along this journey which has been spread out over a significant portion of my short time here on earth. Here, I give thanks to some of the most memorable relationships along the way.

First, I am very grateful for my parents, who instilled in me the importance of always doing my best and the value of education and knowledge. Also, I cannot imagine completing this dissertation without my wife Judy, who has been a wonderful friend and companion along this journey which has become intertwined into the rest of our lives.

I could not have made it through all of the required coursework without many of my fellow physicists who helped me along the way. These friends and colleagues include Parrish Brady, Brian Gentry, Ben Holder, Casey Israel, Samantha Moore, and Iyad Dajani. In addition to spending hours working on physics together, I particularly enjoyed the times when our conversations ventured extremely far from physics. It would be impossible to forget my good friend, Rudy Casals, who worked alongside me while we were completing our undergraduate degrees in physics at the Naval Academy so many years ago. Rudy's energy continues to inspire me today.

I am sincerely grateful to my colleagues at Sandia National Labs who have made this endeavor possible. My manager, Diane Peebles, was instrumental in ensuring that I could complete this dissertation while a member of the technical staff at Sandia. Dale Huber provided much mentorship and guidance in addition to serving as a member of my committee. Other friends and colleagues including Gene Venturini, Jim O'Brien, Paula

Provencio, Ben Frankamp, Judi Lavin, Peter Sharma, Mark Rodriguez, Tyler Stevens, Jean Leger, and Paul Klimov provided much help along the way.

The 2009 Advanced Photon Source XAFS School was extremely helpful in teaching me how to prepare for XAFS experiments and complete XAFS data analysis. This course introduced me to Qing Ma, a beamline scientist at the Advanced Photon Source (APS) who proved invaluable in helping me with my XAFS experiments. Other APS staff and users, including Yang Ren and Valeri Petkov, were also extremely helpful

Finally, I am of course grateful for my advisor, James Erskine, who served as my mentor both while pursuing my M.A. while I was still in the Air Force and now during the completion of my doctoral studies.

Sandia National Laboratories is a multi-program laboratory managed and operated by Sandia Corporation, a wholly owned subsidiary of Lockheed Martin Corporation, for the U.S. Department of Energy's National Nuclear Security Administration under contract DE-AC04-94AL85000. This research was supported by the U.S. Department of Energy, Office of Basic Energy Sciences, Division of Materials Sciences and Engineering.

TODD CHARLES MONSON

The University of Texas at Austin

May 2012

Study of Anomalous Behavior in Solution Synthesized Iron Nanoparticles

Publication No. _____

Todd Charles Monson, Ph.D.

The University of Texas at Austin, 2012

Supervisors: James Erskine and Dale Huber

The magnetic and physical properties of oxide-free, ligand passivated, iron nanoparticles were studied using superconducting quantum interference device (SQUID) magnetometry and synchrotron based X-ray radiation. Particles used for this study ranged in diameter between 2 and 10 nm, which made it possible to distinguish between bulk and surface effects in the nanoparticles' properties. Additionally, the effects of two different weakly interacting ligands (2,4-pentanedione and hexaethylene glycol monododecylether) on the nanoparticles' behavior were studied. The results of this study were compared to theoretical predictions of magnetic transition metal behavior in both thin films and nanoparticles, as well as experimental results from measurements of transition metal clusters formed in an inert carrier gas and measured with a Stern-Gerlach magnet.

Magnetometry revealed that the iron nanoparticles have a magnetocrystalline anisotropy an order of magnitude greater than bulk iron. At the same time, these particles exhibit a saturation mass magnetization (σ_{sat}) up to 209 Am²/kg, which is only slightly lower than bulk iron. The structural properties of these particles were characterized using

high energy X-ray diffraction analyzed using the atomic pair distribution function method (PDF). The PDF analysis indicates that the Fe particles have a distorted and expanded form of the bcc lattice, which could, at least in part, explain the magnetocrystalline anisotropy of these nanoparticles. X-ray absorption fine structure (XAFS) was used to study the surface properties of the iron nanoparticles and further characterize their structural properties. XAFS showed that oxidized species of iron exist at the nanoparticles' surface and can be attributed to iron/ligand interactions. The percentage of oxidized species scales with the surface to volume ratio of the nanoparticles, and therefore appears limited to the nanoparticle surface. The layer of Fe(II) species present at the nanoparticles' surface accounts for the reduction in σ_{sat} values (when compared to bulk iron) observed in these particles. XAFS analysis also provided further confirmation of the nanoparticles' expanded crystalline lattice.

Table of Contents

List of Tables	xi
List of Figures	xii
Chapter 1 Introduction	1
Chapter 2 Nanoparticle Magnetism	7
2.1 Single Domain Magnetic Particles.....	8
2.2 Superparamagnetism.....	9
2.3 Magnetocrystalline Anisotropy.....	14
2.4 Magnetic Nanoparticle and Thin Film Literature Results to Date.....	17
2.4.1 Solution Synthesized Magnetic Nanoparticles	18
2.4.2 Surfactant Free Magnetic Nanoparticle Beams	20
2.4.3 Epitaxial Fe Thin Films	22
2.4.3 Ab Initio Modeling Results.....	23
Chapter 3 Solution Based Synthesis of Magnetic Nanoparticles.....	25
3.1 Introduction to Solution Based Nanoparticle Synthesis	25
3.2 Synthesis of Iron Nanoparticles	26
3.3 TEM Characterization.....	28
3.3.1 Sample Preparation	28
3.3.2 Results and Size Analysis	29
Chapter 4 Magnetic Characterization of Magnetic Nanoparticles.....	36
4.1 Introduction to Magnetometry	36
4.1.1 SQUID Magnetometry.....	36
4.1.2 Magnetic Measurements of Superparamagnetic Nanoparticles..	41
4.2 Magnetic Characterization of Fe Nanoparticles	45
4.2.1 Sample Preparation and Mounting.....	45
4.2.2 DC Magnetic Characterization	46
4.2.3 AC Magnetic Characterization	50

Chapter 5 Synchrotron X-ray Characterization of Iron Nanoparticles	59
5.1 Introduction to Synchrotron Radiation	59
5.2 High Energy XRD and PDF Experiments	63
5.2.1 Sample and Data Handling	65
5.2.2 Experimental Results	66
5.3 XAFS Experiments	69
5.3.1 Sample Preparation	74
5.3.2 XANES Experimental Results	79
5.3.3 Fourier Transform Infrared Spectroscopy (FT-IR) Complimentary Results	85
5.3.4 EXAFS Experimental Results	87
Chapter 6 Conclusion	94
Bibliography	101
Vita	109

List of Tables

Table 2.1:	Magnetic properties, their symbols, and SI units. From Ref.[40].....	7
Table 4.1:	Fitted parameters for both the Néel-Brown and spin-glass power-law models along with values of Φ evaluated about $f = 30$ Hz.	55
Table 4.2:	Parameters determined through fitting AC magnetometry data with the Vogel-Fulcher law.	58
Table 5.1:	Results from modeling PDF X-ray diffraction data of one bulk and two nanoparticle iron samples. The two nanoparticle samples are labeled according their diameter.	68
Table 5.2:	Details of the iron nanoparticle samples studied with XAFS.	75
Table 5.3:	XANES LCF fitting results (fitting results given in %).	82
Table 5.4:	EXAFS fitting results.	91
Table 5.5:	Additional EXAFS fitting results not included in Table 5.4. E_0 for both Fe and FeO theoretical standards was 7112 eV prior to fitting. R factor provides a measure of closeness of fit with a value of zero indicating a perfect match between data and fit.	93

List of Figures

Figure 1.1: Photomicrograph of U937 leukemia cells with CD34-conjugated magnetite nanoparticles bound to the cells. The iron in the particles is made visible in the photomicrograph through Prussian blue staining.[14]	2
Figure 2.1: The stray magnetic field near spherical particles. (a) The stray field of a single domain particle. (b) Through the creation of domain walls, the stray field of a multi-domain particle is reduced greatly, however energy must be expended in the creation of domain walls. Adapted from Refs.[25, 46] Stray field lines were generated by Vizimag 3.0.[47] .9	9
Figure 2.2: The function of equation (2.2) plotted for $mH = 0.15KV$. From Ref.[56]	11
Figure 2.3: The coercivity of an ensemble of magnetic nanoparticles held at a fixed temperature and as a function of particle diameter. Adapted from Ref.[18]	13
Figure 2.4 A pair of spins. Adapted from Ref.[57]	15
Figure 2.5: Equivalent directions in a cubic crystal. From Ref.[57]	16
Figure 2.6: Plots of magnetization vs. applied field for a sample of iron taken along three different crystallographic directions. From Ref.[18]	17
Figure 2.7: Magnetic moment for Ni, Co, and Fe surfactant free particle beams as a function of number of atoms per particle. The spin imbalance per atom is indicated on the right scale. From Ref.[36]	21

Figure 2.8: Ratio of the average moment per atom to the bulk value ($2.22\mu_B$) as a function of film thickness for 2.9, 3.5, and 4.4 ML Fe(100)/Ag(100) films. The solid line is a fit which assumes that all of the moment enhancement occurs in the interface layers. From Ref.[61]	22
Figure 2.9: Qualitative model showing the evolution of the spin density of states for iron from the atom through the bulk via a low coordination environment. The symbol Δ stands for the exchange energy. From Ref.[36]	24
Figure 3.1: Schematic of a Schlenk line used for air-free chemistry. From Ref.[74]	25
Figure 3.2: Inert gas glovebox manufactured by Innovative Technologies, Inc.[75]	26
Figure 3.3: Chemical structure of ligands used for iron nanoparticles: 2,4-pentandione and hexaethylene glycol monodoecylether.....	28
Figure 3.4: TEM image of Fe nanoparticles synthesized with a $\text{Fe}(\text{CO})_5$:C12E6 ratio of 1:1. The inset is a histogram of the distribution of particle diameters determined by analyzing over 300 particles.	31
Figure 3.5: TEM image of Fe nanoparticles synthesized with a $\text{Fe}(\text{CO})_5$:C12E6 ratio of 11:1. The inset is a histogram of the distribution of particle diameters determined by analyzing over 300 particles.	32
Figure 3.6: TEM image of Fe nanoparticles synthesized with a $\text{Fe}(\text{CO})_5$:PD ratio of 13:1. The inset is a histogram of the distribution of particle diameters determined by analyzing over 300 particles.	33
Figure 3.7: TEM image of Fe nanoparticles synthesized with a $\text{Fe}(\text{CO})_5$:PD ratio of 35:1. The inset is a histogram of the distribution of particle diameters determined by analyzing over 300 particles.	34

Figure 3.8: Plot of the volume average diameter as a function of the iron pentacarbonyl to ligand ratio for iron nanoparticles synthesized with pentanedione (PD) and hexaethylene glycol monododecylether (C12E6) surfactants.	35
Figure 4.1: Second-order gradiometer used inside the Quantum Design MPMS. From Ref.[82]	38
Figure 4.2: Layout of the major components of the Quantum Design MPMS surrounding the sample space. From Ref.[82]	39
Figure 4.3: Signal generated from a magnetic nanoparticle sample being pulled through the second-order gradiometer pick-up coils of a MPMS (red solid line). A linear regression fit of the theoretical signal of a dipole moving through the second-order gradiometer is displayed as a blue dashed line.	41
Figure 4.4: (a) M(H) response of a ferrite nanoparticle sample below its T_B , where it exhibits hysteresis. The saturation magnetization, remanance magnetization, and coercive field are all labeled. (b) M(H) response for the same sample above T_B . The sample's initial susceptibility and saturation magnetization are labeled.....	43
Figure 4.5: The M(T) response of an ensemble of single domain iron nanoparticles. The blocking temperature is the peak in the ZFC data.	45
Figure 4.6: Mass magnetization curve of an ensemble of iron nanoparticles with a volume average diameter of 5 nm determined through transmission electron microscopy (TEM). Based on the determination of the mass of Fe in this sample we estimate the σ_{sat} of the sample (at 5 K) to be 209 Am ² /kg.	47

Figure 4.7: ZFC curves measured using DC magnetometry for nanoparticles with diameters of 2.3, 3.1, 3.4, and 4.5 nm. The moments for each curve are normalized for ease of comparison.....	49
Figure 4.8: Plot of T_B vs. particle diameter for a series of Fe nanoparticles of different sizes. A dashed line of blocking temperatures resulting from a constant K_1 and $\tau_0=10^{-10}$ s is co-plotted with measured values of T_B and provided as a guide. These blocking temperatures are compared to a curve (solid blue line) displaying what theory would predict for bcc Fe nanoparticles assuming a measurement time (τ) of 100 s, a value of $\tau_0=10^{-10}$ s, and the bulk value of K_1 for bcc iron.....	50
Figure 4.9: Real (a) and imaginary (b) AC magnetic susceptibilities (χ) of a 2.3 nm diameter iron nanoparticle sample. Data were also collected at 0.3, 3, 30, and 300 Hz but are not displayed.....	52
Figure 4.10: Plot of the natural logarithm of the relaxation time (τ) vs. $1/T_B$ for a 3.1 nm diameter iron nanoparticle sample. The data are fit with the Néel-Brown model described by Eq. (4.2) (dashed line) and the Vogel-Fulcher law described by Eq. (4.5) (solid line).....	54
Figure 5.1: Electro-magnets used in electron storage rings. A complete magnet assembly from the Stanford Synchrotron Light Source (SSRL) is displayed on the bottom right. From Ref.[92]	60
Figure 5.2: The radiation pattern of an accelerated charge in the rest frame of the charge (left) and in the frame of an observer (right). From Ref.[92].....	61
Figure 5.3: Diagram of a storage ring sector at APS. From Ref.[93].....	63
Figure 5.4: The geometry of a diffraction experiment showing the wave vector \mathbf{Q} and the scattering angle, 2θ . From Ref.[95]	64

Figure 5.5: Plot of XRD data collected on a laboratory diffractometer. The data merges low Q data from a Cu target with high Q data from a Mo target.	67
Figure 5.6: Experimental atomic PDF for a micron sized (bulk) iron sample and two iron nanoparticle samples. Model PDFs are displayed as a dashed black line.....	68
Figure 5.7: The X-ray absorption spectrum of NiO with the XANES region, EXAFS region, and white line noted. From Ref.[102].....	70
Figure 5.8: Illustration of the X-ray absorption process using data from a NiO sample. From Ref. [102].....	72
Figure 5.9: Plot of XAFS spectrum for a FeO sample. $\mu(E)$ is shown with a smooth background function $\mu_0(E)$ and the edge-step $\Delta\mu(E_0)$. From Ref.[100]	73
Figure 5.10: Photograph of XAFS experimental setup. The X-ray beampath and path from the sample to the fluorescence detector are shown in the inset photograph.	77
Figure 5.11: Close in photograph of iron nanoparticle sample mounting used for XAFS experiments.....	78
Figure 5.12: XANES spectra of sample PD-13to1. Also displayed are the linear combination fitting (LCF) results along with the reference spectra used to produce the fit (scaled according to their contribution to the fit). 80	
Figure 5.13: XANES spectra of sample PD-35to1. Also displayed are the linear combination fitting (LCF) results along with the reference spectra used to produce the fit (scaled according to their contribution to the fit). 81	

Figure 5.14: XANES spectra of sample C12E6-1to1. Also displayed are the linear combination fitting (LCF) results along with the reference spectra used to produce the fit (scaled according to their contribution to the fit).	83
Figure 5.15: XANES spectra of sample C12E6-11to1. Also displayed are the linear combination fitting (LCF) results along with the reference spectra used to produce the fit (scaled according to their contribution to the fit).	84
Figure 5.16: SAED of sample C12E6-1to1. The diffraction rings are labeled with the indices of either Fe ₃ O ₄ or γ -Fe ₂ O ₃ (the difference in lattice plane spacings between magnetite and γ -Fe ₂ O ₃ are indistinguishable within $\pm 0.05 \text{ \AA}$).	85
Figure 5.17: FT-IR spectra of Fe nanoparticles synthesized with PD surfactants and compared to the spectra of Fe(III)acac and PD (neat).	87
Figure 5.18: EXAFS spectra of Fe nanoparticles synthesized with PD surfactants.	88
Figure 5.19: EXAFS spectra of Fe nanoparticles synthesized with C12E6 surfactants.	89
Figure 5.20: Plot of the magnitude of the Fourier transform of the EXAFS spectra (multiplied by k^2) of PD-13to1 (top) and PD-35to1 (bottom). Fits to both spectra are plotted as dashed lines.	89
Figure 5.21: Plot of the magnitude of the Fourier transform of the EXAFS spectra (multiplied by k^2) of C12E6-1to1 (top) and C12E6-11to1 (bottom). The fits to both spectra are plotted as dashed lines.	90
Figure 5.22: EXAFS spectra (multiplied by k^2) of Fe foil (a) and plot of the Fourier transform of the EXAFS spectra of Fe foil (b). In (b) the fit to the Fe foil data is plotted as a dashed line.	92

Figure 6.1: Scaled representation of the core/shell structure in samples PD-35to1
and C12E6-11to197

Chapter 1

Introduction

Although frequently overlooked, iron nanoparticles have properties that make them extremely desirable for a number of high impact applications. Among them are magnetic and electrical applications including ultra-high density magnetic recording media and magnetic random access memory (MRAM).[1-3] Superparamagnetic iron nanoparticles would make excellent materials for transformer cores, electric motors, and other related technologies because of their very high susceptibilities, large magnetic saturations, and lack of eddy current loss when they remain electrically isolated from one another.[1, 4, 5] An area not often discussed is iron nanoparticles' ability to serve as a material for magnetic refrigeration, particularly if sufficient control over their size dependent properties is demonstrated.[6]

One of the most fruitful and quickly growing applications for magnetic nanoparticles is in the area of biomedicine. Frequently, the material of choice for biological applications of magnetic particles is magnetite. However, zero valent iron particles could prove useful because of their higher mass magnetization saturation (σ_{sat}) compared to iron oxides, particularly if their reactive surface can be passivated. These biomedical applications include drug delivery, disease detection, hyperthermia treatment of cancer cells, and MRI contrast enhancement.[1, 7-17] Many of these applications rely on functionalized ligands bound to the surface of the nanoparticles which enable the attachment of antibodies specific to the disease being detected or treated. Understanding how this surface functionalization affects the nanoparticles' magnetic properties is key to the success of these applications. Figure 1.1 shows a photomicrograph of U937 leukemia cells with CD34-conjugated magnetite nanoparticles bound to the cells. CD34 is a stem

cell antigen expressed by several types of human leukemia blast cells. The iron in the particles is made visible in the photomicrograph through Prussian blue staining.

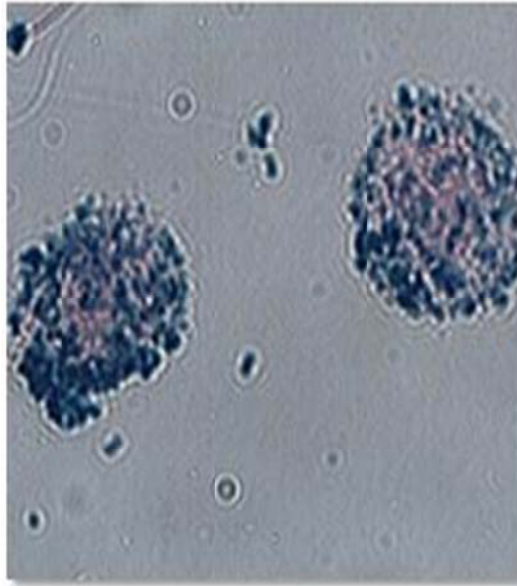


Figure 1.1: Photomicrograph of U937 leukemia cells with CD34-conjugated magnetite nanoparticles bound to the cells. The iron in the particles is made visible in the photomicrograph through Prussian blue staining.[14]

One of iron's most important properties which makes it desirable for many applications is that it has the highest room-temperature σ_{sat} of all the elements.[18, 19] Additionally, because of iron's cubic crystalline structure, it is a soft magnetic material, making it very useful in applications that require low coercivities or superparamagnetic properties over a large range of sizes and temperatures.[18, 19] Iron's low magnetocrystalline anisotropy gives iron nanoparticles lower blocking temperatures (the temperature above which an ensemble of particles behaves superparamagnetically) than other nanoparticles of comparable size. However, iron's key weakness is its reactivity,

particularly in regard to oxygen and water. This reactivity becomes increasingly problematic at the nanoscale, where the surface to volume ratio becomes quite large.

Understanding the differences between nanoparticle and bulk magnetism is a major scientific challenge, particularly when in contact with strongly interacting surfactants. Many phenomena not detected in bulk materials manifest themselves on the nanoscale and have important implications to the harnessing of magnetic nanocomposites in practical applications. Developing an understanding of magnetism in iron nanoparticles, particularly surfactant-coated and chemically-synthesized nanoparticles, is particularly difficult because the iron surface is highly reactive and oxidizes easily. However, understanding the interaction between the iron surface and the organic ligands is imperative for interpreting their magnetic behaviors and future judicious selection of surfactants.

The magnetic properties of solution synthesized iron nanoparticles are further complicated since their syntheses occur at relatively low temperatures (200 °C or less) and they cannot be treated with a high temperature annealing process. These low processing temperatures lead to more disordered materials than found in high quality bulk iron, which is typically annealed at temperatures between 800-1000 °C and cooled slowly back to room temperature.[20] Similarly, thin films of iron grown using molecular beam epitaxy (MBE) in ultra-high vacuum (UHV) produce highly ordered material with a control over the crystalline orientation not possible in solution based nanoparticle syntheses.[21, 22] Although solution synthesis of magnetic particles includes the challenges of low temperature processing and the added complexity of the ligand/surface interaction, it remains one of the best methods for producing high quality magnetic nanoparticles with a narrow size dispersion in quantities sufficient for applications. While organic ligands can affect the magnetism at the surface of the nanoparticles they

are vital in controlling the growth of nanoparticles to within a narrow size distribution, ensuring solubility and dispersion of the particles in a variety of solvents, and providing surface chemistry that allows for the interaction of the particles with other molecules (including targeted pathogens) or the formation of polymer based nanocomposites.

A number of research groups have synthesized high-quality iron nanoparticles, but they typically have an oxide layer present on the surface and/or strongly interacting ligands which produce a nonmagnetic surface layer. As a result, these nanoparticles are reported to have saturation mass magnetizations (σ_{sat}) well below that of bulk iron.[23-27] Some of the early work in iron nanoparticles by both Smith and Wychick and Gedanken and coworkers showed dramatic differences in the magnetizations of iron nanoparticles through the use of different surfactants.[27, 28] Only one recent publication reports σ_{sat} values for small iron nanoparticles that exceed the bulk.[29] These same particles also exhibit an effective anisotropy greater than bulk iron, raising the question as to whether it is possible to control the magnetocrystalline anisotropy of magnetic nanoparticles by varying the synthesis conditions and/or organic surfactants.

The decrease in nanoparticle magnetization compared to bulk materials becomes significantly less pronounced when using the other less reactive transition metals. Nanoparticles of cobalt, nickel, and NiFe have all been synthesized with magnetizations equal to or in some cases exceeding that of their bulk counterparts.[30-34] Even strongly interacting ligands, such as phosphines and carboxylic acids, known to strongly reduce magnetism in iron, did not affect the magnetization of cobalt nanoparticles.[34]

The results observed in solution synthesized iron nanoparticles contrast to those seen in surfactant free transition metal nanoparticle beams generated under UHV conditions.[35-37] Here, iron, cobalt, and nickel nanoparticles' σ_{sat} is shown to increase with decreasing particle diameter. The enhanced magnetization observed in the

surfactant free nanoparticles agrees with experimental results of enhanced magnetization observed in transition metal thin films (measured under UHV conditions) and with ab initio calculations of thin film and nanoparticle magnetism. A summary of the magnetic properties reported in the literature for solution synthesized nanoparticles, surfactant free nanoparticles, and thin films, along with theoretical predictions of magnetization in these systems will be discussed in further detail in Chapter 2. This chapter will also contain a brief review of superparamagnetism and magnetocrystalline anisotropy.

In an attempt to synthesize ligand passivated iron nanoparticles with magnetizations approaching that of bulk iron, chemists at Sandia National Laboratories developed a new synthesis for iron nanoparticles using more weakly interacting ligands than those typically found in the literature.[5] Careful air-free chemistry and sample handling techniques were used due to the reactivity of the iron surface. A description of the particle synthesis, surfactants, and characterization of these particles using transmission electron microscopy can be found in Chapter 3.

The bulk of the scientific effort in this dissertation focused on the characterization of these nanoparticles and the relation of their physical properties to their observed magnetic behavior. Both DC and AC magnetometry were used to study the magnetic properties, including σ_{sat} and magnetocrystalline anisotropy, of these iron nanoparticles. An introduction to magnetometry and the magnetic characterization of our iron nanoparticles are discussed in Chapter 4.

The ligand/surface interaction of the nanoparticles was studied and related to the magnetic properties observed in the nanoparticles. Additionally, the crystalline structure of the nanoparticles and its effect on the particles' magnetic behavior was studied. Due to the nanoparticles' small size and lack of long range order this was not a task that could be accomplished on standard laboratory equipment. The high energies and fluxes of

synchrotron radiation were used to collect and analyze high energy X-ray diffraction (XRD) and X-ray absorption fine structure (XAFS) spectra. The synchrotron based experiments, data analysis, and results are discussed in Chapter 5.

Chapter 2

Nanoparticle Magnetism

Although it has been argued that any particle between 1 and 1000 nm can be considered a nanoparticle[38], this is a rather broad definition. Another case has been made that only particles between 1 and 10 nm in size can be regarded as nanoparticles.[39] A more reasonable definition would be to limit nanoparticles to any particle which is smaller than 40 nm in at least two dimensions, where increasing these dimensions beyond 40 nm would eliminate the unique magnetic, optical, and electronic properties observed at the nanoscale.[25] The particles studied under this research all have a mean sample diameter less than 11 nm and so are well within the nanoscale regime.

Throughout this dissertation SI units will be used for magnetic properties. Table 2.1 lists the magnetic properties seen in the text below, their symbols, and their SI units.

Quantity	Symbol	SI Unit
Volume magnetization	M	Am^{-1}
Mass magnetization	σ	Am^2/kg
Volume susceptibility	χ	dimensionless ^[a]
Mass Susceptibility	χ_p	m^3/kg
Magnetic flux density, magnetic induction	B	T
Magnetic field strength	H	Am^{-1}

[a] Even though volume susceptibility is dimensionless, there is a 4π correction between Gaussian units and SI units, so not all values of χ found in the literature can be directly compared.

Table 2.1: Magnetic properties, their symbols, and SI units. From Ref.[40]

The relationship between \mathbf{B} , \mathbf{H} , and \mathbf{M} in SI units is defined by:

$$\vec{B} = \mu_0(\vec{H} + \vec{M}) \quad (2.1)$$

where $\mu_0=4\pi\times 10^{-7} \text{ Hm}^{-1}$.

2.1 SINGLE DOMAIN MAGNETIC PARTICLES

Weiss first introduced the concept of magnetic domains in 1906, at the same time as his molecular field theory.[41] Then for a period of 43 years, little experimental work was done to demonstrate the existence of magnetic domains. In 1949, Williams, Bozorth, and Shockley, while working at Bell Telephone Laboratories published the experimental observation of domains in silicon-iron single crystals.[42]

Depending on a particle's physical shape, it will generate a stray magnetic field, \mathbf{H}_s , which will increase the particle's energy according to:

$$\mu_0 \nabla \cdot \vec{H} = -\nabla \cdot \vec{M} \quad (2.2)$$

where \mathbf{M} is the magnetization of the sample and \mathbf{H} is the field. Outside of the sample, the field \mathbf{H} is the stray field, \mathbf{H}_s . If the energy of the particle's stray field is greater than the energy required to form domain walls, the particle can lower its energy by breaking up into multiple magnetic domains. An example of a spherical particle with and without domain walls is displayed in Figure 2.1. A magnetic particle will have only one domain if the energy required to create a domain wall is greater than the decrease in energy that would be achieved by reducing the stray magnetic field. Single domain particles were predicted theoretically in the 1930s[43, 44] and then experimentally confirmed later that same decade.[45] It is possible for single domain magnetic particles to exhibit superparamagnetic behavior, which will be discussed in further detail below.

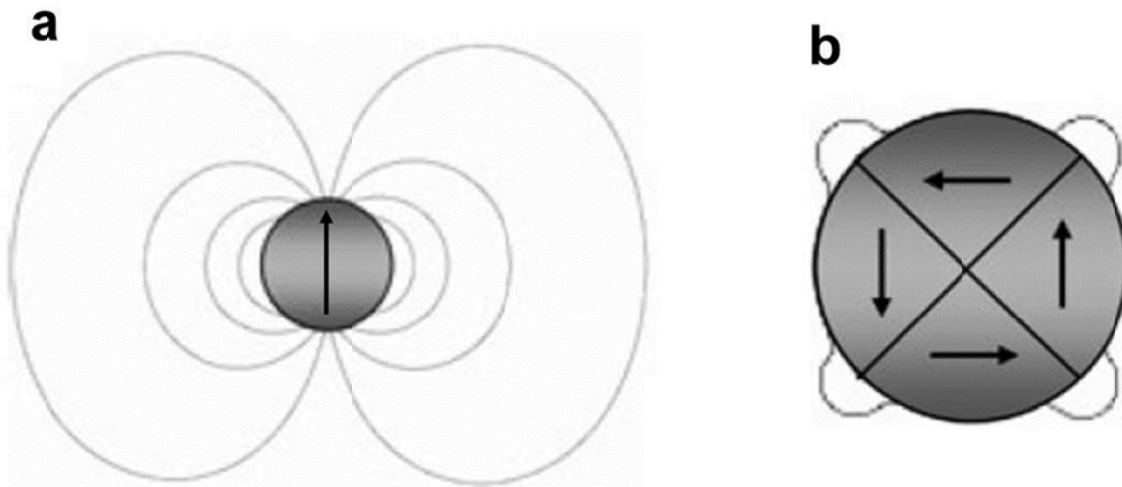


Figure 2.1: The stray magnetic field near spherical particles. (a) The stray field of a single domain particle. (b) Through the creation of domain walls, the stray field of a multi-domain particle is reduced greatly, however energy must be expended in the creation of domain walls. Adapted from Refs.[25, 46] Stray field lines were generated by Vizimag 3.0.[47]

2.2 SUPERPARAMAGNETISM

The theory behind the behavior of single domain nanoparticles was first developed by Néel in 1947[48] and Stoner and Wohlfarth in 1948.[49] Brown built on their efforts in the 1960s and 1970s.[50, 51] Much of the early work focused on what happens when the thermal energy ($k_B T$, where k_B is Boltzmann's constant) is of the same order as the particle's anisotropy energy (KV , where K is the anisotropy constant for a particle with uniaxial anisotropy, neglecting higher terms, and V is the particle's volume). Their predictions regarding the behavior of single domain nanoparticles in this temperature regime were observed experimentally by Bean, Jacobs, and Livingston while working at General Electric Research Laboratory.[52-55] Bean is credited with coining the term superparamagnetism. The term was applied since an ensemble of superparamagnetic nanoparticles would have a zero net magnetic moment in the absence of an external magnetic field (since thermal energy would randomize the distribution of

the particles' moments) but their moments could be aligned with the application of an external field. This is the same behavior described in classical paramagnetism. The key difference, and the reason for the “super”, is that each particle would have a moment of up to several thousand Bohr magnetons (μ_B). For example, a 5 nm diameter iron nanoparticle, which contains approximately 5560 atoms, would have a moment of 12,000 μ_B . [18]

The energy of a superparamagnetic nanoparticle in an external field (H) applied along the z axis, which coincides with the particle's easy axis, can be approximated with the following equation [56]:

$$\varepsilon = KV \sin^2 \theta - mH \cos \theta \quad (2.3)$$

where K is the particle's anisotropy (assuming uniaxial anisotropy), V is the particle's volume, θ is the angle between the particle's moment (m) and the z axis, and μ_0 is the permeability of free space. A plot of this energy is displayed in Figure 2.2. The two minima in energy are located at $\theta = 0$ and $\theta = \pi$ and have the following energies:

$$\varepsilon_1 = -mH \quad \varepsilon_2 = mH \quad (2.4)$$

The two minima are separated by an energy barrier of ε_m .

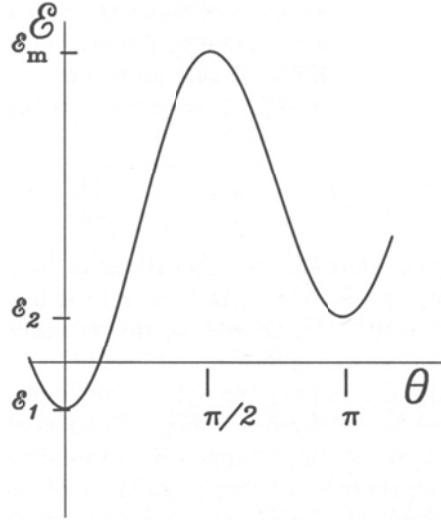


Figure 2.2: The function of equation (2.2) plotted for $mH = 0.15KV$. From Ref.[56]

The number of particles jumping from ε_1 to ε_2 per unit time can then be written as:

$$V_{12} = c_{12} e^{-\beta(\varepsilon_m - \varepsilon_1)} \quad (2.5)$$

where c_{12} is a constant and $\beta = k_B T$. Likewise, the rate of particles jumping from ε_2 to ε_1 can be written:

$$V_{21} = c_{21} e^{-\beta(\varepsilon_m - \varepsilon_2)} \quad (2.6)$$

where much as before c_{21} is a constant. If $H = 0$ both c_{12} and c_{21} are equal. In the study of magnetic nanoparticles, it is more common to consider the reciprocal of equations (2.5) and (2.6), and measure the relaxation time, τ :

$$\tau = \tau_0 \exp\left(\frac{KV}{k_B T}\right) \quad (2.7)$$

where τ_0 is a constant referred to as the attempt time and $\varepsilon_m = KV$ in zero applied field. The relaxation time is the average time it takes the system to jump from one minimum to the next. Equation (2.7) is the Néel-Brown equation. This equation, along with others which account for dipolar interactions, will be discussed in further detail in Chapter 4.

Since both the K and V appear in the exponent of equation (2.7), the relaxation time for an ensemble of particles depends strongly on these parameters. It is worth noting that since the particle volume is proportional to its radius cubed, the relaxation time will be extremely sensitive to very small variations in particle diameter. As an example, a spherical cobalt nanoparticle (with $K = 4.5 \times 10^5 \text{ Jm}^{-3}$ at room temperature)[18] 6.8 nm in diameter would have a room temperature relaxation time of approximately 0.1 s. In contrast, the relaxation time of a cobalt nanoparticle with a diameter of 9 nm would be almost 100 yrs.

The transition from superparamagnetic to non-superparamagnetic behavior is defined to occur at a temperature called the blocking temperature (T_B), around which there is an exponentially rapid slowing down of the magnetic relaxation. Blocking is not a phase transition, but rather a continuous, although rapid variation of $\tau(T)$. The value of the blocking temperature depends on the measurement time, for which $\tau = 100 \text{ s}$ is commonly used. If, as Néel suggested, we take $\tau_0 = 10^{-9} \text{ s}$ [48], we can rearrange equation (2.7) and solve for T_B :

$$T_B = \frac{KV}{25k_B} \quad (2.8)$$

The behavior of an ensemble of magnetic nanoparticles held at a fixed temperature and as a function of diameter is displayed in Figure 2.3. For the smallest diameters, the particles will be both single domain and superparamagnetic. In this region, they will not exhibit any coercivity or hysteresis. As the particles' diameter increases, its anisotropy energy (KV) will increase to the point where the existing thermal energy is not sufficient to switch the magnetization direction within the measurement time and the particles will become blocked. At this point the particles will have a non-zero hysteresis and exhibit both thermal and field dependent hysteresis. The particles' coercivity will

increase as $D^{2/3}$, where D is the particle diameter, and peak at the diameter where the particles begin to form separate magnetic domains. After the formation of domain walls, the particles' coercivity falls off as D^{-1} , approaching bulk behavior.[18]

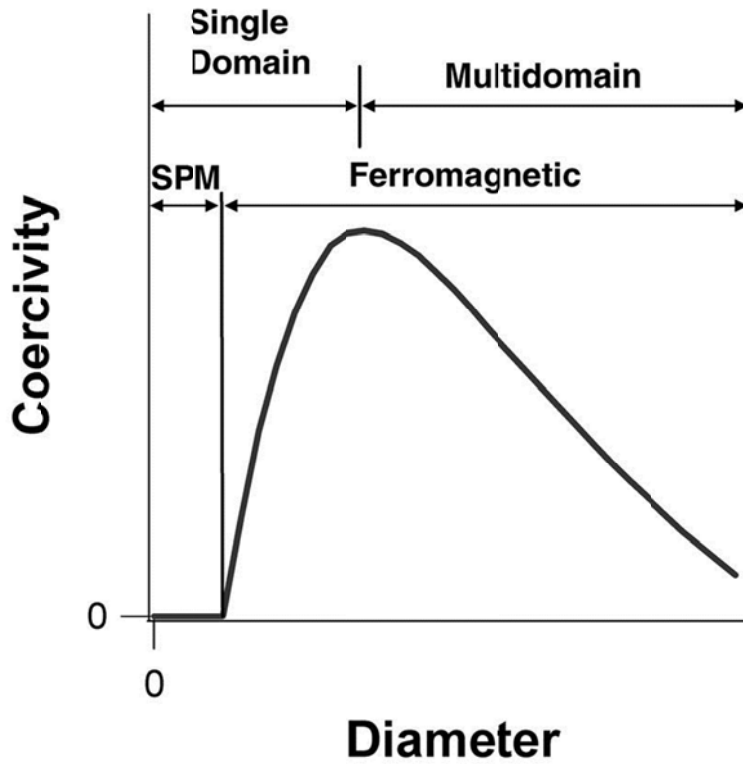


Figure 2.3: The coercivity of an ensemble of magnetic nanoparticles held at a fixed temperature and as a function of particle diameter. Adapted from Ref.[18]

In addition to having no coercivity or hysteresis, an ensemble of superparamagnetic nanoparticles will have a field dependent response which obeys the Langevin equation:

$$\frac{M}{M_s} = L(x) = \coth(x) - \frac{1}{x} \quad x = \frac{mH}{k_B T} \quad (2.9)$$

where M is the ensemble's volume magnetization, M_s is the ensemble's saturation magnetization (per volume), and $L(x)$ is the Langevin function. Since the argument of the Langevin function contains H/T , magnetization curves measured at different temperatures will superimpose when plotted as a function of H/T .

2.3 MAGNETOCRYSTALLINE ANISOTROPY

The dependence of a magnetic material's internal energy on the direction of magnetization is called the magnetocrystalline anisotropy. As the magnetization inside a magnetic domain rotates, all of the spins remain parallel to each other, leaving the exchange interaction between neighboring spins unchanged. Therefore, the exchange interaction is isotropic, and an additional interaction is responsible for magnetocrystalline anisotropy. This additional energy term includes the interactions of the spins with the crystal axes of the magnetic material. A useful model to discuss the effect of crystal structure on the magnetocrystalline anisotropy energy is the spin-pair model.

Consider a pair of spins as displayed in Figure 2.4, where each spin points at an angle φ with the axis connecting the two spins. The energy of the spin-pair can be expanded in terms of Legendre polynomials:[57]

$$w(\cos \varphi) = g + l \left(\cos^2 \varphi - \frac{1}{3} \right) + q \left(\cos^4 \varphi - \frac{6}{7} \cos^2 \varphi + \frac{3}{35} \right) + \dots \quad (2.10)$$

The first term is independent of angle and corresponds to the exchange interaction. The second term has the same form as the magnetic dipole-dipole interaction and is therefore called the dipole-dipole interaction term. The third term in (2.10) is called the quadrupolar interaction and originates from a partially unquenched magnetic orbital moment coupled with the spins. This leads to a variation in the exchange or electrostatic energy with a rotation of the magnetization.

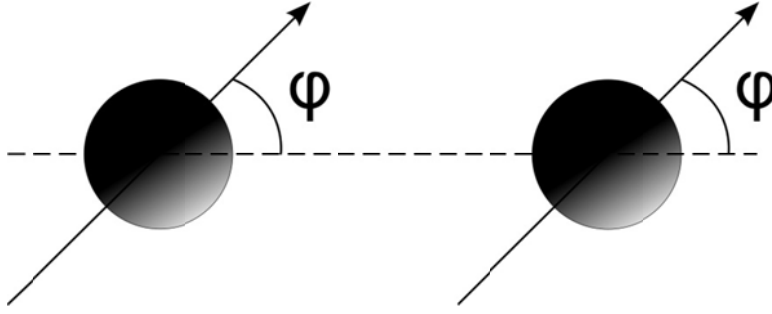


Figure 2.4 A pair of spins. Adapted from Ref.[57]

To calculate the magnetocrystalline anisotropy energy (E_a) for a crystal, the pair energy given by (2.10) must be summed over all spin-pairs in the crystal. This can be written as follows:

$$E_a = \sum_i w_i \quad (2.11)$$

where i is the counting index for each pair. Only first nearest neighbors need to be considered since the pair energy for distant pairs is small. For spin pairs with bonding parallel to the x , y , and z axes, $\cos\phi$ can be replaced by the respective direction cosines along each cube edge in the lattice: α_1 , α_2 , and α_3 . In any bulk cubic crystal, the second or dipole term in (2.10) does not contribute due to symmetry. This term only contributes at sites of reduced symmetry. Then, for a body-centered cubic (bcc) lattice as found in α -Fe:

$$E_a = \frac{16}{9} Nq (\alpha_1^2 \alpha_2^2 + \alpha_2^2 \alpha_3^2 + \alpha_3^2 \alpha_1^2) + const. \quad (2.12)$$

If we express the magnetocrystalline anisotropy of a cubic crystal in terms of the same direction cosines with respect to the three cube edges we will produce an equation with a similar form. To do this, the anisotropy energy is expanded in a polynomial series in α_1 , α_2 , and α_3 . This job is made easier because of the high symmetry of the cubic crystal, for which there are many equivalent directions. An example of equivalent

directions in a cubic lattice is shown in Figure 2.5, where points A_1 , A_2 , B_1 , B_2 , C_1 , and C_2 are displayed on an octant of the unit sphere.

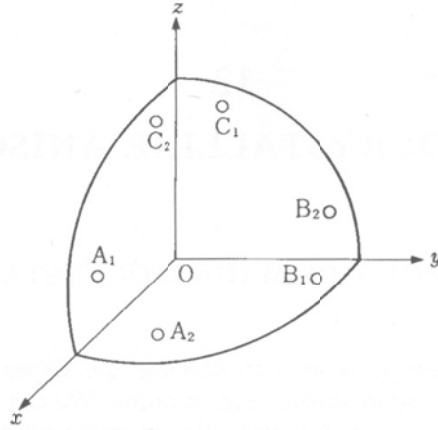


Figure 2.5: Equivalent directions in a cubic crystal. From Ref.[57]

After expanding in α_1 , α_2 , and α_3 and applying symmetry relations, it can be shown that:

$$E_a = K_1(\alpha_1^2 \alpha_2^2 + \alpha_2^2 \alpha_3^2 + \alpha_3^2 \alpha_1^2) + K_2 \alpha_1^2 \alpha_2^2 \alpha_3^2 + K_3(\alpha_1^2 \alpha_2^2 + \alpha_2^2 \alpha_3^2 + \alpha_3^2 \alpha_1^2)^2 + \dots \quad (2.13)$$

where K_n are the anisotropy constants. By comparing (2.12) and (2.13) we can see that in a bcc lattice:

$$K_1 = \frac{16}{9} Nq \quad (2.14)$$

If $K_1 > 0$ as in bcc iron, it can be seen that E_a is higher for [111] than for [100]. This makes the [100], [010], [001], $[\bar{1}00]$, $[0\bar{1}0]$, and $[00\bar{1}]$ directions (because of symmetry), or the cube edges the easy axes and the cube diagonals the hard axes. In nickel, where $K_1 < 0$, the cube edges are the hard axes and the cube diagonals the easy axes. For iron at 20 °C[57]:

$$\begin{aligned}
 K_1 &= 4.72 \times 10^4 \text{ Jm}^{-3} \\
 K_2 &= -0.075 \times 10^4 \text{ Jm}^{-3}
 \end{aligned}
 \tag{2.15}$$

So, in most cases K_2 can be ignored when calculating the magnetocrystalline anisotropy of iron. Magnetization curves for bulk iron along three different crystallographic directions is displayed in Figure 2.6.

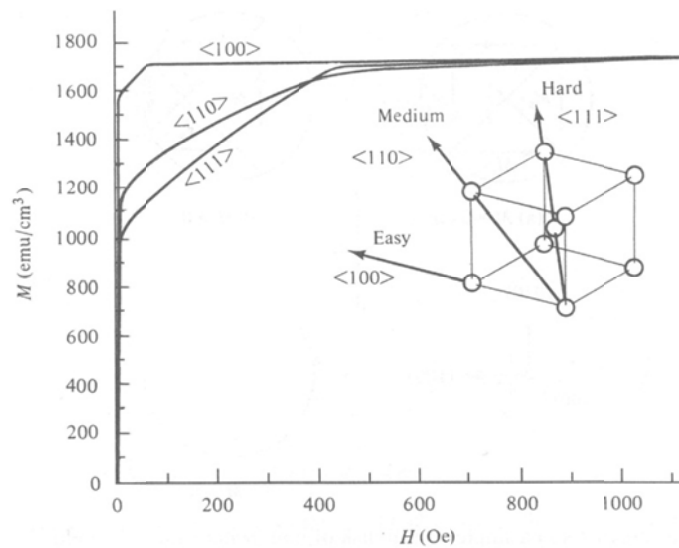


Figure 2.6: Plots of magnetization vs. applied field for a sample of iron taken along three different crystallographic directions. From Ref.[18]

2.4 MAGNETIC NANOPARTICLE AND THIN FILM LITERATURE RESULTS TO DATE

Both literature and experiment show encouraging possibilities for synthesizing transition metal nanoparticles with magnetic moments that are enhanced compared to bulk materials. While iron nanoparticles with large moments would offer increased performance in a host of applications, high σ_{sat} iron nanoparticles from solution based synthesis routes have been extremely elusive.

2.4.1 Solution Synthesized Magnetic Nanoparticles

The reactivity of iron makes the solution based synthesis of oxide free nanoparticles extremely difficult. However, solution based synthesis provides one of the only routes for the production of tailorable iron nanoparticles in sufficient quantities for practical applications. Because of iron's reactive surface, most of the highest quality iron nanoparticle syntheses reported produce particles with either an oxide or a magnetically dead layer at their surface.[23-27] The nonmagnetic or oxide layer can often be caused through interaction between the particle's surface and the organic ligands attached to the particle. This results in iron nanoparticles with σ_{sat} values substantially below that of bulk iron.

It has been demonstrated that iron nanoparticles' magnetizations are very sensitive to the type of surfactant used. For example, when Smith and Wychick synthesized 7-9 nm diameter iron nanoparticles via identical routes using a polybutadiene homopolymer, butadiene-styrene copolymer, and styrene-4-vinyl-pyridine copolymer, the synthesis produced particles with σ_{sat} values of 172 Am²kg⁻¹, 125 Am²kg⁻¹, and 82 Am²kg⁻¹, respectively.[28] As the polarity of the polymers used increased the particles' magnetization decreased. A similar study was completed by Gedanken and co-authors when they synthesized iron nanoparticles via a surfactant-free sonochemical route and coated separate aliquots of the resulting particles with different surfactants. The experiments produced nanoparticles with σ_{sat} values of 85, 55, 10, and 5 Am²kg⁻¹ for particles coated with an alcohol, a carboxylic acid, a sulfonic acid, and a phosphonic acid, respectively.[27] As the ligand's reactivity increased, the particles' magnetization decreased.

Only one research group has reported the synthesis of iron nanoparticles with a saturation magnetization greater than or equal to that of bulk iron.[29] Margeat, *et al.*

synthesized iron nanoparticles through the hydrogenation of a bis(ditrimethylsilyl)amido iron complex. However, this unique iron precursor only yielded iron particles with a σ_{sat} greater than or equal to bulk iron when poly(2,6-dimethyl-1,4-phenyleneoxide) was used as a surfactant. These same particles also had a magnetocrystalline anisotropy an order of magnitude greater than bulk iron. When the same iron precursor was used in combination with carboxylic acid and/or amine based surfactants, the particles' σ_{sat} was always less than that of bulk iron. These results from literature provide additional evidence of the extreme sensitivity of the iron nanoparticle surface, and the particle magnetism, to its environment.

The reactivity of iron's surface is significantly greater than other transition metals, as evidenced by several cobalt and nickel based nanoparticle syntheses which yield magnetizations equal to, or in some cases greater than, the bulk metal. Wilcoxon, *et al.* synthesized 1.8 nm diameter cobalt nanoparticles with alkylated polyether surfactants which had a σ_{sat} of $178 \text{ Am}^2\text{kg}^{-1}$ (which exceeds the bulk value of $162 \text{ Am}^2\text{kg}^{-1}$).[34] For these particles, exchanging the polyether surfactants with phosphines and carboxylic acids had no effect on their magnetization, although dodecanethiol did decrease their magnetization by over 35%. Chen, *et al.* reported on the synthesis of Co nanoparticles using an inverse micelle based method.[30] In their particles an increase in magnetic moment (up to 30% over the bulk value) along with an increase in magnetocrystalline anisotropy was observed as the diameter of the synthesized particles decreased. The authors believe their particles consisted of an fcc Co core surrounded by a shell of paramagnetic Co of uncertain composition. Amiens and co-workers were successful in synthesizing Co nanoparticles, Co nanorods, Ni nanorods, and NiFe nanoparticles all with magnetizations equivalent to the bulk material.[31-33] Although the NiFe

nanoparticles' σ_{sat} was identical to bulk NiFe, the particles had a magnetocrystalline anisotropy more than two orders of magnitude higher than bulk NiFe alloy.

2.4.2 Surfactant Free Magnetic Nanoparticle Beams

In contrast, when ferromagnetic transition metal nanoparticles are synthesized in a non-reactive environment, they exhibit σ_{sat} values in excess of their bulk counterparts. This has been best demonstrated experimentally by creating particle beams of transition metal nanoparticles using pulsed laser vaporization of a metal source in an inert carrier gas. The particle beam is then injected into a ultra-high vacuum (UHV) chamber, where the particle magnetization can be determined by measuring the beam deflection after passing through a Stern-Gerlach magnet. Results from these types of experiments show an increase in particle magnetization with decreasing particle diameter.[35-37] The results for iron, cobalt, and nickel are qualitatively similar, as can be seen from results published in Ref. [36] and displayed in Figure 2.7.

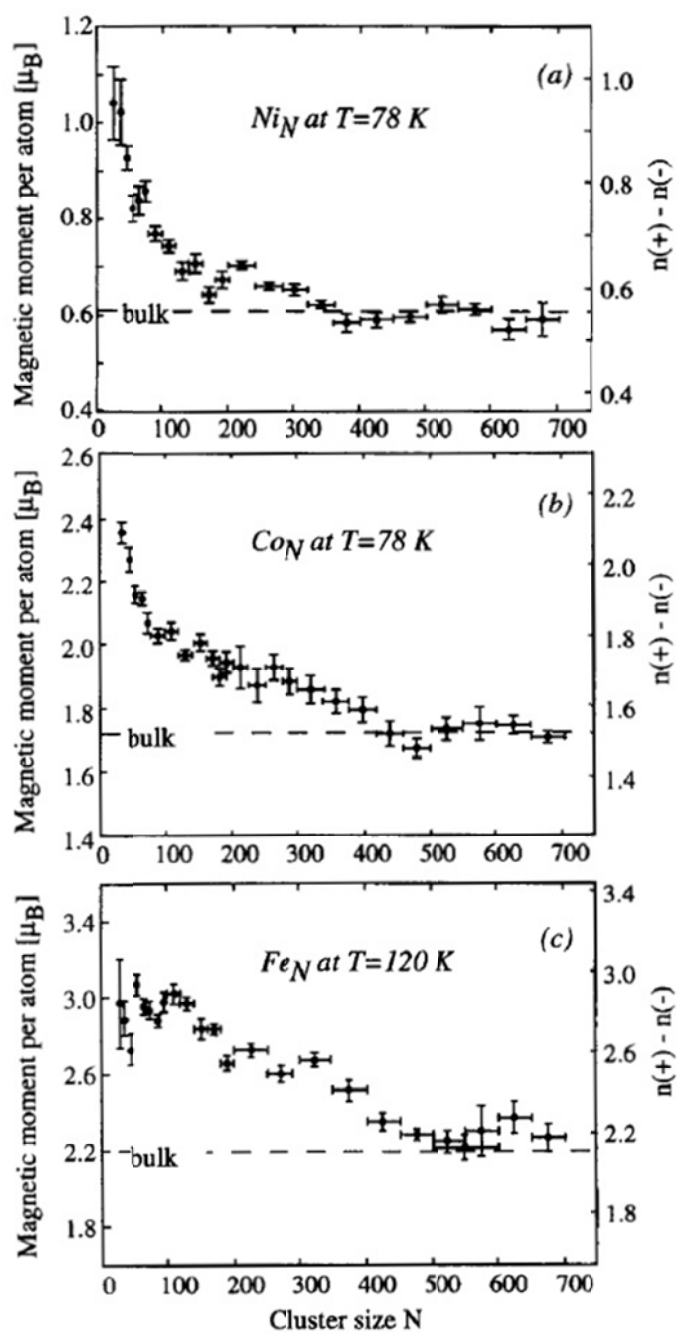


Figure 2.7: Magnetic moment for Ni, Co, and Fe surfactant free particle beams as a function of number of atoms per particle. The spin imbalance per atom is indicated on the right scale. From Ref.[36]

2.4.3 Epitaxial Fe Thin Films

Enhanced magnetization in iron epitaxial films has been observed on both W(110) and Ag(100) substrates. Indirect evidence of a ~14% enhancement in the magnetization of Fe(110) on W(110) was shown by extrapolating torsion magnetometer measurements to low temperature.[58] Additionally, polarized neutron reflectometry indicated an enhanced magnetic moment in thin Fe films.[59] However, these measurements require beam and background corrections, calculated asymmetries, and very accurate film thickness determinations, which is common to almost all thin film magnetization measurements.[60]

Markert and co-workers provided a direct measurement of enhanced moments in ultrathin (1-5 ML) Fe films on Ag(100) substrates. After growth of the thin Fe films, they were capped with Au and measured in a SQUID magnetometer. Magnetic moments enhanced by as much as ~30% were observed. A plot of the ratio of the average moment per atom to the bulk value as a function of film thickness is displayed in Figure 2.8.

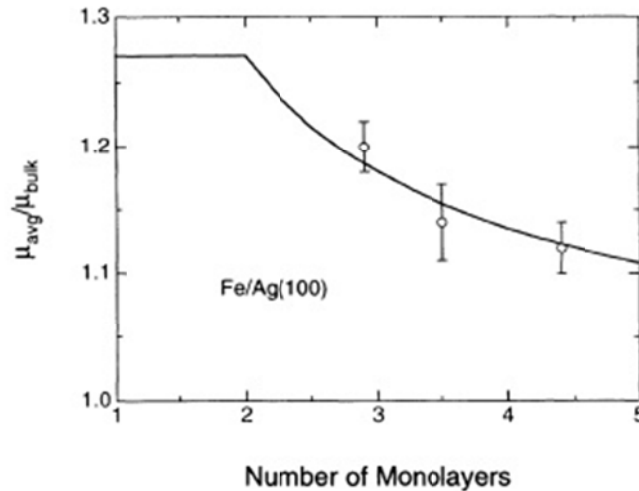


Figure 2.8: Ratio of the average moment per atom to the bulk value ($2.22\mu_B$) as a function of film thickness for 2.9, 3.5, and 4.4 ML Fe(100)/Ag(100) films. The solid line is a fit which assumes that all of the moment enhancement occurs in the interface layers. From Ref.[61]

2.4.3 Ab Initio Modeling Results

The results from the particle beam and epitaxial thin film based experiments agree with ab initio modeling of transition metal surfaces both in thin films and small clusters of atoms. The bulk of the literature focuses on the study of magnetic thin films and suggests an enhancement of the magnetic moment.[62-65] Press, *et al.* modeled clusters of Fe and Ni atoms, and similarly found an increase in magnetism compared to the bulk metals.[66] Both Chelikowsky and co-workers and Yang, *et al.* showed an enhanced magnetization in iron clusters that decreases towards the bulk limit with increasing particle size.[67, 68] The increase in magnetism can be attributed to a decrease in nearest neighbors at the metal surface. This lower coordination number results in more localized electron wavefunctions, a narrower d-band, and in turn a larger magnetic moment per atom. Figure 2.9 shows a qualitative model showing the evolution of magnetism for iron from the atom through the bulk as the coordination for the system changes. As the coordination number for iron increases, the density of states broadens.

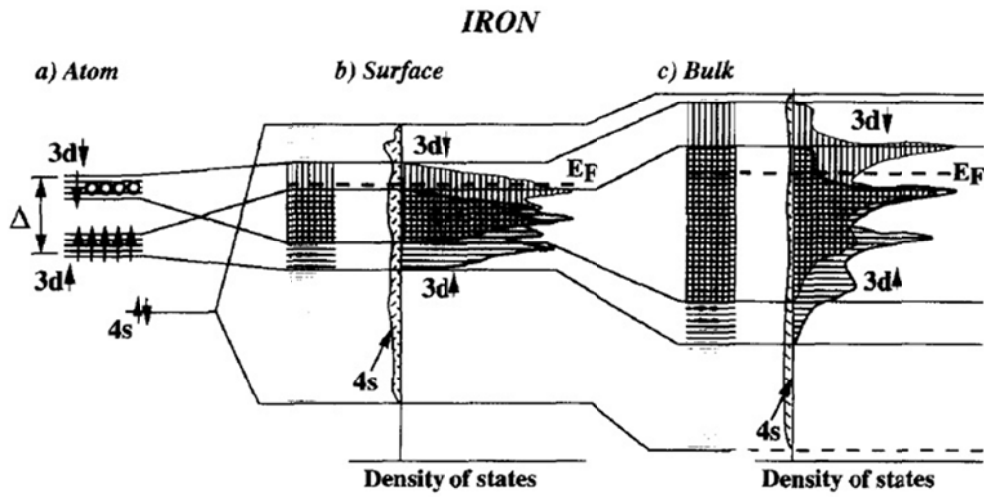


Figure 2.9: Qualitative model showing the evolution of the spin density of states for iron from the atom through the bulk via a low coordination environment. The symbol Δ stands for the exchange energy. From Ref.[36]

Chapter 3

Solution Based Synthesis of Magnetic Nanoparticles

3.1 INTRODUCTION TO SOLUTION BASED NANOPARTICLE SYNTHESIS

Although it is possible to form magnetic nanoparticles from various vapor phase techniques, these particles are either short lived or end up bound to a substrate.[35-37, 69-73] In order to produce unbound magnetic nanoparticles in quantities large enough for almost any application, solution based synthesis routes are required. For transition metals, particularly iron, the surface is highly reactive and air-free chemistry techniques are required. The use of a Schlenk line, or manifold for supplying inert gas and pulling a vacuum on laboratory glassware, is necessary. A diagram of a Schlenk line is shown in Figure 3.1. Additionally, reagents and solvents must be purified and distilled. These purified reagents are most often stored in an inert gas glove box, where often times the chemical apparatus for nanoparticle synthesis is first assembled prior to connection to the Schlenk line. A photograph of an inert gas glove box is shown in Figure 3.2.

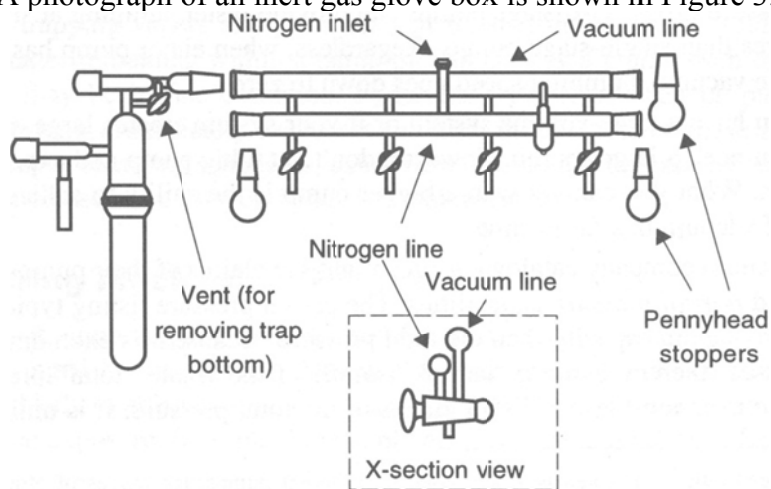


Figure 3.1: Schematic of a Schlenk line used for air-free chemistry. From Ref.[74]



Figure 3.2: Inert gas glovebox manufactured by Innovative Technologies, Inc.

3.2 SYNTHESIS OF IRON NANOPARTICLES

Chemists at Sandia Labs sought to develop a new solution based synthesis of iron nanoparticles that would yield σ_{sat} values close to or even exceeding bulk iron. The synthesis was based on the frequently used thermal decomposition of iron pentacarbonyl.[76-78] The novelty of the synthesis route is the surfactant used, 2,4-pentanedione, which is a more weakly binding surfactant compared to those found in the literature. 2,4-pentanedione is capable of chelating iron but is not known to oxidize iron as carboxylic acids or alcohols are. Details of the synthesis along with TEM and magnetic characterization has been reported earlier.[5]

All chemicals and reagents were purchased from Sigma-Aldrich. Dioctyl ether, octadecene, 2-4-pentanedione (PD), and hexaethylene glycol monododecylether (C12E6) were purified by vacuum distillation. Prior to distillation, dioctyl ether and octadecene

were first dried over sodium metal. PD and C12E6 were dried over sodium sulfate prior to vacuum distillation. Iron pentacarbonyl, 99.5%, was purified by vacuum transfer. All purified reagents were stored in an inert gas glove box. Purified iron pentacarbonyl or $\text{Fe}(\text{CO})_5$ was mixed with either dioctyl ether or octadecene and stored in a $-50\text{ }^\circ\text{C}$ freezer inside a glovebox to prevent premature decomposition.

Fe nanoparticles with PD surfactants were synthesized using a previously published procedure.[5] Briefly, a reaction flask is filled with 2 mL of dioctyl ether and 0.002 mL PD inside an inert gas purged glove box. The flask is then removed from the glove box, attached to a bubbler, and put under flowing nitrogen. Next, the flask is heated to $200\text{ }^\circ\text{C}$ with a reflux condenser and vigorous stirring. A syringe filled with dioctyl ether, PD, and iron pentacarbonyl is inserted into the flask via a septa top. The syringe is filled with a 900:1 volumetric ratio of dioctyl ether to surfactant and 100:1 volumetric ratio of iron pentacarbonyl to surfactant. The contents of the syringe are injected into the flask at a rate of 1.6mL/hr. using a syringe pump. The injection time is adjusted to alter the final iron pentacarbonyl to surfactant ratio (and final particle size). Once the entire contents of the syringe are injected into the flask, the reaction is allowed to continue for 1 hr. After the completion of the reaction, the flask containing the iron nanoparticles is pumped into a nitrogen purged glove box.

Fe nanoparticles with C12E6 surfactants are synthesized with an almost identical procedure. The differences were filling the reaction flask with 1.44 mL of octadecene and 0.05 mL of C12E6. The contents of the syringe did not contain surfactant. Rather, it only contained a 4:1 volumetric ratio of octadecene to $\text{Fe}(\text{CO})_5$. The C12E6 molecules are much larger than PD molecules, interact differently with the iron surface, and provide another system to compare and contrast the PD data to. The chemical structure of both PD and C12E6 are displayed in Figure 3.3. Throughout the study, extreme care was

taken with sample preparation to ensure the iron nanoparticles were not exposed to water or air.

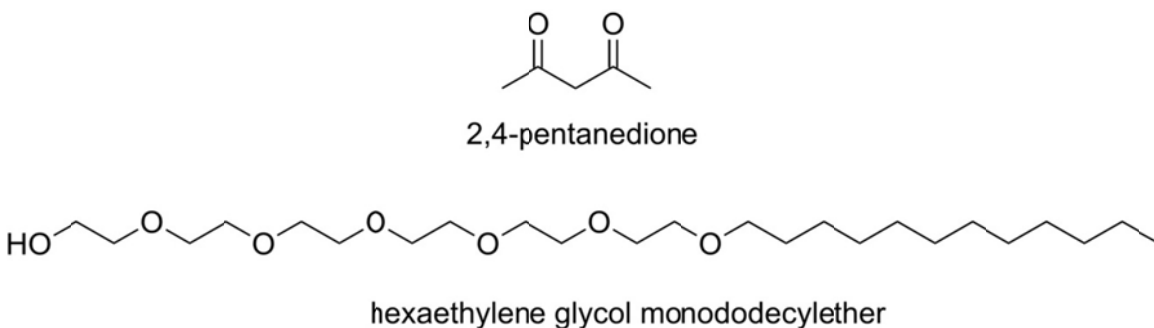


Figure 3.3: Chemical structure of ligands used for iron nanoparticles: 2,4-pentandione and hexaethylene glycol monodocecyclether.

3.3 TEM CHARACTERIZATION

3.3.1 Sample Preparation

Samples for microscopic analysis were prepared inside an inert gas glovebox by depositing the nanoparticles onto a holey carbon coated copper TEM grid (Structure Probe, Inc.; West Chester, PA). A 3 μL aliquot was withdrawn from a flask containing the nanoparticles immediately after vigorously vortexing and then added to the surface of the TEM grid. Filter paper placed under the TEM grid was used to aid in wicking away excess solvent and to evenly disperse the nanoparticles across the holey carbon surface. After the grids were prepared they were sealed inside two glass vials (one inside the other) and placed immediately into a custom made nitrogen purged antechamber for the TEM. Once the antechamber was purged for >15 min., the samples were loaded into the microscope.

Bright field TEM images were acquired with a JEOL 1200 EX (Tokyo, Japan) using an acceleration voltage of 120 kV. The instrument has a point to point resolution of approximately 9 Å. Images were collected on a Gatan slow scan CCD camera.

3.3.2 Results and Size Analysis

Size distributions of the iron nanoparticles were determined from TEM images using ImageJ (public domain software, National Institutes of Health; Bethesda, MD, USA). Briefly, the Feret diameter (defined as the maximum caliper diameter) was measured for a minimum of 300 particles selected from multiple micrographs. Both particles in contact with the edge of an image and overlapping particles were excluded from the size analysis.

Although the particles were stored and handled only under inert conditions, an oxide layer is still visible in many of the TEM images. The presence of some oxidized species detected through XAFS experiments will be discussed below. However, the amount of oxide detected in XAFS experiments cannot fully account for the oxide shell visible in the TEM images. Once the particles are deposited onto a TEM grid and the solvent evaporated, the reactive iron surface is particularly susceptible to oxidation. In fact, a monolayer of iron oxide has been shown to form with 1×10^{-6} Torr sec exposure of oxygen and stepped surfaces have been shown to be even more susceptible to oxidation.[79, 80] Therefore, TEM measurements conducted under high vacuum (HV) conditions are not an accurate way to determine the presence or absence of surface oxide. Methods which measure the properties of a large ensemble of particles maintained in dried and degassed solvents are much better for this purpose.

A TEM image of iron nanoparticles synthesized with a $\text{Fe}(\text{CO})_5:\text{C}_{12}\text{E}_6$ molar ratio of 1:1 is displayed in Figure 3.4. The inset of Figure 3.4 contains a histogram of the

particle size distribution for this sample. A TEM image (with a histogram of the particle size distribution included as an inset) of a sample synthesized with a $\text{Fe}(\text{CO})_5$:C12E6 molar ratio of 11:1 is displayed in Figure 3.5. Samples synthesized with PD surfactants are displayed in Figures 3.6 and 3.7. Figure 3.6 contains an image of particles synthesized with a $\text{Fe}(\text{CO})_5$:PD ratio of 13:1 and Figure 3.7 shows an image of particles synthesized with a $\text{Fe}(\text{CO})_5$:PD ratio of 35:1. Both figures contain histograms of the sample size distribution as an inset.

Analyzing the particle sizes as a function of iron pentacarbonyl to surfactant ratio shows that particle diameter can be controlled in a linear fashion over a limited range when both PD and C12E6 surfactants are used. The mechanism for nanoparticle growth in the case of both ligands has an initial nucleation phase as the iron pentacarbonyl solution is first dripped into the reaction vessel. This results in non-linear growth at the lowest iron pentacarbonyl to surfactant ratios. The nucleation phase is followed by a sustained period of linear growth, which is plotted for both surfactants in Figure 3.8. It is believed that once the particles have grown to a certain size, their magnetic moments are sufficiently large that magnetic agglomeration following by precipitation to the bottom of the reaction vessel occurs. If iron pentacarbonyl continues to be added into the reaction vessel, another phase of particle nucleation begins. This process, if controlled properly, could be used to synthesize large volumes of iron nanoparticles of a specified diameter over a sustained period of time.

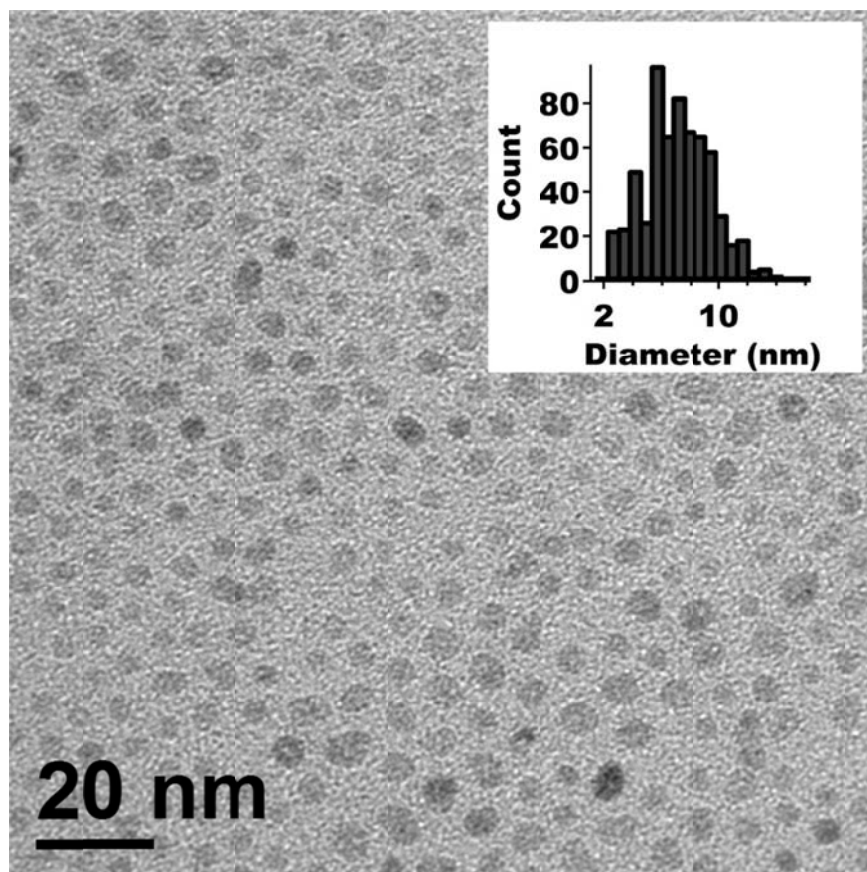


Figure 3.4: TEM image of Fe nanoparticles synthesized with a $\text{Fe}(\text{CO})_5$:C12E6 ratio of 1:1. The inset is a histogram of the distribution of particle diameters determined by analyzing over 300 particles.

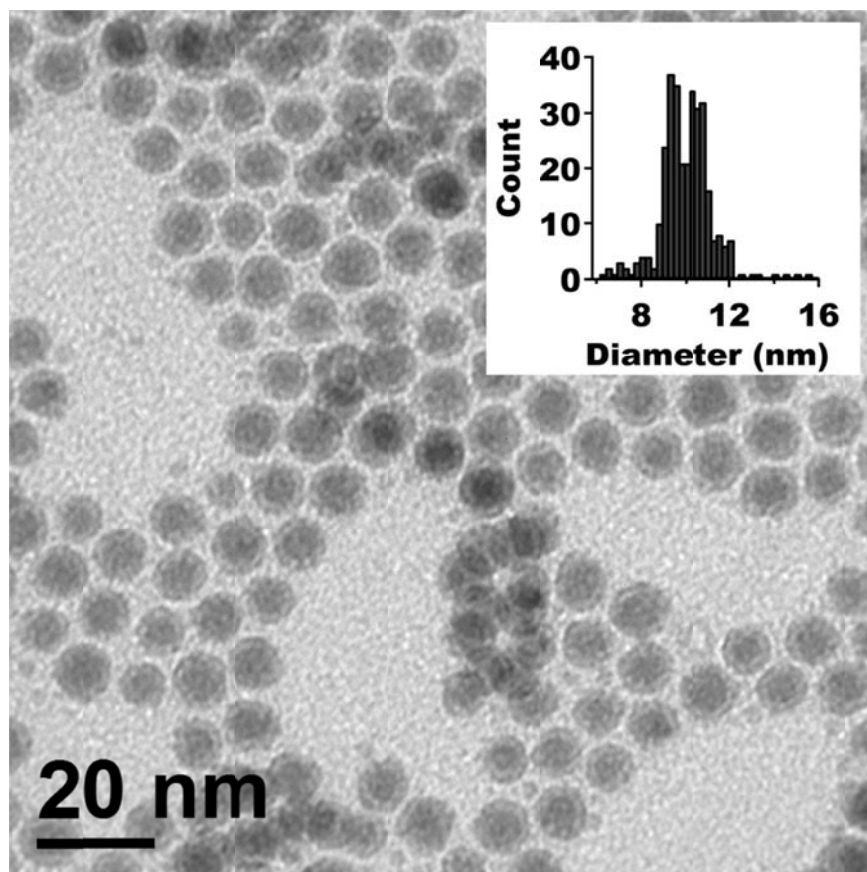


Figure 3.5: TEM image of Fe nanoparticles synthesized with a $\text{Fe}(\text{CO})_5$:C12E6 ratio of 11:1. The inset is a histogram of the distribution of particle diameters determined by analyzing over 300 particles.

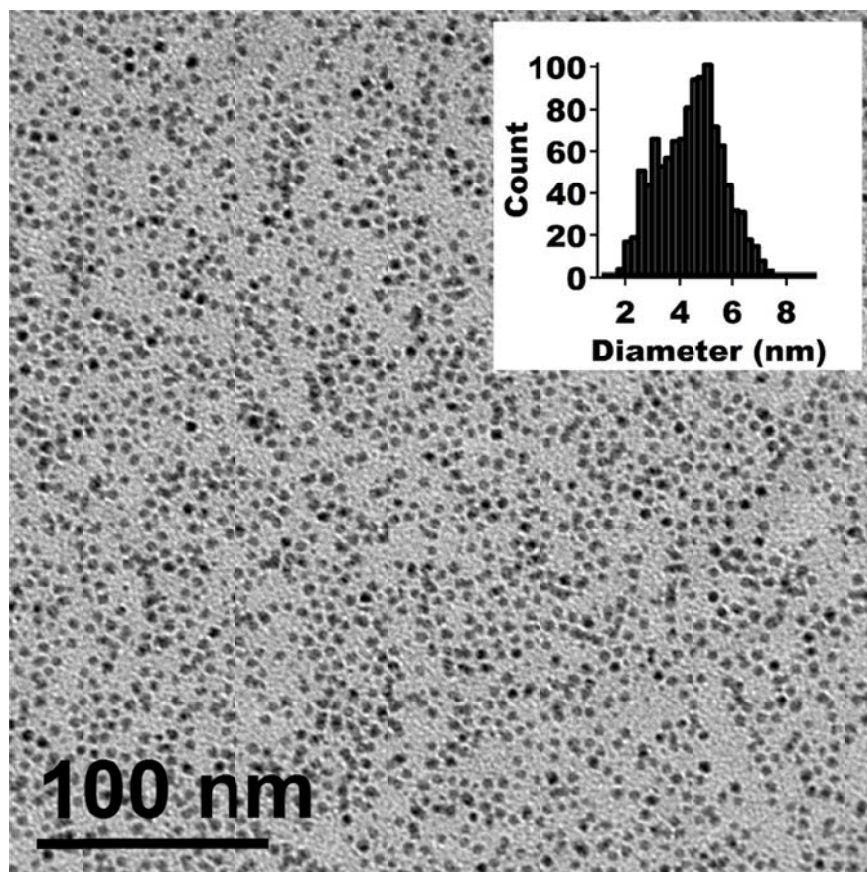


Figure 3.6: TEM image of Fe nanoparticles synthesized with a $\text{Fe}(\text{CO})_5$:PD ratio of 13:1. The inset is a histogram of the distribution of particle diameters determined by analyzing over 300 particles.

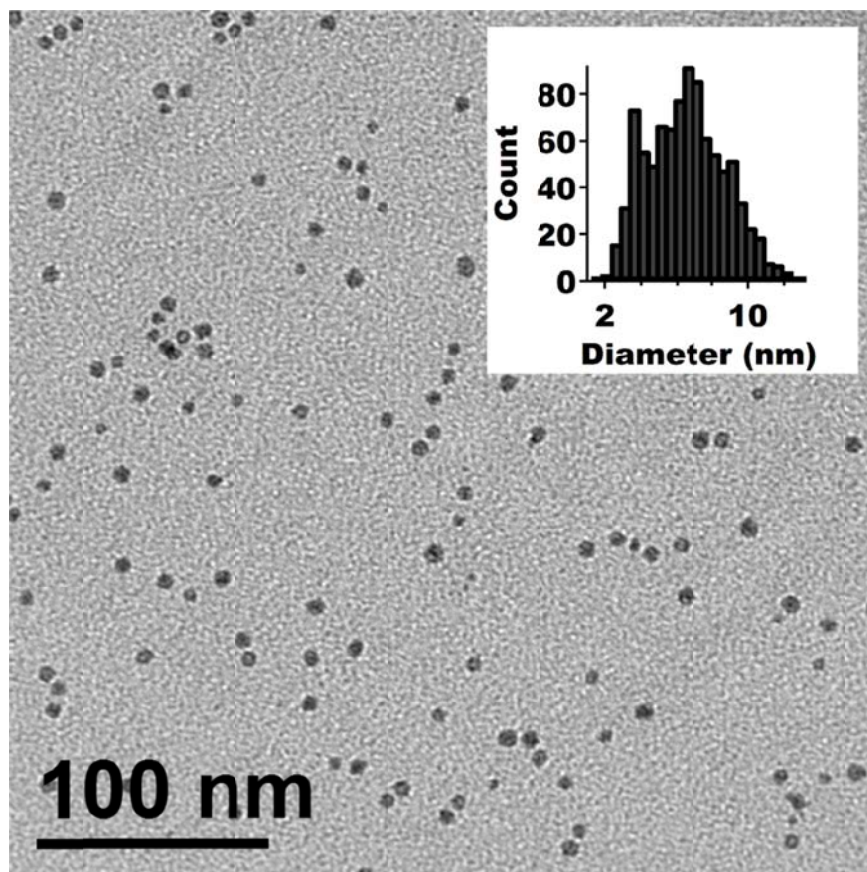


Figure 3.7: TEM image of Fe nanoparticles synthesized with a $\text{Fe}(\text{CO})_5$:PD ratio of 35:1. The inset is a histogram of the distribution of particle diameters determined by analyzing over 300 particles.

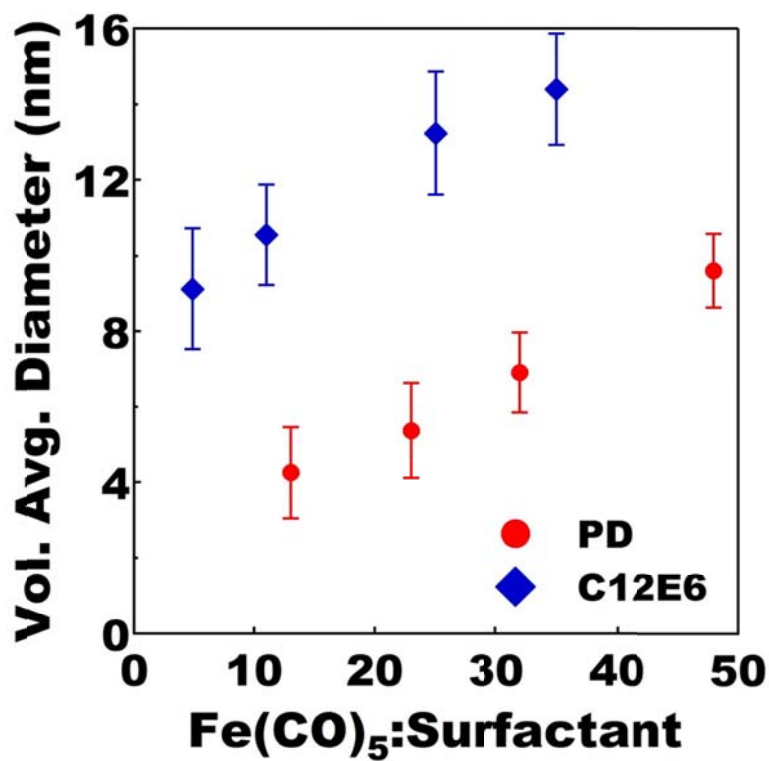


Figure 3.8: Plot of the volume average diameter as a function of the iron pentacarbonyl to ligand ratio for iron nanoparticles synthesized with pentanedione (PD) and hexaethylene glycol monododecylether (C12E6) surfactants.

Chapter 4

Magnetic Characterization of Magnetic Nanoparticles¹

4.1 INTRODUCTION TO MAGNETOMETRY

When measuring small samples or those with a low moment, flux based methods of measuring magnetization are often the most practical. These methods measure the change in flux through a pick-up coil as the sample is moved. Those most simple of the flux based methods is the extraction magnetometer, in which a sample starting at the center of a pick-up coil is removed to a point outside of the coil. By using two oppositely wound segments, so as to not register changes in the field applied to the sample, an improved pick-up coil can be constructed. Extraction magnetometers can have a sensitivity of approximately 10^{-6} Am^2 .^[81] The vibrating sample magnetometer (VSM) is essentially an AC version of the extraction magnetometer. In a VSM, the sample is vibrated at a frequency typically in the range of 10-100 Hz about the center of a set of pick-up coils. A VSM is capable of detecting moments as small as approximately 10^{-8} Am^2 .^[81] An extremely sensitive flux based method of magnetic measurements uses a superconducting quantum interference device (SQUID). SQUID magnetometers have sensitivities of 10^{-10} Am^2 for DC measurements and as high as 10^{-12} Am^2 for AC measurements. The high sensitivity is made possible by the SQUID device itself, which can detect a 10^{-6} fraction of a flux quantum $h/2e = 2.1 \times 10^{-15} \text{ Tm}^2$.^[81]

4.1.1 SQUID Magnetometry

The magnetometry measurements described here were made on a Magnetic Property Measurement System (MPMS) manufactured by Quantum Design (San Diego, CA). The MPMS combines several different systems to make an integrated platform for

¹ Part of this chapter was submitted for publication in J. Magn. Mater. on 11/2/2011.

measuring the magnetic response of samples. These systems include: a temperature control system which allows the temperature of the sample to be adjusted between 1.9 to 400 K; a superconducting magnet capable of generating fields up to 7 T; a SQUID detector and amplifier system; a sample handling system to control the motion of the sample through the pick-up coils; and a computer operating system. The MPMS is available with an AC measurement option capable of supplying drive frequencies between 0.1 Hz and 1 kHz.

The rf SQUID is the key component of the MPMS magnetic moment detection system. The rf SQUID was made possible by B.D. Josephson, who proposed the Josephson junction in 1962, and for which he later won a Nobel Prize. In 1964, Anderson and Rowell experimentally observed a Josephson junction. A SQUID device consists of a closed superconducting loop with one (rf) or two (DC) Josephson junctions in the loop's current path. Since they are considered easier to manufacture, rf SQUIDS are more common in commercial instruments.

Although the SQUID is a highly sensitive device for detecting magnetic fields, in the MPMS, it is not used to directly measure the sample's magnetic field. Instead, the SQUID is located approximately 11 cm below the instrument's superconducting magnet and inside of a superconducting shield, which protects the SQUID from the field generated by the superconducting magnet and the ambient laboratory field. The SQUID is connected to superconducting pick-up coils which sit just outside of the sample space via superconducting wires. Any change in magnetic flux inside the pick-up coils changes the persistent current in this closed superconducting loop. The SQUID then functions as an extremely sensitive linear current-to-voltage detector.

The detection coil is a superconducting wire wound into three coils to form a second-order, i.e. second-derivative, gradiometer (see Figure 4.1). The upper coil is a

single clockwise turn, the center coil is two turns wound counter-clockwise, and the bottom coil is once again a single clockwise turn. The magnetic field created by the sample couples inductively into the set of pick-up coils as the MPMS stepper motors move the sample through the gradiometer. This configuration makes the SQUID detector circuit less susceptible to variations in the field generated by the superconducting magnet since flux changes in the two-turn center coil would be exactly canceled by the single-turn top and bottom coils.

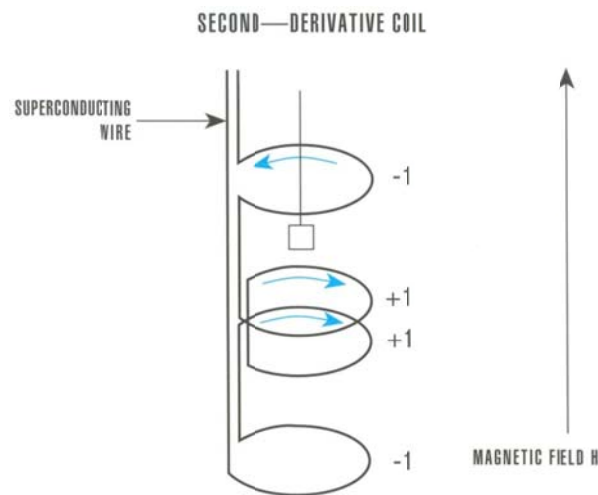


Figure 4.1: Second-order gradiometer used inside the Quantum Design MPMS. From Ref.[82]

Just outside of the pick-up coils (see Figure 4.2 for picture of the main components of the MPMS surrounding the sample space) lies a superconducting magnet made of NbTi wire wound in a solenoid configuration. The magnet is constructed as a closed superconducting loop, allowing it to be operated during measurement in persistent mode without an external power supply, minimizing noise during the measurement. In order to change the field of the superconducting magnet, a persistent-current switch is

formed by wrapping a heater around a small segment of the NbTi wire. A current source is attached to both ends of the switch, and allows the current flowing through the superconducting magnet to be changed. The superconducting magnet, detection coils, and SQUID are all maintained in a bath of liquid He (4.2 K at sea level) to maintain their superconducting state.

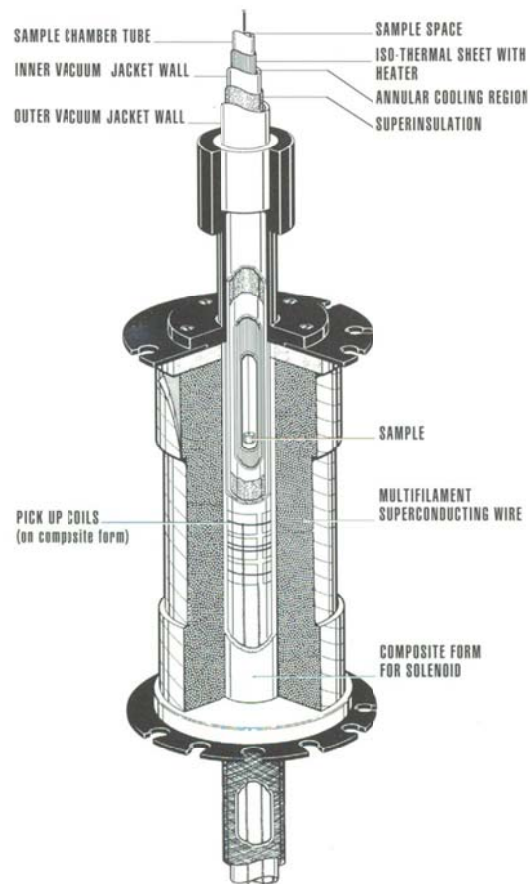


Figure 4.2: Layout of the major components of the Quantum Design MPMS surrounding the sample space. From Ref.[82]

Just inside of the pick-up coils lies the sample space, which is a 9 mm diameter tube maintained with a low pressure of helium gas. The lower 30 cm of the sample tube

is lined with copper to maintain a region of high thermal uniformity. Two calibrated thermometers are placed inside the sample space to ensure precise temperature control, which is regulated through the use of heating coils and pulling liquid He boil off (from the liquid He which immerses the superconducting solenoid and detection circuit) through the sample space. Samples are loaded into the sample space via an airlock system.

The sample is attached to the end of a long rigid sample rod, which feeds into the sample space through a double seal called a lip seal. The top of the sample transport rod is attached to a stepper motor which moves the sample through the pick-up coils in a series of discrete steps. Since the detection circuit is a complete superconducting loop, the induced current will not decay and it is possible to move the sample in steps rather than a continuous motion. The SQUID voltage is recorded at each stop of the stepper motor and the entire scan can be repeated multiple times to improve signal-to-noise. If the sample is much smaller than the detection coil and is uniformly magnetized it will produce a signal very close to that of a point-source magnetic dipole being pulled through a second-order gradiometer. A magnetic nanoparticle sample whose signal very closely matches that of dipole source is displayed in Figure 4.3. The magnetometer software has fit the data with the theoretical signal of a dipole moving through the gradiometer using a linear regression algorithm. By fitting the data in this fashion, the MPMS software can extract the sample's moment.

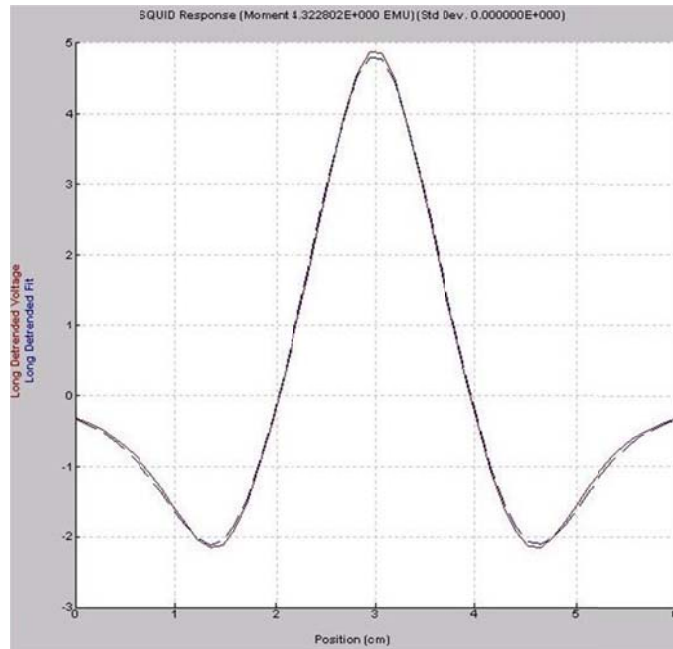


Figure 4.3: Signal generated from a magnetic nanoparticle sample being pulled through the second-order gradiometer pick-up coils of a MPMS (red solid line). A linear regression fit of the theoretical signal of a dipole moving through the second-order gradiometer is displayed as a blue dashed line.

4.1.2 Magnetic Measurements of Superparamagnetic Nanoparticles

Generally, both the field dependent and temperature dependent response of magnetic nanoparticles are measured. The field dependent response is often measured at a series of different temperatures, producing a hysteresis loop or a plot of the sample's magnetization, M , as it responds to an external field, H . For each temperature, the sample starts at zero field and is taken to a high positive field where it achieves saturation magnetization M_s . If the sample behaves ferromagnetically, it will maintain a remanance magnetization, M_r , when the external field is lowered to zero. In order to further reduce or reverse the magnetization a coercive field, H_c , is required in the negative direction. By increasing the field in the negative direction, the sample is once again taken to magnetic saturation. The sample is then returned to positive magnetic saturation, forming a closed

loop. If the sample is measured above its T_B , it will not exhibit any remanance magnetization or coercivity, and its magnetic response can be fit with the Langevin equation (2.9). The hysteresis loop of a ferrite nanoparticle sample below its blocking temperature is displayed in Figure 4.4a. The saturation magnetization, remanance magnetization, and coercive field are all labeled. The magnetic response of the same sample at 300 K, above T_B for this sample, is displayed in Figure 4.4b. The sample exhibits a high initial susceptibility (χ_i), which is labeled along with the M_s .

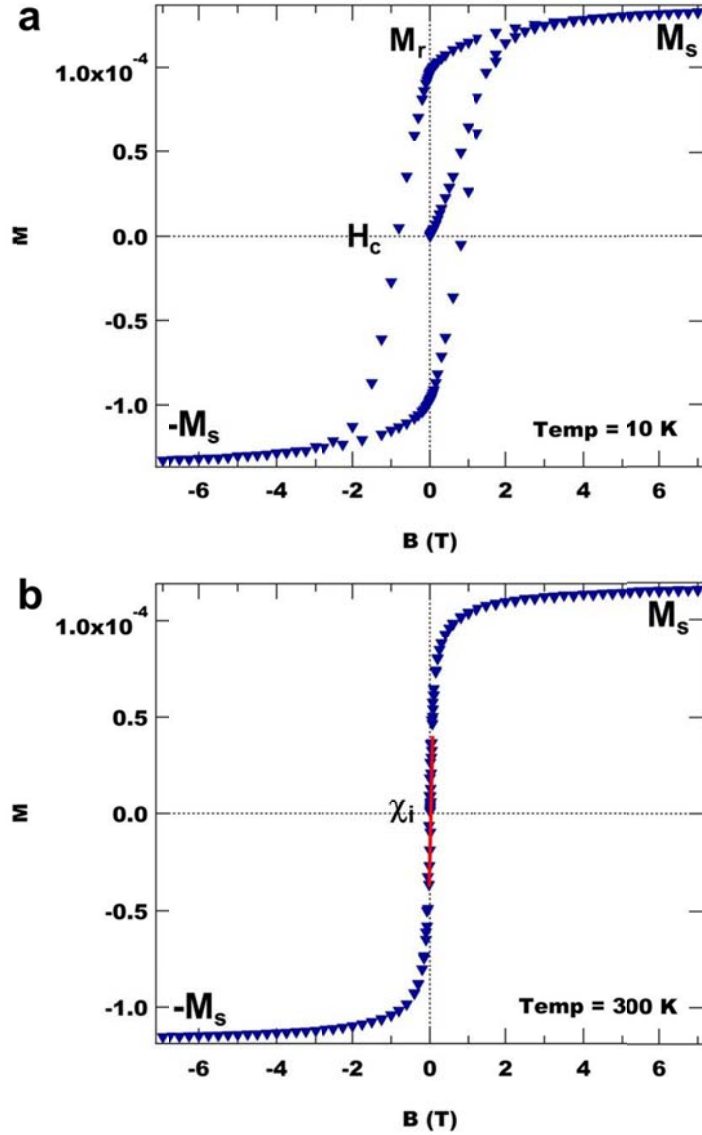


Figure 4.4: (a) $M(H)$ response of a ferrite nanoparticle sample below its T_B , where it exhibits hysteresis. The saturation magnetization, remanance magnetization, and coercive field are all labeled. (b) $M(H)$ response for the same sample above T_B . The sample's initial susceptibility and saturation magnetization are labeled.

The temperature dependent response of magnetic nanoparticles most often consists of two different curves: a zero-field-cooled (ZFC) curve and a field-cooled (FC) curve. These two sets of data enable the determination of where the magnetic behavior of the particles is reversible (in this case, superparamagnetic) or hysteretic. The particles should be immobilized so that only Néel relaxation (rotation of the particles' moments) and not Brownian relaxation (rotation of the particles themselves) can occur. This can be accomplished by dispersing the particles in a solvent and then freezing it, or by depositing the particles onto a fixed substrate or matrix material.

The ZFC measurement begins by rapidly cooling the nanoparticle sample to near 0 K in the absence of a magnetic field. At this point, the sample should consist of randomly oriented nanoparticles with their magnetic moments oriented along one of their easy directions. Next, a small field, generally 1 mT, is applied to the sample and the magnetization of the sample is measured as it is slowly warmed. As the thermal energy available increases, the particles' moments begin to align with the applied field. The sample's collective moment eventually reaches a maximum, which experimentally determines T_B . Above T_B , there is enough thermal energy to rotate the particles' magnetization away from the direction of the small applied field and the collective moment falls off as $1/T$.

In order to measure the FC curve, the sample is re-cooled. As the sample is cooled under the small applied field, it will retrace the ZFC curve to T_B . Below T_B , the particles' magnetizations become "blocked" and they remain in their maximally aligned state. Therefore, thermal (and field dependent) hysteresis is observed below T_B . Figure 4.5 shows the $M(T)$ response for an iron nanoparticle sample along with the key features of the ZFC and FC curves. Both the ZFC and FC curves can also be collected over a

range of measurement frequencies, but it is common to only measure the ZFC response as a function of frequency.

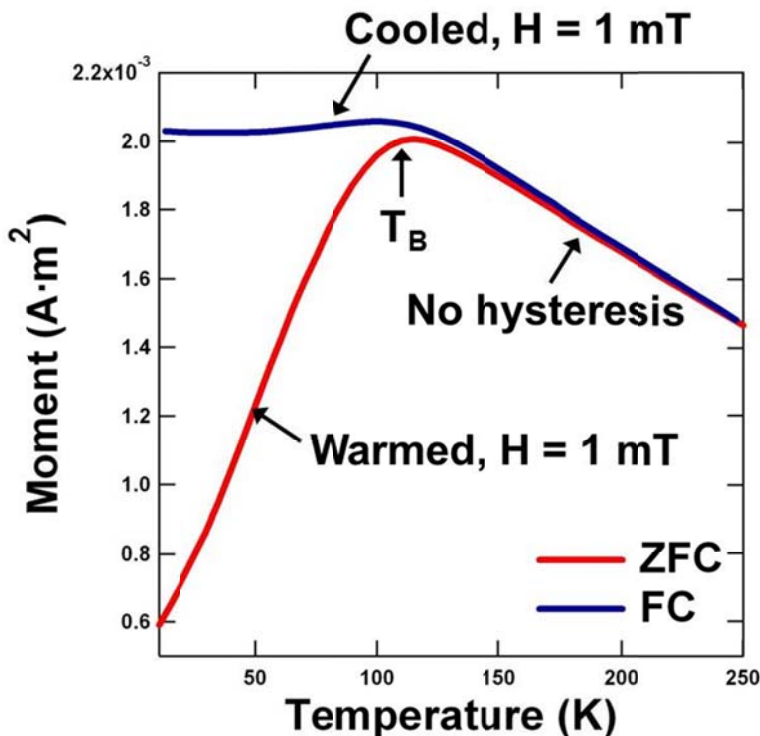


Figure 4.5: The $M(T)$ response of an ensemble of single domain iron nanoparticles. The blocking temperature is the peak in the ZFC data.

4.2 MAGNETIC CHARACTERIZATION OF FE NANOPARTICLES

4.2.1 Sample Preparation and Mounting

Both DC magnetization and AC susceptibility (χ) measurements were completed on a Quantum Design MPMS-7 SQUID magnetometer using samples of 1 wt% iron or less dispersed in frozen solvent (dioctyl ether). Temperature sweeps were performed by zero-field-cooling the sample and then measuring the magnetic moment as a function of temperature under the influence of a weak magnetic field (1 mT) during warming and subsequent cooling. AC magnetic susceptibilities were measured using an AC field of 0.35 mT and no DC field component. Precise masses for each sample were determined

destructively, by forming the phenanthroline/Fe²⁺ complex, and spectrophotometrically quantifying the concentration of a known dilution.[83] Magnetic data plotting, analysis, and fitting were performed using Igor Pro (WaveMetrics, Inc., Lake Oswego, OR, USA).

4.2.2 DC Magnetic Characterization

Due to the use of a surfactant that binds less strongly to the iron surface than ligands commonly used, nanoparticle samples with diameters of 5 nm or less synthesized with β -diketone surfactants have σ_{sat} values as high as 209 Am²/kg (for bulk iron σ_{sat} =222 Am²/kg at 0 K).[84] A magnetization curve of an iron nanoparticle sample with a volume average diameter of 5 nm determined through transmission electron microscopy (TEM) is displayed in Fig. 4.6. Based on the determination of the mass of Fe in this sample we estimate the σ_{sat} of the sample (at 5 K) to be 209 Am²/kg. Despite σ_{sat} values approaching bulk iron, our characterization below shows that these nanoparticles have an effective anisotropy that is more than an order of magnitude greater than bulk iron.

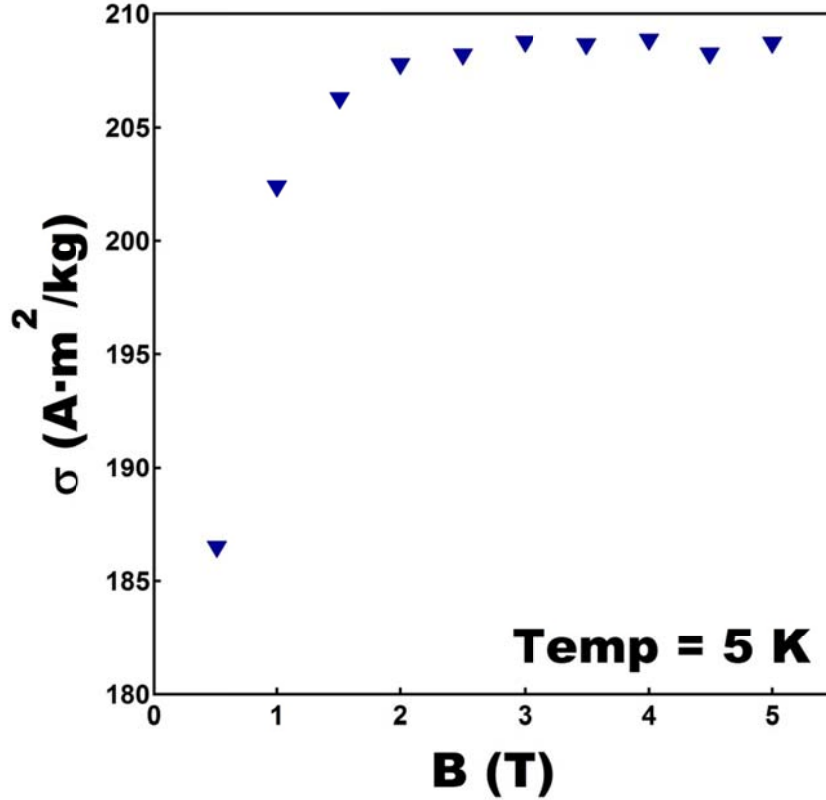


Figure 4.6: Mass magnetization curve of an ensemble of iron nanoparticles with a volume average diameter of 5 nm determined through transmission electron microscopy (TEM). Based on the determination of the mass of Fe in this sample we estimate the σ_{sat} of the sample (at 5 K) to be 209 Am²/kg.

The first indication that the iron nanoparticles studied had anomalously high magnetocrystalline anisotropies were their measured DC blocking temperatures (T_B), which were almost two orders of magnitude higher than what similarly sized nanoparticles with bulk iron's magnetocrystalline anisotropy would have. The T_B is the temperature at which a superparamagnetic particle's moment can reorient itself with the applied field in the timescale of the experiment. From the Néel-Brown model (2.7) for the relaxation of magnetic nanoparticles, it can be shown that blocking temperature depends on the product of the nanoparticle volume and anisotropy.[18] For the

magnetometer's DC measurement time (τ) of 100 s (which is typical for most instruments), the T_B for nanoparticles with cubic anisotropy follows the following equation:

$$T_B = \frac{K_1 V}{4k_B \cdot \ln(100/\tau_0)} \quad (4.1)$$

where K_1 is the first coefficient of magnetocrystalline anisotropy, V is the particle volume, k_B is the Boltzmann constant, and τ_0 is a constant referred to as the attempt time which should fall within the accepted range of $10^{-9} - 10^{-12}$ s.[18, 19, 56, 85-87] Figure 4.7 displays zero-field-cooled (ZFC) curves measured using DC magnetometry for iron nanoparticles with diameters of 2.3, 3.1, 3.4, and 4.5 nm (as determined by fitting the field dependent magnetometry data with a Langevin function and confirmed with TEM). Within the figure, moments are normalized for ease of comparison between data from different samples. Values of T_B can be recorded by determining the peak location in each ZFC curve. The values of T_B scale with the volume of the particles as Eq. (4.1) would indicate. Blocking temperatures from this DC magnetometry data are plotted as a function of particle diameter in Fig. 4.8. A dashed line of blocking temperatures resulting from a constant K_1 and $\tau_0=10^{-10}$ s is co-plotted with measured values of T_B and provided as a guide. These DC blocking temperatures are compared to a curve displaying the calculated blocking temperatures for hypothetical bcc Fe nanoparticles with a measurement time (τ) of 100 s, a value of $\tau_0=10^{-10}$ s, and the bulk value of K_1 for bcc iron. In all cases, T_B (and therefore K_1) for the synthesized Fe nanoparticles are well above those calculated using the values of bulk Fe. The measured blocking temperatures also lie along a line of constant anisotropy, suggesting that this anomalous property is not dominated by either surface effects (which would be strongest in the smallest

nanoparticles) or dipolar interactions (which should increase with larger particle diameters).

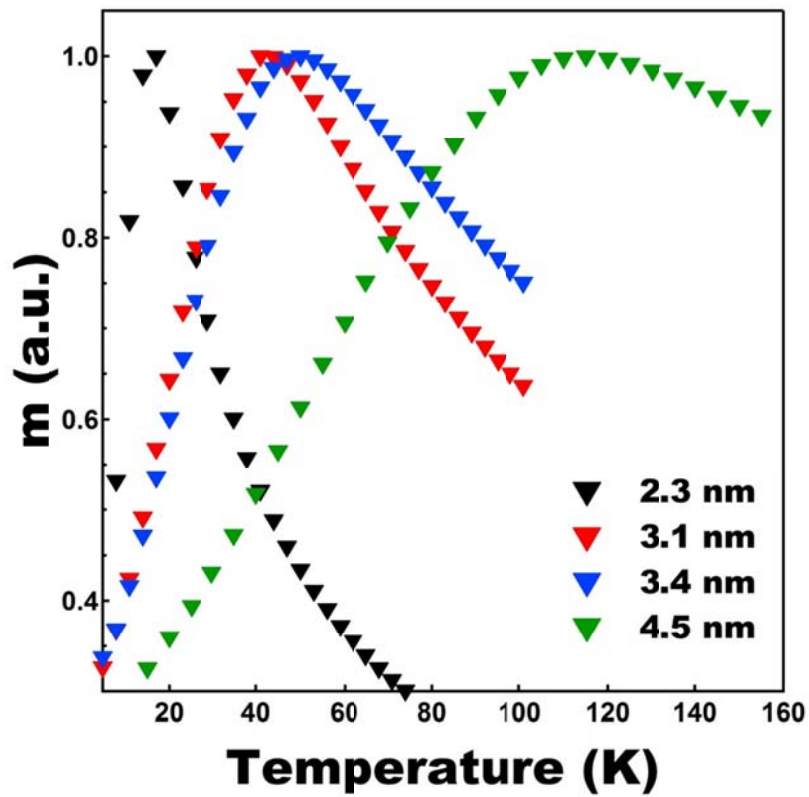


Figure 4.7: ZFC curves measured using DC magnetometry for nanoparticles with diameters of 2.3, 3.1, 3.4, and 4.5 nm. The moments for each curve are normalized for ease of comparison.

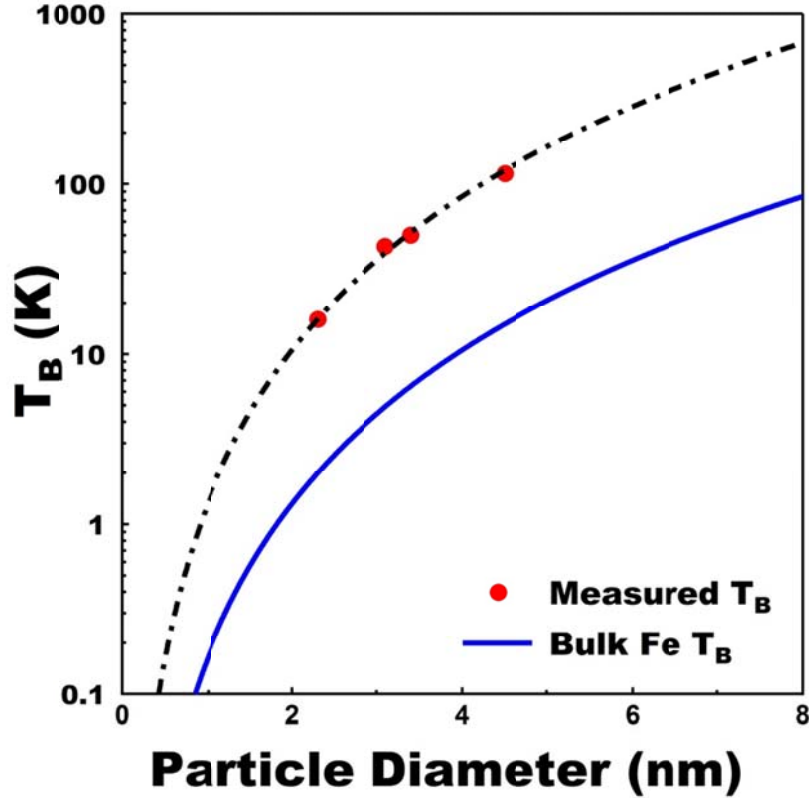


Figure 4.8: Plot of T_B vs. particle diameter for a series of Fe nanoparticles of different sizes. A dashed line of blocking temperatures resulting from a constant K_1 and $\tau_0=10^{-10}$ s is co-plotted with measured values of T_B and provided as a guide. These blocking temperatures are compared to a curve (solid blue line) displaying what theory would predict for bcc Fe nanoparticles assuming a measurement time (τ) of 100 s, a value of $\tau_0=10^{-10}$ s, and the bulk value of K_1 for bcc iron.

4.2.3 AC Magnetic Characterization

Next, AC magnetometry experiments were performed on all four samples of iron nanoparticles. The AC susceptibilities were measured in a series of ZFC curves at the following frequencies: 0.1, 0.3, 1, 3, 10, 30, 99.9, 300, and 997 Hz. Real (a) and imaginary (b) AC susceptibilities for a 2.3 nm diameter iron nanoparticle sample are displayed in Fig. 4.9. To improve readability, only five frequencies are plotted. From these curves we can determine the blocking temperature for the nanoparticle sample as a

function of the frequency of the applied field. In AC ZFC data, the experiment time is dictated by the frequency of the applied field, unlike DC ZFC data, where the time to reorient is the timescale of the experiment. Once again, we take T_B to be the peak moment in the ZFC data set.

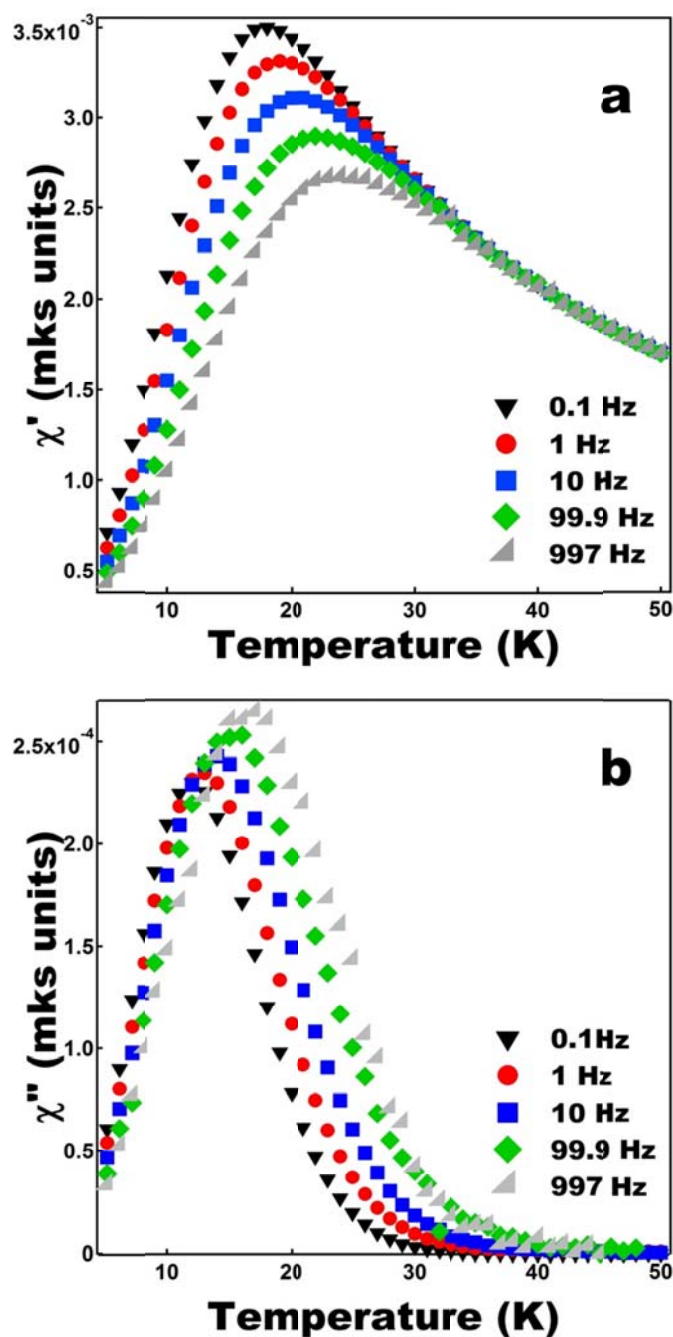


Figure 4.9: Real (a) and imaginary (b) AC magnetic susceptibilities (χ) of a 2.3 nm diameter iron nanoparticle sample. Data were also collected at 0.3, 3, 30, and 300 Hz but are not displayed.

Our AC data shows that the T_B increases with the measurement frequency, as expected in a thermally activated process. If the particles are assumed to be noninteracting, they should obey the Néel-Brown model, and the relaxation time (τ) can be plotted as a function of $1/T_B$ and fit with the following Arrhenius function (2.7)[56, 88]:

$$\tau = \tau_0 \exp\left(\frac{E_B}{k_B T}\right) \quad (4.2)$$

where τ_0 is the attempt time, E_B is the activation energy required to reverse a particle's magnetization, k_B is the Boltzmann constant, and T is the temperature in Kelvin (in this case T_B). E_B is equal to the product of the first coefficient of magnetocrystalline anisotropy (K_1) and the particle's volume (V) in the case of a material with uniaxial anisotropy. In the case of cubic anisotropy where the easy directions lie along the cube edges (as in bcc iron), K_1 should be replaced by $K_1/4$. [6, 18, 56, 89]

A plot of the natural logarithm of the relaxation time vs. $1/T_B$ for the set of 3.1 nm diameter iron nanoparticles is displayed in Fig. 4.10. From the slope of a linear fit (dashed line) to this data we determined the particles have a K_1 value of $7.7 \times 10^6 \pm 0.4 \times 10^6 \text{ Jm}^{-3}$, which is over two orders of magnitude greater than the value for bulk iron ($4.72 \times 10^4 \text{ Jm}^{-3}$). [57] From the Y-intercept, we determined that $\tau_0 = 4.1 \times 10^{-20} \pm 0.2 \times 10^{-20}$ s, which is too small to have physical meaning and far outside of the typical values of τ_0 ($10^{-9} - 10^{-12}$ s). [18, 19, 56, 85-87] Values of K_1 and τ_0 determined for the remaining samples (along with their mean diameters) are listed in Table 4.1. In all cases, K_1 is more than an order of magnitude higher than the magnetocrystalline anisotropy for bulk iron. However, since all of the determined values for τ_0 are well below the typically accepted range, the validity of the Néel-Brown model and the assumption of non-interacting

particles in our samples is brought into question. For this reason, we chose to evaluate our AC susceptibility data using additional methods.

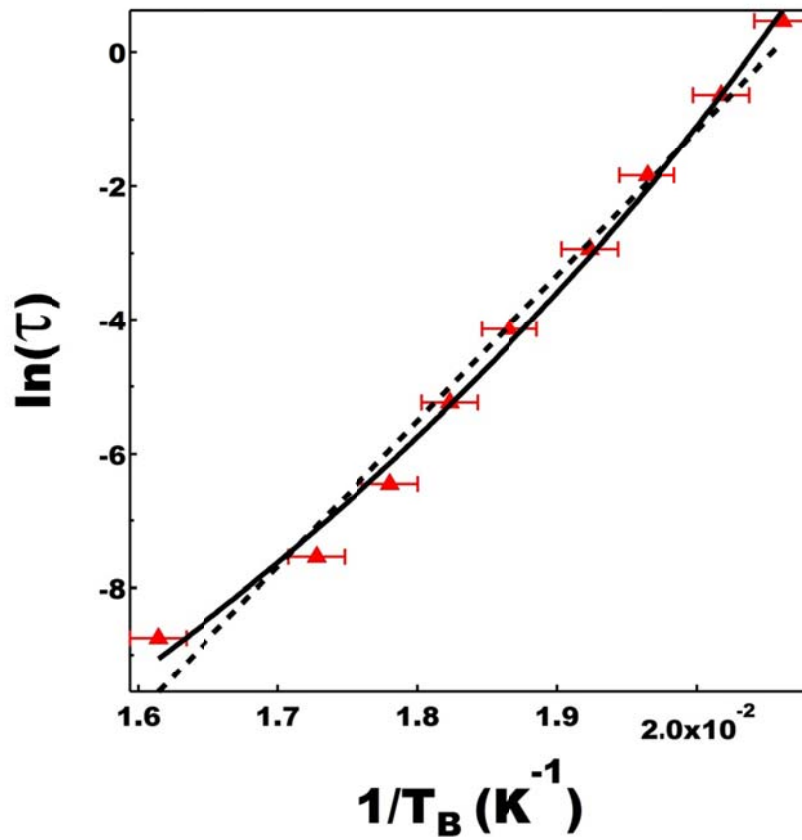


Figure 4.10: Plot of the natural logarithm of the relaxation time (τ) vs. $1/T_B$ for a 3.1 nm diameter iron nanoparticle sample. The data are fit with the Néel-Brown model described by Eq. (4.2) (dashed line) and the Vogel-Fulcher law described by Eq. (4.5) (solid line).

Sample		Néel-Brown		Spin-Glass Power-Law		
Diameter (nm)	Φ	τ_0 (s)	K_1 (10^6 Jm^{-3})	τ_0 (s)	T_g (K)	$z\nu$
2.3	0.08	1.1×10^{-14}	3.4 ± 0.1	1.3×10^{-4}	8.6 ± 0.2	10.2
3.1	0.06	4.1×10^{-20}	7.7 ± 0.4	6.5×10^{-7}	39.8 ± 1.7	9.6
3.4	0.06	5.9×10^{-20}	6.6 ± 0.2	1.6×10^{-6}	40.7 ± 11.3	13.5
4.5	0.05	5.2×10^{-25}	8.0 ± 0.4	3.4×10^{-6}	111.9 ± 11.6	5.5

Table 4.1: Fitted parameters for both the Néel-Brown and spin-glass power-law models along with values of Φ evaluated about $f = 30$ Hz.

In order to determine whether the nanoparticle samples were exhibiting spin-glass type behavior or that of interacting superparamagnetic nanoparticles we assessed the value of the model-independent empirical parameter Φ . This parameter relates the shift in the temperature of the maximum in χ' or χ'' (T_M) with the measured frequency, f , for an AC susceptibility data set using the following equation:

$$\Phi = \frac{\Delta T_M}{T_M \Delta \log_{10}(f)} \quad (4.3)$$

where ΔT_M is the difference between T_M measured in the $\Delta \log_{10}(f)$ frequency interval. For this set of samples, Φ was evaluated about $f = 30$ Hz (therefore the value of T_M at $f=30$ Hz was used). The values of Φ (also displayed in Table 4.1) for all of the iron nanoparticle samples lies within the range for interacting superparamagnetic nanoparticles (0.05 – 0.13), with a trend towards smaller values as the particle diameter increases.[6] This trend towards smaller values indicates that the degree of dipolar interaction increases with the particle size, however, values of Φ remain larger than those found in conventional spin glass systems (0.005 – 0.015).[89, 90]

Although the values of Φ suggest that T_M is varying with respect to changes in the measurement frequency more than in a spin-glass system, attempting to fit the data

with a spin-glass model could provide additional assurance that these nanoparticle systems are not acting collectively as a spin-glass. The data was fit with a model based on dynamical scaling near a phase transition, in this case, near the glass transition temperature, T_g . The equation describing this power-law behavior is:

$$\tau = \tau_0 \left[\frac{T_M}{T_g} - 1 \right]^{-zv} \quad (4.4)$$

Where once again, τ_0 is the attempt time, and T_M is the temperature of the maximum in χ' or χ'' . [90, 91] The product exponent zv is called the dynamical exponent. Fitting of the nanoparticle data with this power-law (plots not shown but fitting results are listed in Table 4.1) yielded good quality fits, however the values determined for τ_0 bring into question the validity of a spin-glass model for these Fe nanoparticle systems. Although all of the values found for the dynamical exponent (except for the 3.4 nm particle) are within the accepted range of values (4 – 12), [90] the values of τ_0 are all many orders of magnitude larger than the expected values ($10^{-10} - 10^{-14}$). [85] Because of these unphysical large values of τ_0 the existence of a phase transition to a glassy state in our samples can be discounted.

While a spin-glasslike state does not exist in the iron nanoparticle samples considered here, it is clear that there is a degree of dipolar interactions between the individual nanoparticles comprising each sample. The Vogel-Fulcher law accounts for dipolar interactions by including a term T_0 , which is the strength of the particle interaction (in K). The relaxation time is defined in the following manner using the Vogel-Fulcher law:

$$\tau = \tau_0 \exp \left[\frac{E}{k_B(T - T_0)} \right] \quad (4.5)$$

All terms except for T_0 are identical to the terms defined in the Néel-Brown model, or Eqn. (4.2). A plot of the Vogel-Fulcher model fit to the AC susceptibility data for the 3.1 nm sized sample can be seen in Figure 4.10 (solid line). This sample had a value of K_1 equal to $1.8 \times 10^6 \pm 0.4 \times 10^6 \text{ Jm}^{-3}$, $\tau_0 = 1.3 \times 10^{-11} \pm 0.1 \times 10^{-11} \text{ s}$, and $T_0 = 28.8 \pm 3.2 \text{ K}$. For all four sizes of iron nanoparticles, the Vogel-Fulcher model yielded excellent fits and the results can be seen in Table 4.2. As the diameter of the particles increased, their magnetocrystalline anisotropy remained constant, with a mean value of $1.9 \times 10^6 \pm 0.3 \text{ J/m}^3$. The degree of particle interaction (T_0) increased as the particles' diameter became larger, which is to be expected. However, the values of τ_0 remained within an acceptable range of physical values. The only sample for which a questionable value of τ_0 was measured was the 4.5 nm sample, whose value ($5.1 \times 10^{-14} \pm 1.7 \times 10^{-14} \text{ s}$) was outside of the most accepted range of ($10^{-9} - 10^{-12} \text{ s}$). [18, 19, 56, 86, 87] Other authors do suggest that reasonable values of τ_0 could be as low as 10^{-14} s . [85, 89] It is clear that from the value of T_0 ($65.4 \pm 25.4 \text{ K}$) and from its value of Φ discussed earlier, that this sample has the largest degree of dipolar interactions. The value of Φ for this sample (0.05) suggests that this particle has dipolar interactions strong enough that it is on the verge of becoming a weakly coupled spin-glass. For this reason, the Vogel-Fulcher law may not provide as good of a fit as with the other three Fe nanoparticle samples, which the larger errors of the fitted parameters suggest. Nevertheless, this sample's value of K_1 ($2.1 \times 10^6 \pm 1.5 \times 10^6 \text{ Jm}^{-3}$) is no larger than the three smaller samples.

Diameter (nm)	τ_0 (s)	K_1 (10^6 Jm^{-3})	T_0 (K)
2.3	3.0×10^{-12}	2.2 ± 0.9	2.8 ± 2.3
3.1	3.1×10^{-10}	1.4 ± 0.6	30.7 ± 4.4
3.4	1.3×10^{-11}	1.8 ± 0.4	28.8 ± 3.2
4.5	5.1×10^{-14}	2.0 ± 1.6	65.5 ± 25.4

Table 4.2: Parameters determined through fitting AC magnetometry data with the Vogel-Fulcher law.

A mean value of $K_1 = 1.9 \times 10^6 \text{ Jm}^{-3}$ for all the nanoparticle samples studied gives them a magnetocrystalline anisotropy over an order of magnitude greater than the value for bulk iron ($4.72 \times 10^4 \text{ Jm}^{-3}$). [57] Since the Vogel-Fulcher law accounts for dipolar interactions, the large anisotropy cannot be attributed to particle-particle interactions. If the large anisotropy was caused by a surface mediated effect, the values of K_1 should vary inversely with the particle diameter, but this was not the case. This lack of variation with size led us to explore the possibility that the enhanced anisotropy may be caused by some intrinsic material property of the nanoparticles.

Chapter 5

Synchrotron X-ray Characterization of Iron Nanoparticles¹

5.1 INTRODUCTION TO SYNCHROTRON RADIATION

Synchrotron radiation was originally considered a waste product and a nuisance to high energy physicists because the energy lost to this radiation had to be replaced by rf energy. However, over the past thirty years synchrotron radiation has had an enormous impact on many areas of science.

Synchrotron radiation is created by electrons of constant energy (on the order of a few GeV) that circle around a storage ring. The electrons are kept on the desired horizontal orbit by vertical magnetic fields generated by dipole electro-magnets which are located around the ring. Additional magnets, such as quadrupoles and sextupoles keep the electrons focused in a well-defined cross section.[92] Photographs of different magnets used in an electron storage ring are displayed in Figure 5.1.

¹ Portions of this chapter were submitted for publication in J. Magn. Magn. Mater. on 11/2/2011 and J. Appl. Phys. on 11/30/2011.

Magnets in electron storage rings

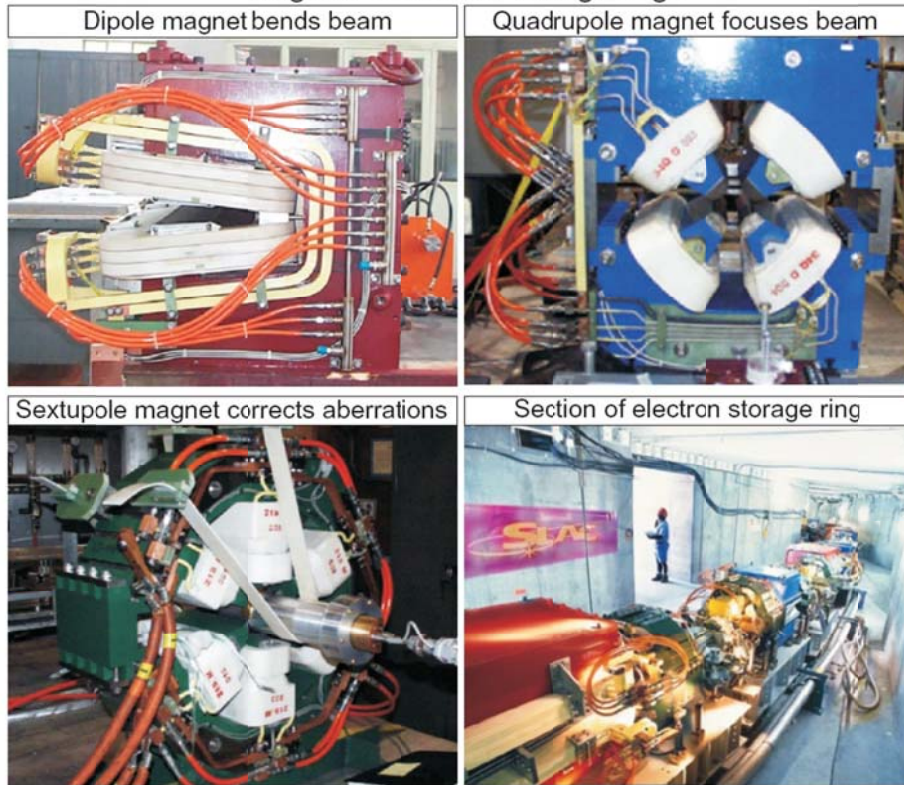


Figure 5.1: Electro-magnets used in electron storage rings. A complete magnet assembly from the Stanford Synchrotron Light Source (SSRL) is displayed on the bottom right. From Ref.[92]

For an electron moving in an electron storage ring, the radiation pattern emitted by the electron is quite different as observed from the rest frame of the charge and that of an observer at a large distance from the source (see Figure 5.2). In the rest frame of the electron ($v=0$), the radiation pattern has the shape of a donut centered about the axis defined by the acceleration vector \mathbf{a} . This is the dipole radiation pattern (left side of Figure 5.2). For an electron with an energy of several GeV it will be traveling with a velocity of $v \sim c$. In the case of a stationary observer, the radiation pattern becomes distorted and most of the intensity is emitted in the forward direction in a narrow cone of opening angle $2/\gamma$ (right side of Figure 5.2), where γ is defined as:

$$\gamma = \frac{1}{\sqrt{1 - \left(\frac{v}{c}\right)^2}} \quad (5.1)$$

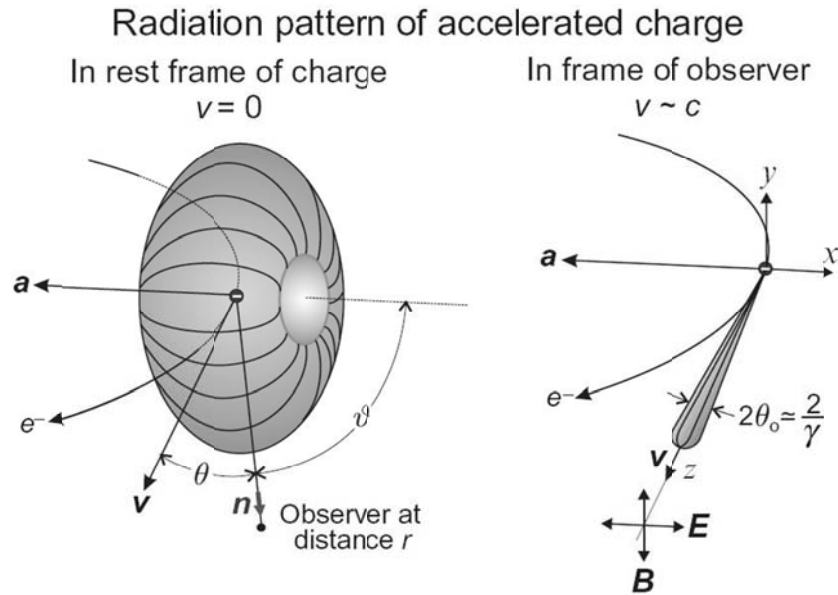


Figure 5.2: The radiation pattern of an accelerated charge in the rest frame of the charge (left) and in the frame of an observer (right). From Ref.[92]

The process for generating synchrotron radiation at Argonne National Laboratory's Advanced Photon Source (APS), where the synchrotron experiments described here were performed, is described below. The steps involved will be very similar at other synchrotron sources across the globe. Electrons for the synchrotron storage ring begin their journey in a linear accelerator (LINAC). There, electrons are emitted from a cathode heated to $\sim 1100^\circ\text{C}$. Next, the electrons are accelerated by high-voltage alternating electric fields inside the LINAC until they have an energy of 450 MeV. From the LINAC, electrons are injected into a booster synchrotron, which is a racetrack-shaped ring of electromagnets. There, the electrons are accelerated to 7 GeV

within a half second. From the booster synchrotron, the electrons are injected into the 1104 m circumference storage ring. The APS storage ring is comprised of 40 straight sections or sectors, brought together by bending magnets (dipole magnets). Five sectors are reserved for rf equipment and beam injection leaving 35 sectors for experimental setups. “Third generation” synchrotron storage rings such as the APS add insertion devices to their straight sections to enable a wide range of advanced experiments that require high X-ray flux and a tunable X-ray energy. Insertion devices include wigglers and undulators which are both constructed out of arrays of magnets. A diagram of a typical APS sector is displayed in Figure 5.3.

TYPICAL APS STORAGE RING SECTOR & FRONT END CONFIGURATION

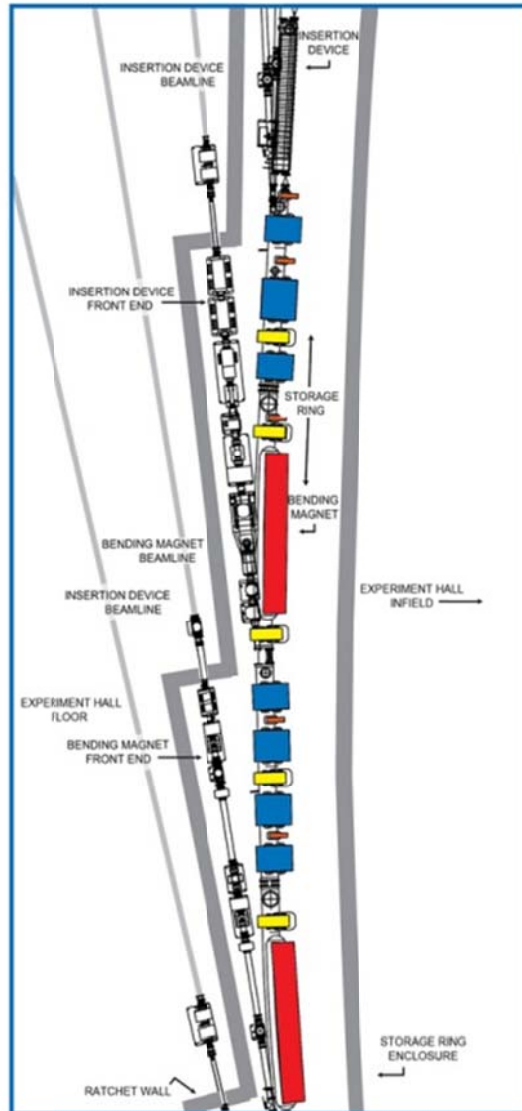


Figure 5.3: Diagram of a storage ring sector at APS. From Ref.

5.2 HIGH ENERGY XRD AND PDF EXPERIMENTS

When studied using laboratory based X-ray diffraction (XRD), nanoparticles produce diffraction patterns with a large diffuse component and only a few broad Bragg-like features.[94] This is due to their lack of long range order and often a more disordered crystalline structure at the local scale. Structural characterization methods

used to characterize a set of sharp Bragg peaks become impractical or impossible to use. However, through the use of high energy and high flux X-rays available from synchrotron storage rings it is possible to study the structural properties of nanoparticles, glasses, amorphous materials, and even liquids using the atomic pair distribution function (PDF). This is made possible by including the diffuse scattering intensity which in standard diffraction analysis is treated as ‘background’, curve-fitted, and discarded.[95] Including this diffuse scattering component is the total scattering method.

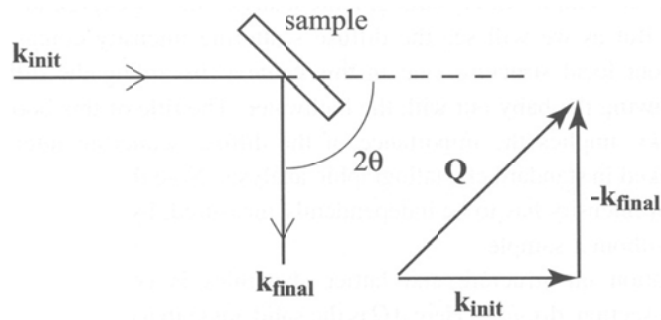


Figure 5.4: The geometry of a diffraction experiment showing the wave vector \mathbf{Q} and the scattering angle, 2θ . From Ref.[95]

The basis of the total scattering method is the measured scattering intensity from a sample. When this quantity is normalized, it becomes the total scattering structure function $S(\mathbf{Q})$, where \mathbf{Q} is defined as²:

$$\mathbf{Q} = \mathbf{k}_{\text{init}} - \mathbf{k}_{\text{final}} \quad (5.1)$$

The geometry of a diffraction experiment showing the wave vector \mathbf{Q} and the scattering angle, 2θ , is showing in Figure 5.4. The magnitude of \mathbf{Q} is given by:

$$Q = \frac{4\pi \sin \theta}{\lambda} \quad (5.2)$$

² Some textbooks will define \mathbf{Q} as $\mathbf{Q} = \mathbf{k}_{\text{final}} - \mathbf{k}_{\text{init}}$

The experimentally observable structure function can then be related to the coherent part of the total scattered intensity as follows[94, 96, 97]:

$$S(\vec{Q}) = 1 + \frac{[I^{coh}(\vec{Q}) - \sum c_i |f_i(\vec{Q})|^2]}{|\sum c_i f_i(\vec{Q})|^2} \quad (5.3)$$

where $I^{coh}(\mathbf{Q})$ is the coherent scattering intensity per atom in electron units and c_i and f_i are the atomic concentration and X-ray scattering factor, respectively, for the atomic species of type i . This quantity is often displayed as the reduced structure function:

$$F(\vec{Q}) = \vec{Q}[S(\vec{Q}) - 1] \quad (5.4)$$

The PDF is the Fourier transform of the reduced structure function:

$$G(r) = \left(\frac{2}{\pi}\right) \int_{Q=0}^{Q_{max}} \vec{Q}[S(\vec{Q}) - 1] \sin(\vec{Q}r) dQ \quad (5.5)$$

The PDF can also be written as:

$$G(r) = 4\pi r[\rho(r) - \rho_0] \quad (5.6)$$

where $\rho(r)$ and ρ_0 are the local and average atomic number densities, respectively, and r is the radial distance. In order to produce the most useful PDFs a Q range of $\sim 30 \text{ \AA}^{-1}$ and therefore synchrotron based radiation is required.[95] This contrasts with most lab X-ray diffractometers which use Cu K_α radiation at a wavelength of 1.54 \AA and are limited to a maximum Q of about 8 \AA^{-1} .

5.2.1 Sample and Data Handling

High-energy X-ray diffraction experiments were carried out on beamline 11-ID-C at the Advanced Photon Source (APS), Argonne National Laboratory using X-rays of energy 114.496 keV ($\lambda=0.1083 \text{ \AA}$) and a 2 dimensional detector (mar345 image plate). For the diffraction measurements, iron nanoparticles in dioctyl ether were sealed in glass

capillary tubes under an inert atmosphere. The high flux from the synchrotron radiation X-ray source allowed us to measure the weak diffraction patterns of our iron nanoparticles with very good statistical accuracy. Additionally, the higher energies of synchrotron X-rays made it possible to reach higher scattering vectors (Q). Both the high flux and ability to reach high Q are necessary for the success of the atomic pair distribution function (PDF) analysis described here.[95] The X-ray data reduction and conversion to atomic PDFs was completed using the program RAD.[98] Structure modeling was performed using the program PDFFIT.[99] PDFFIT calculates the PDF from a structural model using the following relation:

$$G_c(r) = \frac{1}{r} \sum_i \sum_j \left[\frac{b_i b_j}{\langle b \rangle^2} \delta(r - r_{ij}) \right] - 4\pi r \rho_0 \quad (5.7)$$

where the sum goes over all pairs of atoms i and j within the model crystal separated by r_{ij} . The scattering power of atom i is b_i and $\langle b \rangle$ is the average scattering power of the sample. In the case of X-ray scattering b_i is the atomic form factor evaluated at a user-defined value of Q. In order to account for either thermal or static displacements from the average atomic positions each delta function in (5.7) can be convoluted with a Gaussian.

5.2.2 Experimental Results

In an effort to understand the anomalous anisotropy in these iron nanoparticles, we studied their atomic-scale structure using high-energy X-ray diffraction, analyzing the data using the PDF approach. Standard XRD could not provide data of sufficient quality for structural analysis of the iron nanoparticles (see Figure 5.5 for XRD data generated on a laboratory instrument which merges low Q data from a Cu target with high Q data from a Mo target). The plots of the experimental atomic PDF as a function of radial distance

and the curves generated from structure modeling appear in Fig. 5.6. The models were based on the crystal structure of bcc Fe. We studied three samples: micron sized (bulk) Fe, 10 nm diameter Fe nanoparticles, and 4.5 nm diameter nanoparticles. The results from the modeling of the data appear in Table 5.1. Both of the nanoparticle samples have a correlation length much less than their diameters, indicating that the bcc-type atomic ordering is not maintained across the entire nanoparticle. Both nanoparticle samples also have an expanded nearest neighbor distance and higher root-mean-square fluctuations in their atomic positions than bulk bcc iron. These results indicate that the nanoparticles have an expanded and distorted bcc-type structure.

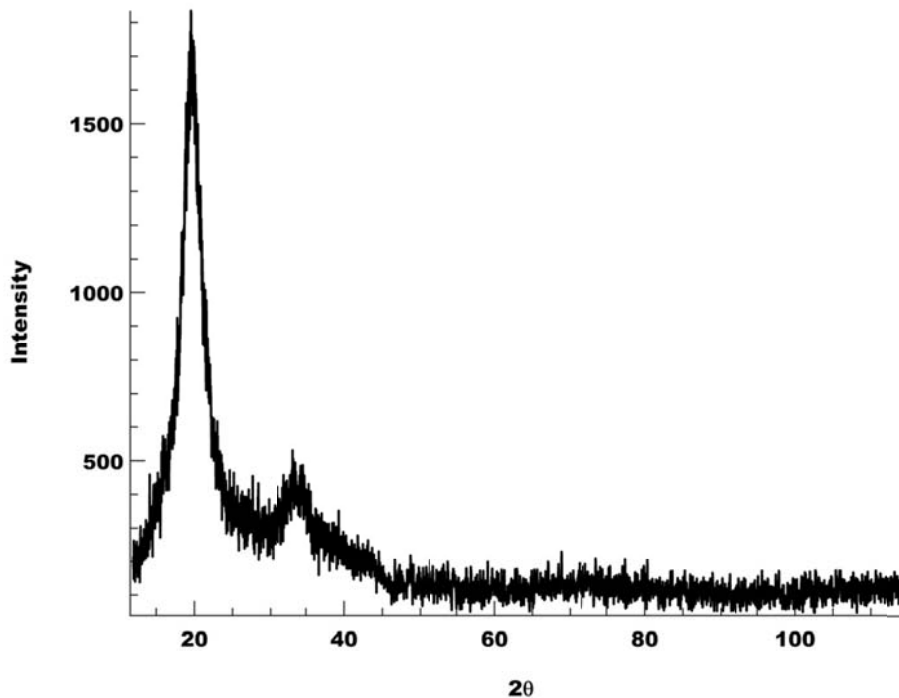


Figure 5.5: Plot of XRD data collected on a laboratory diffractometer. The data merges low Q data from a Cu target with high Q data from a Mo target.

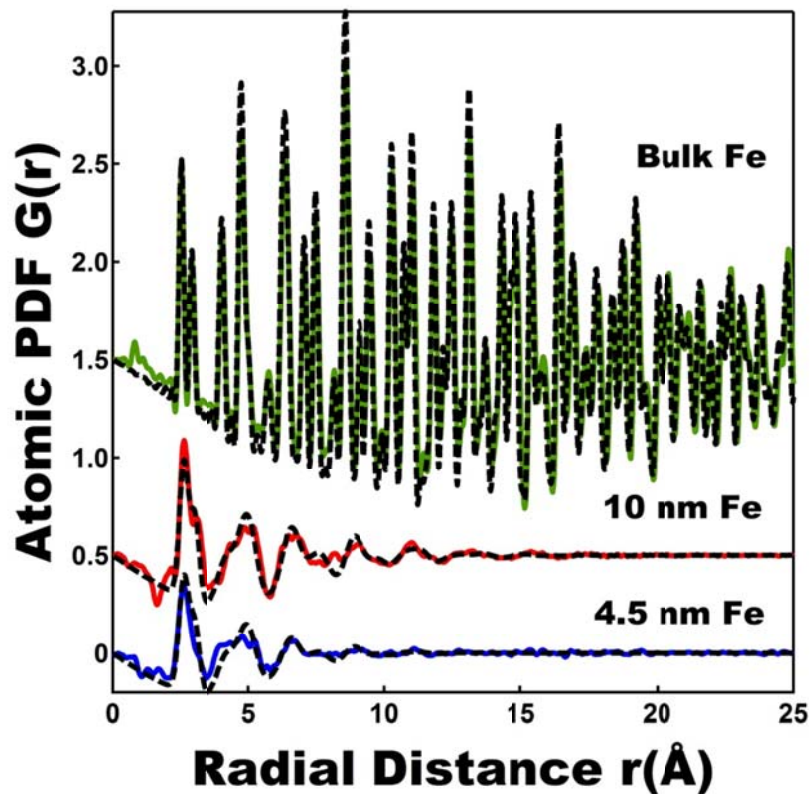


Figure 5.6: Experimental atomic PDF for a micron sized (bulk) iron sample and two iron nanoparticle samples. Model PDFs are displayed as a dashed black line.

Sample	Fe-Fe distance (Å)	Correlation Length*	RMS atomic position fluctuation (Å ²)**
Bulk Fe	2.48(1)	1 mm	0.005
10 nm Fe	2.56(2)	2 nm	0.052
4.5 nm Fe	2.56(2)	1 nm	0.052

*- The correlation length is estimated by the distance at which the experimental PDFs decay to zero.

** - RMS atomic fluctuations are estimated by a Gaussian fit to the first peak in the experimental PDFs. Note in bulk Fe they are mostly due to thermal disorder.

Table 5.1: Results from modeling PDF X-ray diffraction data of one bulk and two nanoparticle iron samples. The two nanoparticle samples are labeled according to their diameter.

5.3 XAFS EXPERIMENTS

X-ray absorption fine structure (XAFS) is related to how X-rays are absorbed by an atom at energies near and above the core-level binding energies of that atom.[100] More specifically, XAFS is caused by the modulation of an atom's X-ray absorption probability due to the chemical and physical state of the atom. The energy of the incoming X-rays can be tuned such that they excite and study the environment surrounding a single element within a sample. These absorption spectra are sensitive to the absorbing atom's oxidation state, coordination chemistry, nearest neighbor distances and species, and coordination number. XAFS probes the immediate environment of the selected element, to within about 6 Å. Unlike XRD, the theory and interpretation of XAFS does not rely on any assumption of periodicity or symmetry. For this reason, XAFS is a useful structural probe for nanocrystalline and highly disordered materials, including nanoparticles. The collection of X-ray absorption data is relatively straightforward as long as an intense and tunable source of X-rays is available. XAFS techniques were first developed in the early 1970s[101] and the technique continues to be widely used at synchrotron storage rings all over the globe.

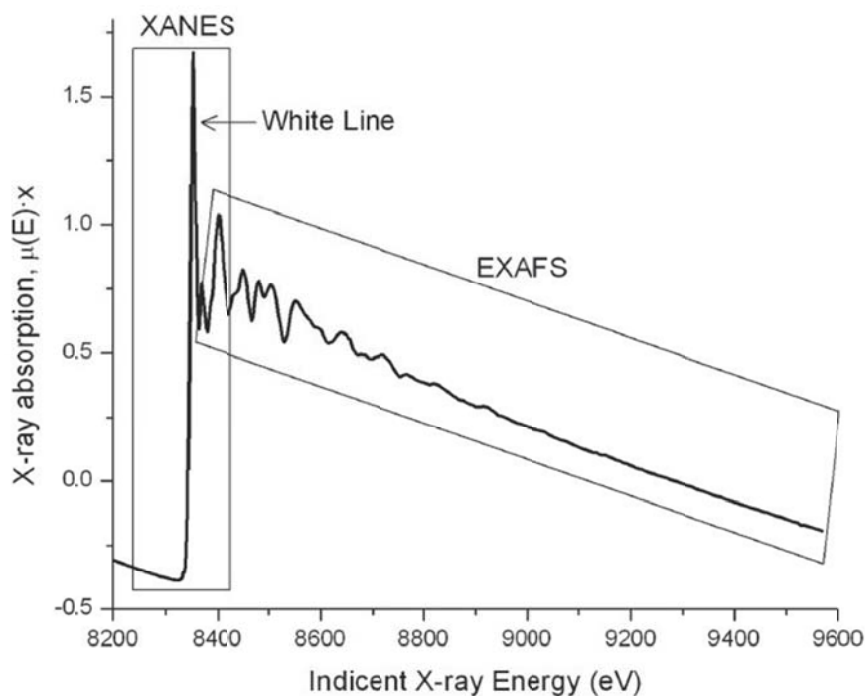


Figure 5.7: The X-ray absorption spectrum of NiO with the XANES region, EXAFS region, and white line noted. From Ref.[102]

XAFS is a method capable of providing the additional information desired regarding the nanoparticle/ligand interaction in a system of nanoparticles suspended in solution.[103, 104] X-ray absorption near edge structure (XANES), is particularly well suited for this study because of its sensitivity to the coordination chemistry and oxidation state of the absorbing atom. XANES is the part of the absorption spectrum near an X-ray absorption edge (equivalent to the binding energy of a core level electron), ranging from approximately -50 eV to +200 eV relative to the edge energy. Extended X-ray absorption fine-structure spectroscopy (EXAFS) is able to provide complimentary information including bond distances, number and type of atoms in coordination with the absorbing atom, and the degree of bonding disorder.[102] The EXAFS portion of the X-ray absorption spectrum is the normalized oscillatory part of the absorption coefficient above

the absorption edge to approximately 1000 eV or even higher. Figure 5.7 shows the X-ray absorption edge, XANES region, and EXAFS region for a NiO sample. The data was collected near the Ni K-edge. The absorption edge, which is the step-like part of the absorption spectrum, for this NiO sample has a strong peak referred to as a “white” line.

When the X-ray absorption process excites a core level electron in an atom with neighbors, the excited photo-electron can scatter from electrons of the neighboring atoms. The scattered photoelectron can then return to the absorbing atom and affect the availability of electronic states in the absorbing atom. This means that the photoelectron scattered back from the neighboring atoms will alter the absorbing atom’s absorption coefficient. This process is the origin of XAFS, which is described further in Figure 5.8 with the example of the absorption spectrum of NiO.

The XAFS spectrum of NiO is displayed in Fig. 5.8a. Below the absorption edge of NiO (approximately 8333 eV), incoming X-rays do not have sufficient energy for the creation of a photoelectron (see Figure 5.8b). If the arriving X-rays have an energy above the absorption edge core level electrons are promoted to the continuum (Fig. 5.8c and 5.8d). The kinetic energy of the ejected photoelectrons will equal the difference between the incident X-ray energy and the electron binding energy. These photoelectrons can be described as spherical waves propagating outward from the absorbing atoms (see Fig. 5.8c and 5.8d), which can then scatter from the neighboring atoms and change the absorption coefficient of the absorber atom. The absorption coefficient is determined by the relative phase of the outgoing photoelectron wave and the scattered wave, which is determined by the photoelectron wavelength and the distance between the absorbing and scattering atoms. If these waves are out of phase (Fig 5.8c), a minimum in absorption occurs, resulting in a drop in the XAFS spectrum. As the incident X-ray energy is increased the photoelectron wavelength becomes shorter and the

waves will progressively become in phase (see Fig 5.8d), resulting in a maximum in the XAFS spectrum. This sequence of minima and maxima in the oscillatory part of the XAFS spectrum produces the EXAFS oscillations.

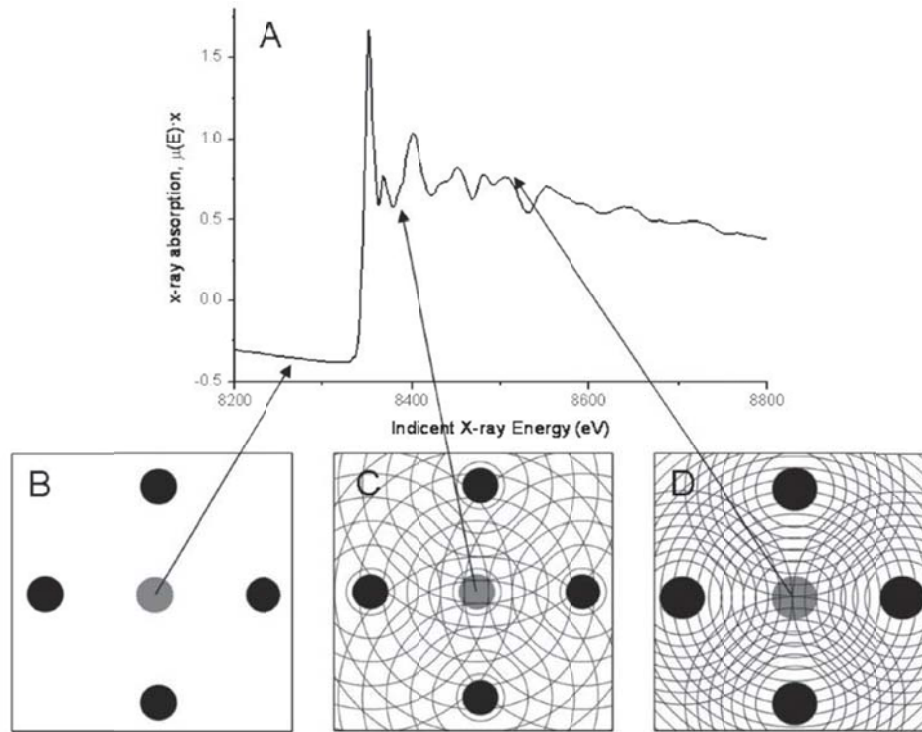


Figure 5.8: Illustration of the X-ray absorption process using data from a NiO sample. From Ref. [102]

When studying EXAFS, we are interested in these oscillations above the absorption edge and can define the EXAFS fine-structure function $\chi(E)$ as:

$$\chi(E) = \frac{\mu(E) - \mu_0(E)}{\Delta\mu_0(E)} \quad (5.8)$$

where $\mu(E)$ is the measured absorption coefficient, $\mu_0(E)$ is a smooth background function representing the absorption of an isolated atom, and $\Delta\mu_0$ is the measured jump in the absorption $\mu(E)$ at the absorption edge energy, or E_0 (see Figure 5.9).

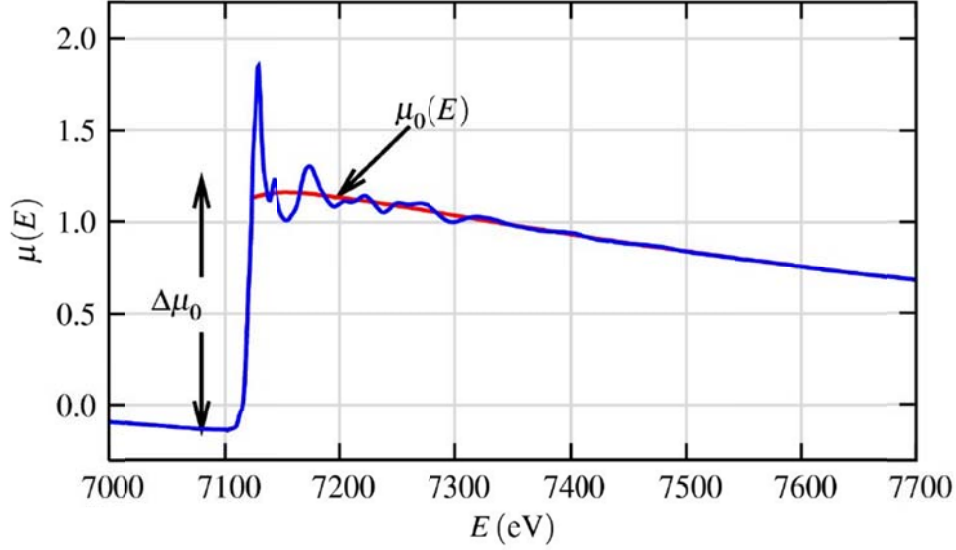


Figure 5.9: Plot of XAFS spectrum for a FeO sample. $\mu(E)$ is shown with a smooth background function $\mu_0(E)$ and the edge-step $\Delta\mu(E_0)$. From Ref.[100]

Due to the wave nature of the photoelectron, it is common to convert the X-ray energy to k , or the wave number of the photoelectron. The photoelectron's wavenumber has units of 1/distance and is defined as:

$$k = \sqrt{\frac{2m(E - E_0)}{\hbar^2}} \quad (5.9)$$

where m is the electron mass. The EXAFS, or $\chi(k)$, can then be described and modeled according to the EXAFS equation[105-107]:

$$\chi(k) = \sum_j \frac{(N_j S_0^2) e^{-2k^2 \sigma_j^2} e^{-2R_j / \lambda(k)} F_{eff_j}(k)}{k R_j^2} \sin[2kR_j + \varphi_j(k)] \quad (5.10)$$

where the summation is over all scattering paths of the photoelectron. The terms $F_{eff}(k)$, $\varphi_j(k)$, and $\lambda(k)$ are the effective scattering amplitude of the photoelectron, the photoelectron's phase shift, and the photoelectron's mean free path, respectively. R_j is the half path length of the photoelectron. For single scattering events, N_j is the number of

coordinating atoms within a particular coordination shell (group of atoms at the same radial distance from the absorber atom). In the case of multiple scattering events, N_j represents the number of identical paths. S_0^2 is the passive electron reduction factor which accounts for the slight relaxation of the remaining electrons in the presence of the core hole vacated by the photoelectron. σ^2 is the mean-square displacement of the bond length between the absorber atom and the coordination atoms in a shell. The σ^2 term accounts for both dynamic (thermal) and static (structural heterogeneity) disorder. The exponential term which includes $\lambda(k)$ in its argument causes the EXAFS signal to be dominated by scattering contributions from atoms within 10 Å or less of the absorber atom.

5.3.1 Sample Preparation

Experiments were carried out at the bending magnet beamline (5-BM-D) operated by the DuPont–Northwestern–Dow Collaborative Access Team (DND-CAT) at the Advanced Photon Source (APS) of Argonne National Laboratory (Argonne, IL). The beamline uses a Si(111) monochromator for energy selection. The energy resolution at the Fe K-edge (7112 eV) is ~1.0 eV. During the X-ray absorption measurements, the synchrotron storage ring was operated in the “top-up” mode, with the electron beam current kept at ~100 mA. The X-ray beam size in the experimental station is selected by two sets of Huber slits that are $2 \times 8 \text{ mm}^2$. The X-ray energies were calibrated by using an Fe standard measured in transmission.

Particles with PD surfactants were synthesized with $\text{Fe}(\text{CO})_5$:PD molar ratios of 13:1 and 35:1. Particles with C12E6 surfactants were synthesized with $\text{Fe}(\text{CO})_5$:C12E6 molar ratios of 1:1 and 11:1. This provided both a “small” and “large” sample with each choice of ligand to help distinguish between surface and bulk effects in the XAFS data.

Table 5.2 lists the samples used for this study in addition to their Fe(CO)₅ to ligand ratio and volume average diameter.

Sample Name	Surfactant	Fe(CO) ₅ :ligand molar ratio	Vol. Avg. Diameter (nm)
PD-13to1	PD	13:1	4.48 ± 1.00
PD-35to1	PD	35:1	6.97 ± 1.84
C12E6-1to1	C12E6	1:1	8.85 ± 2.31
C12E6-11to1	C12E6	11:1	10.55 ± 1.32

Table 5.2: Details of the iron nanoparticle samples studied with XAFS.

Iron nanoparticle samples for XAFS were prepared in a glove box by adding 1.5 mL of nanoparticles suspended in either dioctyl ether or octadecene to a 2 mL screw top microcentrifuge tube from VWR (Radnor, PA). An Oxford Instruments Isis 300 energy dispersive X-ray spectrometer (EDS) equipped with an ultrathin window and mounted on a JEOL 5800 LV SEM was used to verify that the centrifuge tubes did not contain iron impurities within the detection limit of the EDS. The centrifuge tube caps were wrapped in Parafilm “M” and the tube placed inside a clear plastic bag which was then heat sealed. For shipment to APS, the samples were heat sealed inside two mylar foil bags with a desiccant pack and oxygen absorber (IMPAK Corp.; Los Angeles, CA). Just prior to measurement, the outer two mylar foil bags were removed and the sample was placed in the beamline under a plastic bag filled with flowing nitrogen. The nanoparticle samples were measured in fluorescence mode. Photographs of the XAFS experimental setup and a close in picture of the Fe nanoparticle sample mounting are displayed as Figures 5.10 and 5.11, respectively.

In addition to the nanoparticle samples, foils of Fe, FeO, Fe₂O₃ and Fe₃O₄ were measured in transmission. Powders of Fe(II) acetylacetonate (Fe(II)acac) and Fe(III) acetylacetonate (Fe(III)acac) were deposited on kapton tape and measured. Fe(II)acac was measured in transmission and Fe(III)acac was measured in fluorescence. Fe(CO)₅ was sealed inside a microcentrifuge tube and measured in fluorescence mode. These standards were used in analyzing the XANES data using linear combination fitting (LCF).

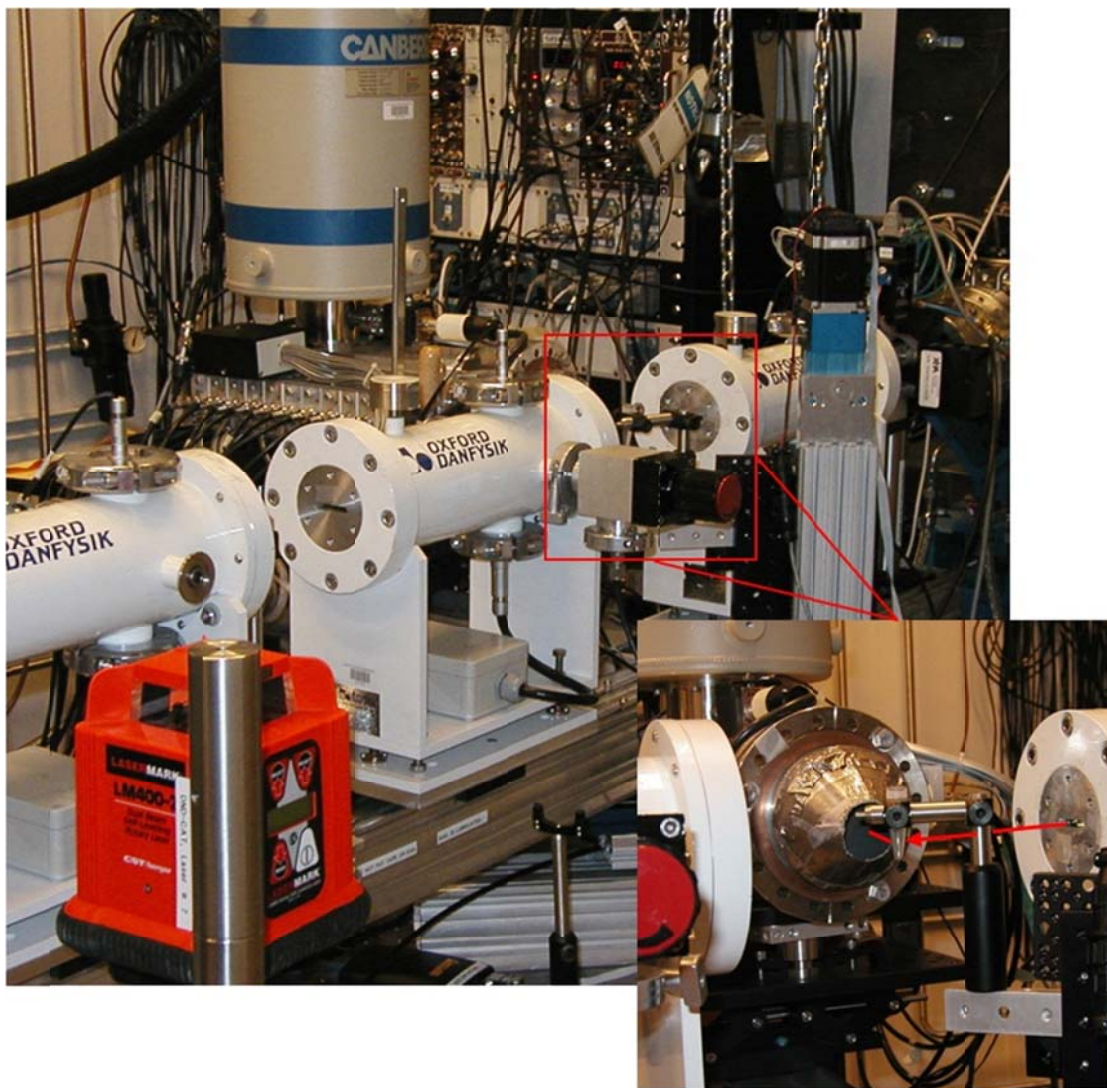


Figure 5.10: Photograph of XAFS experimental setup. The X-ray beam path and path from the sample to the fluorescence detector are shown in the inset photograph.

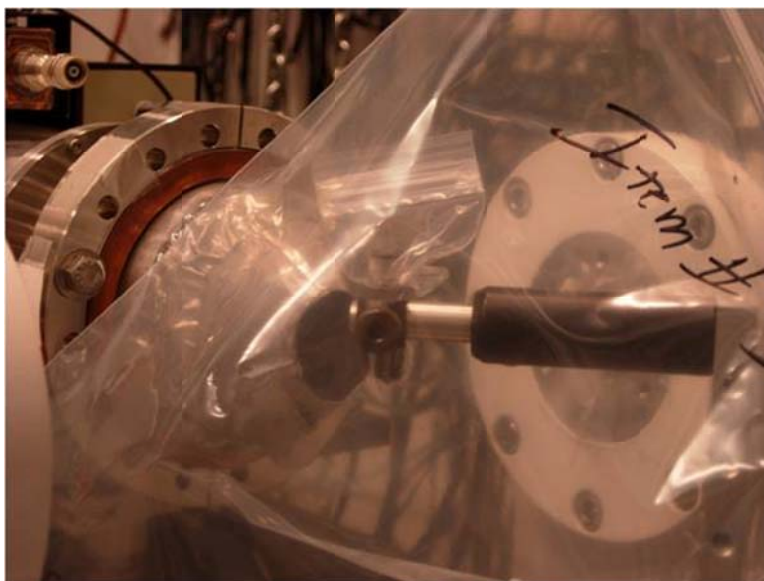


Figure 5.11: Close in photograph of iron nanoparticle sample mounting used for XAFS experiments.

The incident X-ray intensity was monitored by an ion chamber (Oxford Danfysik; Oxford, UK). A 13-element Ge solid-state detector (Canberra; Meriden, CT) was used to collect the fluorescence emissions of Fe K_{α} to obtain XANES and EXAFS spectra at room temperature. Digital X-ray process electronics (DXP2X) from XIA LLC (Hayward, CA) are used for X-ray pulse processing, which provides precise deadtime correction within a given experimental condition. Typically, 12-15 energy scans were averaged to obtain sufficiently good data statistics. The XANES spectra allow determination of the coordination chemistry and oxidation state of the absorbing Fe atoms. The EXAFS spectra reveal the interatomic distances (R), the root mean squares of the bond distance spread (σ^2), and the coordination numbers (N) around each absorbing atom.[102, 104] XAFS data was analyzed using the Horae and Ifeffit software packages.[108, 109]

All plots were generated using Igor Pro software (WaveMetrics, Inc.; Lake Oswego, OR, USA). Additional image rendering was completed using Inkscape (public domain software, Inkscape Project; New York, NY).

Extreme care was taken during sample preparation, transport, and measurement to avoid any exposure to conditions which could oxidize the iron nanoparticles. For each sample, no evidence of oxidation or radiation damage could be observed over the maximum of 15 energy scans (a total data collection time of approximately 10 hrs.)

5.3.2 XANES Experimental Results

XANES data for samples PD-13to1 and PD-35to1 are displayed in Figure 5.12 and 5.13, respectively. In addition to the spectra from the Fe nanoparticle sample, spectra from the references that produced a best linear combination fit (scaled according to their contribution to the fit) and the fit itself are also plotted. The linear combination fitting (LCF) range for all samples was from 10 eV below to 30 eV above E_0 (chosen as the zero crossing in the second derivative of the absorption edge). Additionally, for all fits E_0 was kept fixed and the addition of a linear term after E_0 was not allowed. Initially, all of the standards measured were included as a potential contributor to a best fit.

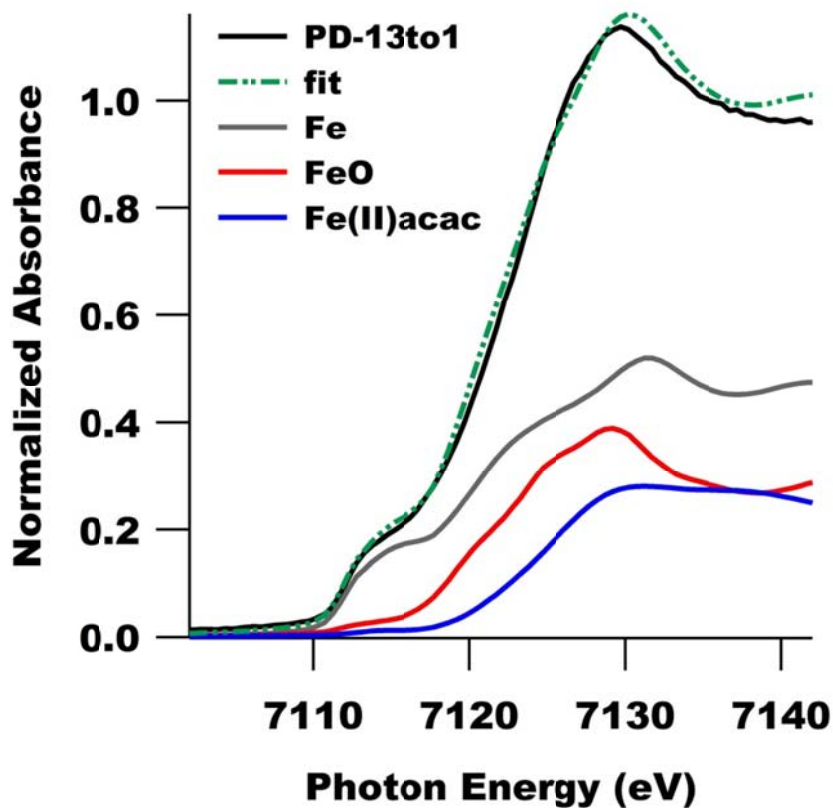


Figure 5.12: XANES spectra of sample PD-13to1. Also displayed are the linear combination fitting (LCF) results along with the reference spectra used to produce the fit (scaled according to their contribution to the fit).

Details of the best fit to the XANES data from all Fe nanoparticle samples is displayed in Table 5.3. Although $\text{Fe}(\text{CO})_5$ was present as a reagent in the nanoparticle synthesis, it quickly became clear during the fitting process that none of the Fe particles contained any appreciable amount of $\text{Fe}(\text{CO})_5$, suggesting that the iron precursor had fully decomposed during the synthesis process. The best fits to the samples with PD ligands were found using a combination of spectra from Fe, FeO, and Fe(II)acac, identifying the key constituents of the nanoparticles synthesized with PD as Fe(0) and Fe(II). The amount of total Fe(II) present in these samples scales with the surface to

volume ratio of the particles. This leads us to believe that the Fe(II) species are occurring at the surface of the nanoparticles, leaving a core of Fe(0) at the center. Based on the amount of Fe(II) present, it extends approximately 2-3 atomic layers into the nanoparticle.

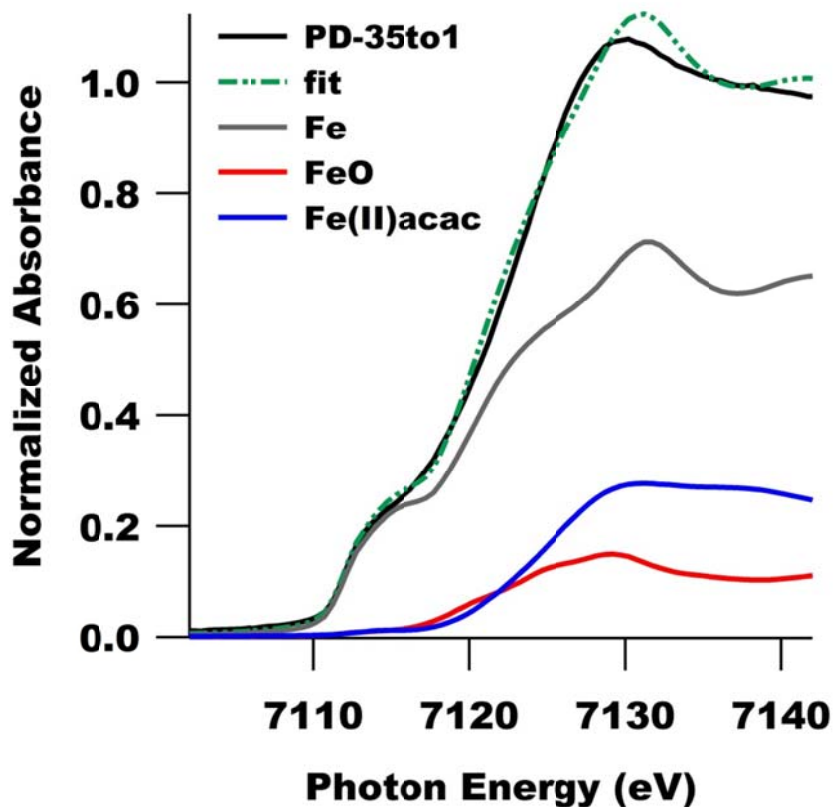


Figure 5.13: XANES spectra of sample PD-35to1. Also displayed are the linear combination fitting (LCF) results along with the reference spectra used to produce the fit (scaled according to their contribution to the fit).

The lack of any Fe(III) component also tells us something about the nature of the interaction between the PD ligands and the surface of the particles. Since a better fit resulted in both cases when Fe(II)acac was included, it can be concluded that the PD is forming a bond with strong ionic character at the particle surface, and appearing very

much like an acetylacetonate anion. Since the PD is interacting with iron atoms at the surface, more than two PD molecules would be sterically hindered from coordinating to a single iron atom. This would in part explain the lack of any Fe(III)acac at the nanoparticle surface. Since the best fits were produced using a combination of Fe(II)acac and FeO for the Fe(II) species, this suggests that electrons withdrawn by the PD ligands may be shared between neighboring Fe atoms.

Sample Name	Fe	FeO	Fe(II)acac	Fe ₂ O ₃	Fe ₃ O ₄
PD-13to1	49(2)	29(2)	22(1)		
PD-35to1	67(2)	11(2)	22(1)		
C12E6-1to1	20(2)			40(3)	40(4)
C12E6-11to1	62(2)	38(2)			

Table 5.3: XANES LCF fitting results (fitting results given in %).

LCF fits of the XANES data for particles synthesized with C12E6 revealed differences between the surface interactions of C12E6 and PD. Plots of the XANES data, reference spectra used in LCF, and best fit for samples C12E6-1to1 and C12E6-11to1 are displayed in Figure 5.15 and 5.16, respectively. Although Fe(II)acac and Fe(III)acac were tried as fitting standards, neither molecule contributed to the best fits. This was expected since PD was no longer present as a ligand and due to the difference in interaction between both PD and C12E6 with the iron surface.

Sample C12E6-1to1 was best fit with 20% Fe, 40% Fe₃O₄ and 40% Fe₂O₃. The large amount of Fe(III) species leads us to believe that this sample was oxidized during the synthesis process. We believe the oxidation occurred not due to improper air-free chemistry techniques but rather through the nanoparticles' interaction with excess C12E6

surfactant. With a $\text{Fe}(\text{CO})_5$ to C12E6 molar ratio of 1:1, excess surfactant would be available at the completion of nanoparticle synthesis and the terminal hydroxyl group of the C12E6 (see Figure 3.1) is a known oxidizer of iron.[110] The presence of Fe(III) was also confirmed via electron diffraction of the sample remaining in our lab, which was introduced into the TEM via a nitrogen purged antechamber. Selected area electron diffraction (SAED) of the sample shows a very strong iron oxide pattern, beyond what would be expected from oxidation in the HV TEM column (see Figure 5.16).

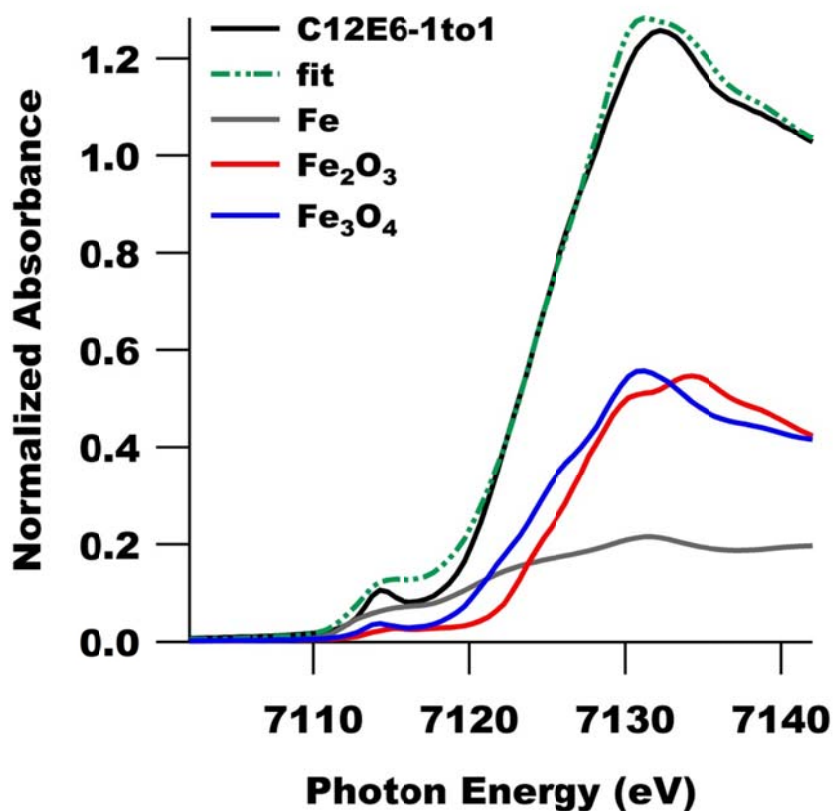


Figure 5.14: XANES spectra of sample C12E6-1to1. Also displayed are the linear combination fitting (LCF) results along with the reference spectra used to produce the fit (scaled according to their contribution to the fit).

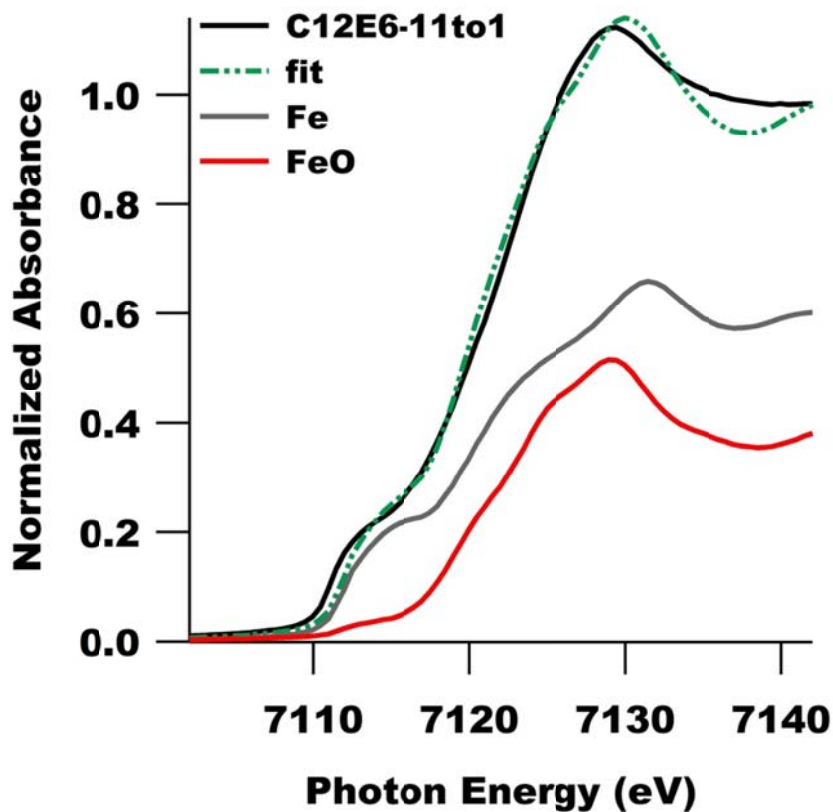


Figure 5.15: XANES spectra of sample C12E6-11to1. Also displayed are the linear combination fitting (LCF) results along with the reference spectra used to produce the fit (scaled according to their contribution to the fit).

The remaining sample, C12E6-11to1, was not oxidized during synthesis and provided insight into the nature of the interaction between the C12E6 ligands and the surface of the nanoparticle. A mixture of 62% Fe and 38% FeO yielded the best LCF results. As with the PD passivated particles, we believe the C12E6 coated particles consist of a core of Fe(0) and a shell of Fe(II). According to the amount of Fe(II) present, the oxidized species would penetrate further (approximately four atomic layers) into the surface of the nanoparticle. Once again, we believe the oxygen atoms in the ligand are interacting with the nanoparticle surface and withdrawing electrons from neighboring Fe

atoms. Since C12E6 is a large molecule and its interaction with the nanoparticle surface will also be sterically hindered, it is very likely that withdrawn electrons are again being shared by neighboring iron surface atoms as well as Fe atoms below the nanoparticle surface.

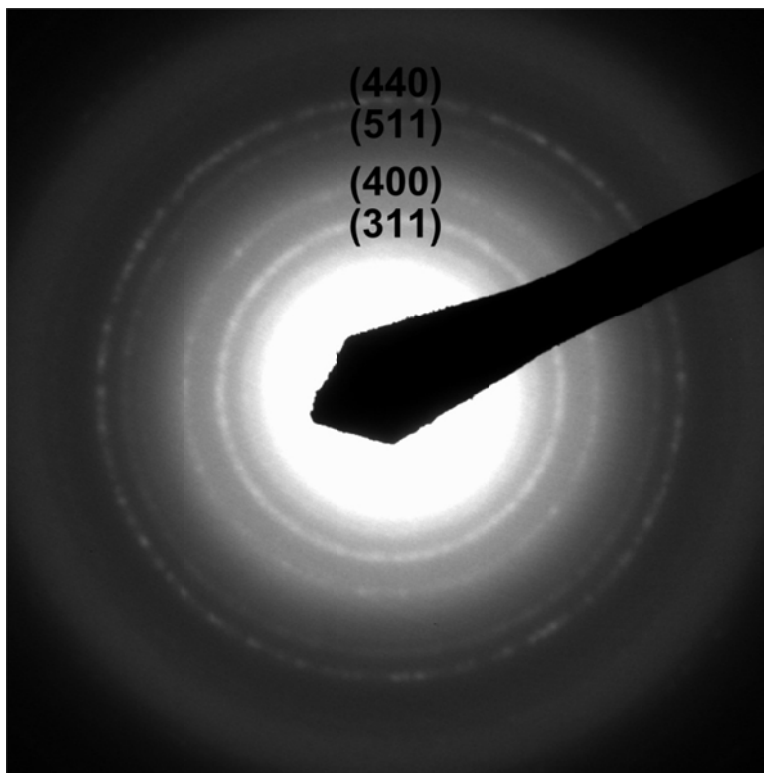


Figure 5.16: SAED of sample C12E6-1to1. The diffraction rings are labeled with the indices of either Fe_3O_4 or $\gamma\text{-Fe}_2\text{O}_3$ (the difference in lattice plane spacings between magnetite and $\gamma\text{-Fe}_2\text{O}_3$ are indistinguishable within $\pm 0.05 \text{ \AA}$).

5.3.3 Fourier Transform Infrared Spectroscopy (FT-IR) Complimentary Results

Fourier Transform – Infrared (FT-IR) spectra were obtained with a Bruker IFS 66v/s FT-IR spectrometer in an evacuated chamber. Fe nanoparticles and Fe(III)acac were pressed into a KBr pellet with a sample concentration of 2 % (w/w). PD (neat) was deposited between two KBr windows. All sample preparation was performed inside an

inert gas glovebox. The samples were then sealed in glass vials and taken immediately to the FT-IR sample chamber.

The presence of Fe(acac) like species at the surface of iron nanoparticles passivated with PD has also been observed using Fourier transform-infrared spectroscopy (FT-IR), where strong similarities exist between the spectra of Fe nanoparticles with PD ligands and Fe(III)acac. A plot of FT-IR spectra comparing iron nanoparticles with PD ligands to both Fe(III)acac and PD (neat) is displayed in Figure 5.17. Some absorption peaks visible in the Fe(III)acac spectra shown here (and in Fe(III)acac spectra reported in the literature) that are visible in the Fe nanoparticle spectra include: the C=C stretching vibration at 1573 cm^{-1} , C=O stretching mode at 1525 cm^{-1} , CC and CCH₃ stretch at 1275 cm^{-1} , CH₃ rocking mode at 1025 cm^{-1} , and CCH₃ and CO stretch at 930 cm^{-1} . [111-113] Of particular note is the Fe-O stretch visible at 660 cm^{-1} . This provides strong evidence that the PD interaction with the nanoparticle surface is ionic in nature.

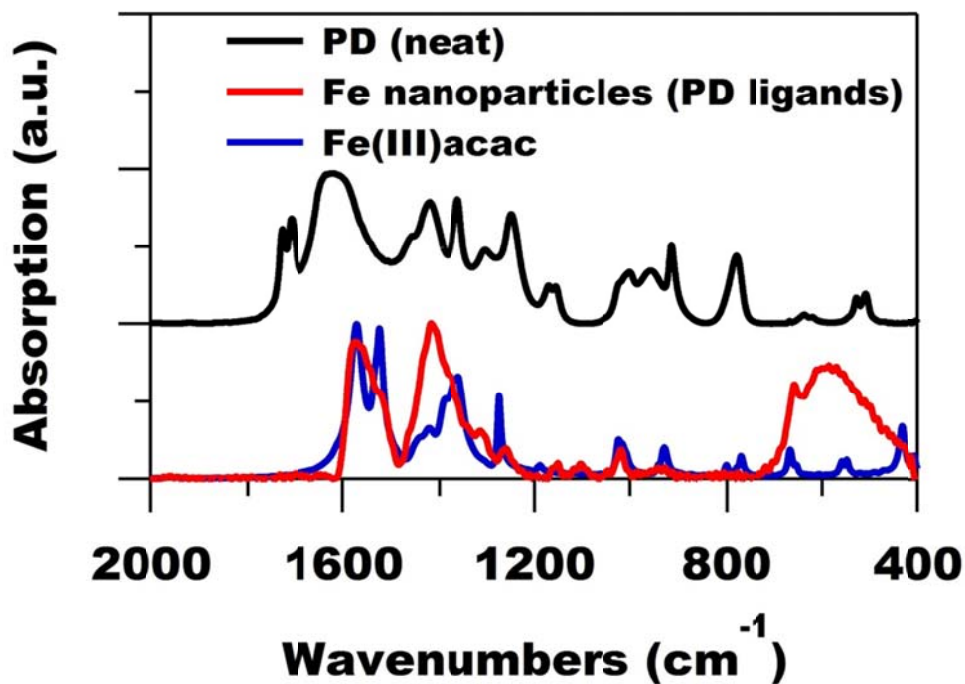


Figure 5.17: FT-IR spectra of Fe nanoparticles synthesized with PD surfactants and compared to the spectra of Fe(III)acac and PD (neat).

5.3.4 EXAFS Experimental Results

EXAFS analysis provided another method for assessing the amount of oxide present in the samples as well as the distance between neighboring iron and oxygen atoms. Prior to analyzing the data, background subtraction was performed using a minimum R-space distance, R_{bkg} , for the background spline of 1.0 Å and following the methods outlined by Newville *et al.*[114] Following subtraction of the background, the data were transformed into a function of photoelectron wavenumber, k . The EXAFS spectra are displayed in Figures 5.18 and 5.19, where the data have been multiplied by k^2 to compensate for the EXAFS amplitude falling off with increasing k . Particles synthesized with PD surfactants are displayed in Figure 5.18 and those with C12E6 surfactants are displayed in Figure 5.19. Since it was oxidized during synthesis, the

spectra of C12E6-1to1 shows a clear difference in relation to the other three samples. Despite the particles' small size, their higher degree of crystalline disorder as compared to bulk materials, and the necessity to measure the particles dispersed in a solvent to prevent oxidation during sample preparation and measurement, reasonably good quality EXAFS data were collected.

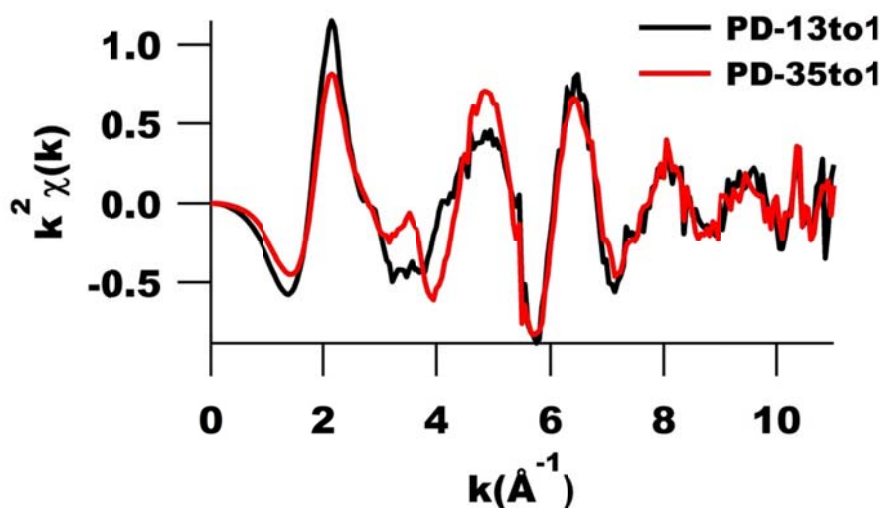


Figure 5.18: EXAFS spectra of Fe nanoparticles synthesized with PD surfactants.

The Fourier transform of the EXAFS data (multiplied by k^2) was taken over the range of $1.8 - 9.9 \text{ \AA}^{-1}$ using Hanning windows with sills of 1.0 \AA^{-1} in width. The data was then analyzed through fitting the spectra with ab initio theoretical standards for Fe and FeO using the EXAFS equation (5.10).[104-107] Although the XANES data of the PD coated particles were best fit by including both FeO and Fe(II)acac in the LCF, FeO was sufficient in the EXAFS analysis to account for Fe(II) species while minimizing the number of variables being fit. The magnitude of the Fourier transforms of the EXAFS data for PD coated particles (solid lines) and fits to these spectra (dashed lines) are displayed in Figure 5.20. Figure 5.21 shows the spectra and fit to sample C12E6-11to1.

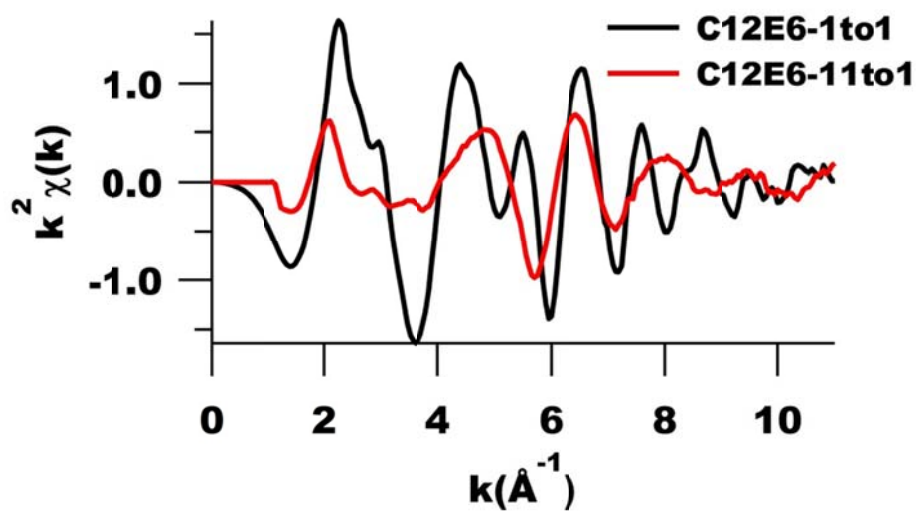


Figure 5.19: EXAFS spectra of Fe nanoparticles synthesized with C12E6 surfactants.

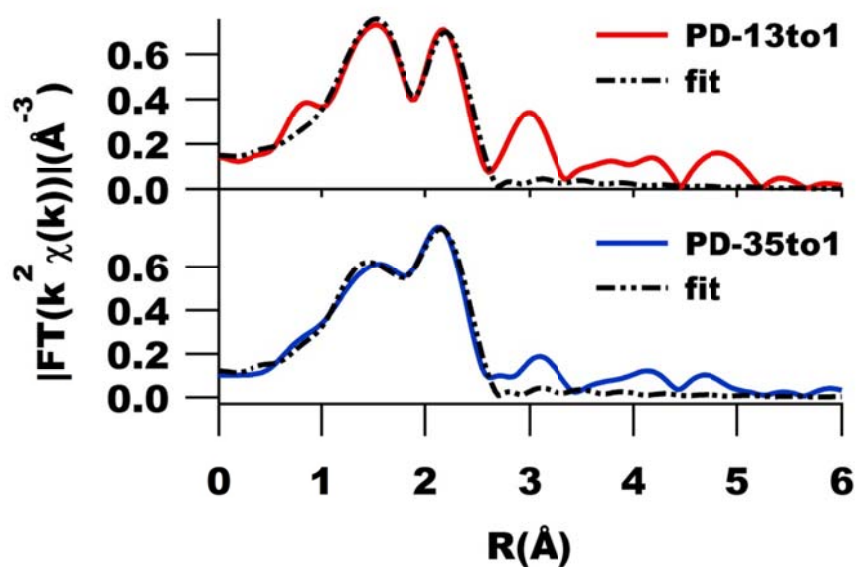


Figure 5.20: Plot of the magnitude of the Fourier transform of the EXAFS spectra (multiplied by k^2) of PD-13to1 (top) and PD-35to1 (bottom). Fits to both spectra are plotted as dashed lines.

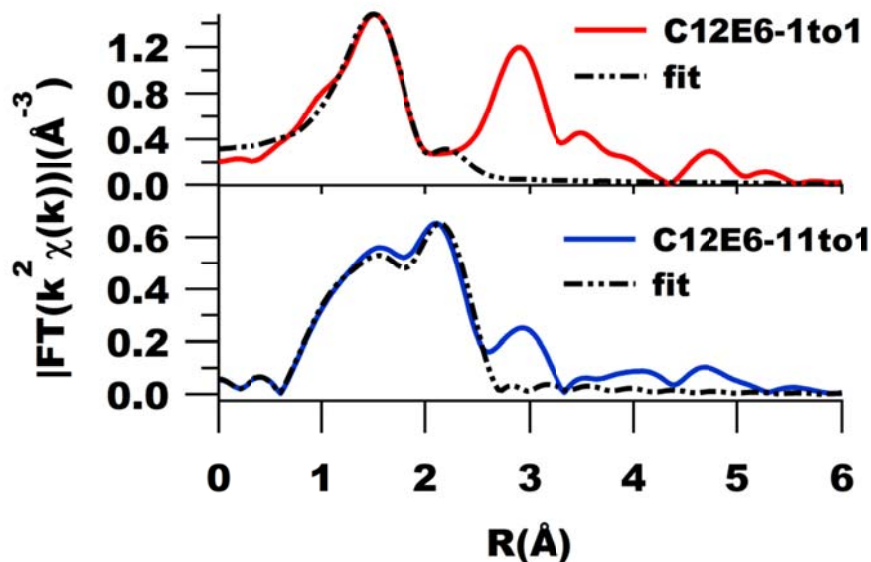


Figure 5.21: Plot of the magnitude of the Fourier transform of the EXAFS spectra (multiplied by k^2) of C12E6-1to1 (top) and C12E6-11to1 (bottom). The fits to both spectra are plotted as dashed lines.

Due to the noise present in the data and evidently small contribution from high coordination shells, only the first coordination shell of the Fe atoms were analyzed. A range of 1–2.6 Å, set using Hanning windows with sills of 0.5 Å in width, was used during the fitting. Given the way the EXAFS data were collected, coordination numbers determined will be less reliable. However, it is reasonable to assume that the errors induced by the non-ideal experimental geometry (refer to Figures 5.10 and 5.11) are the same for both Fe and FeO components. During the preliminary fittings, σ^2 for both Fe and FeO varied within $\pm 10\%$ of 0.015 \AA^2 . For this reason, and in order to use the limited information content of the data most effectively, the values of σ^2 for both Fe and FeO were set to 0.015 \AA^2 and the passive electron reduction factor (S_0^2) was fixed at 1. This held the number of fitting parameters low enough to extract reliable numbers for bond distances and amounts of Fe(II) present in the nanoparticle samples. For all three

samples, multiple k-weight (1,2,3) fitting maximized the use of the data. To produce a fit with a reasonable R factor the background for C12E6-11to1 was included in order to account for the density around 1 Å which is somewhat larger and likely unphysical. The fitting results crucial for our investigation are summarized in Table 5.4.

Sample Name	%FeO	Fe-Fe bond Distance (Å)	Fe-O bond Distance (Å)
PD-13to1	49(5)	2.50(0.03)	2.01(0.04)
PD-35to1	39(7)	2.51(0.03)	1.94(0.06)
C12E6-11to1	45(12)	2.51(0.01)	1.94(0.06)

Table 5.4: EXAFS fitting results.

The amount of FeO determined by fitting the EXAFS data is consistent (within experimental error) with the total amount of Fe(II) species found through LCF of the XANES data. The Fe-Fe bond distances for samples PD-13to1, PD-35to1, and C12E6-11to1 are expanded by approximately 2%. The percent expansion was found by comparing to the Fe-Fe nearest neighbor distance determined by fitting the EXAFS data for the Fe Foil reference. For iron foil, the Fe-Fe distance was found to be 2.46 ± 0.02 Å. A plot of the Fe foil EXAFS data, Fourier transform of the EXAFS data, and fit to this data can be found in Figure 5.22. The Fe-Fe bond distance for sample C12E6-1to1 (not shown) was found to be slightly less than bulk. However, due to the low percentage of Fe(0) in this sample, the Fe-Fe nearest neighbor distance value calculated during fitting is unreliable. The Fe-O bond distances do not show any significant trend. However, FeO is not a completely idealized model for this system because of the presence of organic ligands at the particles' surface. Additional EXAFS fitting results, including values of

E_0 (energy origin of the photoelectron) for both Fe and FeO and R factors, can be found in Table 5.5.

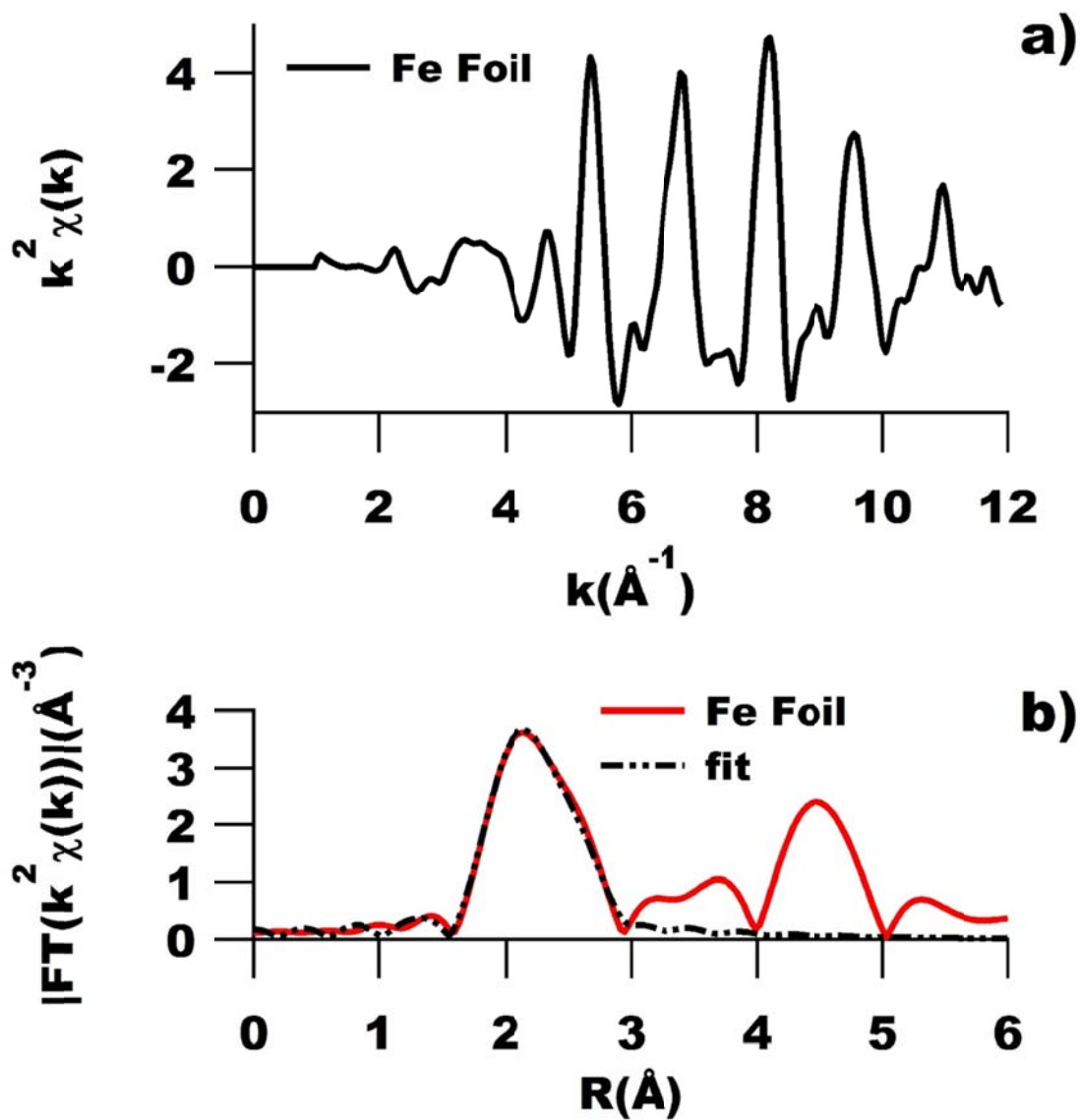


Figure 5.22: EXAFS spectra (multiplied by k^2) of Fe foil (a) and plot of the Fourier transform of the EXAFS spectra of Fe foil (b). In (b) the fit to the Fe foil data is plotted as a dashed line.

Sample Name	E_0 (eV), Fe	E_0 (eV), FeO	R factor
PD-13to1	7113(3)	7120(3)	0.010
PD-35to1	7113(3)	7118(4)	0.024
C12E6-1to1	7112 (held fixed)	7122(1)	0.008
C12E6-11to1	7112 (held fixed)	7114(6)	0.010

Table 5.5: Additional EXAFS fitting results not included in Table 5.4. E_0 for both Fe and FeO theoretical standards was 7112 eV prior to fitting. R factor provides a measure of closeness of fit with a value of zero indicating a perfect match between data and fit.

Chapter 6

Conclusion

In conclusion, we have shown that chemically-synthesized iron nanoparticles with two different ligands (2,4-pentanedione and hexaethylene glycol monododecylether) can be synthesized with σ_{sat} values only slightly less than bulk iron, yet have anisotropies more than an order of magnitude greater than bulk iron. This anomalous magnetocrystalline anisotropy remains constant with respect to particle size. Two different synchrotron based X-ray characterization techniques (PDF analysis of XRD and XAFS) show a 2-3% expansion in the crystalline lattice, which also remains constant with respect to particle size.

Both XANES and EXAFS analysis of iron nanoparticles synthesized with PD and C12E6 surfactants have shown that ligands often considered as weakly binding interact strongly enough with the nanoparticle surface to produce several layers of Fe(II) species. The amount of Fe(II) present scales with the surface to volume ratio of the nanoparticles and can play a significant role in the particles' magnetic properties, particularly by reducing apparent σ_{sat} values. Fig. 6.1 displays a scaled representation of the core/shell structure observed in particles synthesized with both PD and C12E6. In the case of PD, the ligand was shown to interact with the Fe surface much more strongly than previously thought, forming a Fe(acac) like species. Additionally, a 2% expansion of the crystalline lattice of the Fe(0) core for these particles (with both PD and C12E6 ligands) has been observed using EXAFS. The expansion observed in the EXAFS data is consistent with results seen in the PDF analysis of high energy XRD data, which observed a 3% expansion in the iron nanoparticles' crystalline lattice. Results from the PDF analysis

also show that these particles have a distorted bcc-type structure and a correlation length shorter than their diameters.

The expansion or contraction of a material's crystalline lattice (when compared to bulk materials) is not without precedence, particularly in nanomaterials studied with either EXAFS or PDF. These newer techniques have enabled the measurement of subtle (on the order of a few percent or less) changes in lattice parameters that could not be observed previously. For example, a 1 % lattice volume expansion was observed in NiO nanocrystals while Au nanoparticles were reported to have a slightly smaller lattice parameter than bulk Au.[115, 116]

The possibility of any systematic errors affecting the results presented here, particularly the increased, yet constant, magnetocrystalline anisotropy values has been thoroughly considered. Particle diameter measurements larger than the values reported would have only underestimated the value of K_1 . In order for the blocking temperatures (and therefore values of K_1) of the nanoparticles studied to line up with the curve calculated for bulk iron (see Figure 4.8) it would be necessary for their diameters to double. Systematic errors in temperature would have to be far greater (off by a factor of 8) for the measured values in Figure 4.8 to line up with the theoretical curve. For the largest particles, their measured blocking temperature would have to be reduced by 100 K to line up with the theoretical curve. Additionally, to ensure the accuracy of the magnetometry data, the temperature control, thermometry, and magnetic response of the magnetometer are thoroughly calibrated at regular intervals. The other physical property observed to remain constant with respect to particle size is the lattice expansion of the nanoparticles. This lattice expansion was observed using multiple techniques (PDF and XAFS) on different samples synthesized by different chemists (using the same protocol)

multiple years apart and with two different organic ligands. The same can be said of the samples and measurements of the magnetocrystalline anisotropy.

An equally thorough amount of care was taken to ensure a slow oxidation of the iron nanoparticles did not affect the experimental results. It is true that discrete nanoparticles will oxidize under high vacuum conditions. In fact, a monolayer of iron oxide has been shown to form with 1×10^{-6} Torr sec exposure of oxygen and stepped surfaces have been shown to be even more susceptible to oxidation.[79, 80] For this reason, TEM measurements were not used to determine the amount of oxidation present in as synthesized particles. In fact, we have observed the growth of an oxide layer over time inside the TEM. Instead of the measurement of discrete particles, we only relied on the measurement of a large ensemble of particles handled and measured using air-free techniques. When the particles are sealed inside of a glass vessel (NMR tube, capillary tube) a very small percentage of the particles may be oxidized due to the presence of trace oxygen impurity but their ensemble properties are not affected (due to a very large total surface area for the ensemble). The exact same magnetic properties have been measured in an iron nanoparticle sample sealed in an NMR tube and measured both immediately after synthesis and three years later. Similarly, the EXAFS measurements completed at APS showed no change in the sample's structural properties over the course of a 15 hr. data collection period. The practice of sealing ensembles of α -Fe nanoparticles in a glass vessel under a controlled atmosphere for Mossbauer spectroscopy has been demonstrated previously, where the Mossbauer spectra measured were characteristic of α -Fe.[117]

The lattice expansion observed in these iron nanoparticle samples could further impact the particles' magnetic properties, affecting both their σ_{sat} and magnetocrystalline anisotropy. The observed lattice expansion is believed to be at least in part responsible

for the large magnetocrystalline anisotropies in these particles. However, little ab initio modeling has been done to study how changes in the lattice constant of bcc iron could affect magnetocrystalline anisotropy. One paper by Ostanin, *et al.* does predict a very sharp increase in magnetocrystalline anisotropy as the lattice constant increases from its equilibrium value.[118]

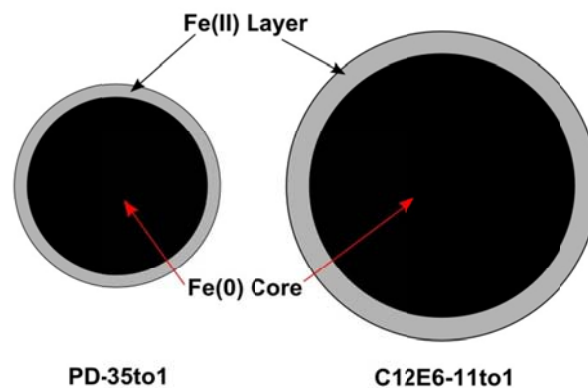


Figure 6.1: Scaled representation of the core/shell structure in samples PD-35to1 and C12E6-11to1.

Ab initio calculations may be the best way to determine whether the observed expansion in Fe-Fe distances and substantial structural disorder explain the anomalously high anisotropy measured. Absent this modeling, we cannot definitively state that this is the case, but the evidence points to this conclusion. Other possible explanations including dipolar interactions and surface anisotropy do not appear to be the dominant causes of the enhanced anisotropy. Both effects are strongly size dependent, and are inconsistent with our observation of size-independent anisotropy. Surface anisotropy is enhanced in smaller particles due to the high surface to volume ratio. Conversely, dipolar interactions are very strongly dependent on particle size, with the strongest effects seen in large particles and concentrated samples.[119] Additionally, the Vogel-Fulcher law fits

show a reasonable accounting for the physical effects of dipolar interactions when determining the values of K_1 for these particles.

The structural changes of the iron nanoparticles seen here are reminiscent of a recent publication by Margeat *et al.* that attributed high anisotropy in iron nanoparticles to a polytetrahedral structure.[29] While this system is qualitatively similar, the K_1 reported is considerably lower than seen in the current study ($5.2 \times 10^5 \text{ J/m}^3$ vs. $1.9 \times 10^6 \text{ J/m}^3$). It is tempting to assume the structure observed here must similarly be polytetrahedral, but our PDF data was reproduced well by a distorted bcc model, and our pair distribution function bears no resemblance to the one published by Margeat *et al.* Still, there is precedent for high anisotropy in iron nanoparticles being caused by structural changes.

One potential cause of the size independent lattice expansion and magnetocrystalline anisotropy could be the incorporation carbon atoms into the nanoparticles during the growth process. Although a vigorous flow of inert gas is used to remove the CO gas formed during the decomposition of the $\text{Fe}(\text{CO})_5$ precursor, the possibility does exist for carbon atoms to become incorporated into the Fe crystalline structure. Since the X-ray analysis of these particles does reveal a bcc Fe structure, C could only be present at very low levels ($< 0.1\%$). This low Z element would be essentially impossible to detect at these levels, particularly against such a large background of organic ligands and solvent. A series of experiments confirming or refuting the presence of C in these iron nanoparticles could be the subject of a chemistry based follow on study. One Danish group reported the formation of particles with the magnetic properties of an iron-carbon alloy (and therefore a much higher C concentration than possible in this study) using a $\text{Fe}(\text{CO})_5$ precursor but synthesized under much

different conditions.[120] The incorporation of C into the Fe lattice could be expected to increase the magnetocrystalline anisotropy.[121]

The ligand/surface interactions observed are most likely responsible for the Fe particles' lower σ_{sat} values than bulk iron since an expanded Fe-Fe distance should lead to a higher magnetic moment per iron atom.[36] Since the smaller particles have been observed to have lower σ_{sat} values than the larger particles, it is probable that quenching of the surface magnetism is causing the decrease in σ_{sat} . Both PD and C12E6 were chosen as ligands for iron nanoparticles because they were believed to be less strongly interacting with the iron surface than other ligands used in the literature. This is most likely still the case, however, they still have a significant impact on the magnetic properties of the iron nanoparticles' surface. Further work must still be done to identify ligands that will make iron nanoparticle magnetization equivalent to that found in bulk iron or even enhanced compared to bulk, as demonstrated in surfactant free nanoparticle beams.

It is hoped that this work can encourage and be the basis for further research into the effects of synthesis conditions and ligand choice on the properties of magnetic nanoparticles, particularly iron nanoparticles. Ab initio modeling of the effect of changes in lattice spacing and disorder on the magnetocrystalline anisotropy of iron nanoparticles through spin-polarized DFT could build upon the experimental results reported here. A more robust understanding of the relationship between crystalline structure and magnetocrystalline anisotropy could lead to the ability to tailor the anisotropy of nanoparticles for the desired application (e.g. magnetically hard particles for memory storage or permanent magnets and magnetically soft particles for transformer cores). The ability to fine tune the magnetic response of nanoparticles is a very attractive proposition. Although iron nanoparticles with magnetizations equal to or exceeding bulk iron were not

achieved through this research effort, our understanding of the interaction between the iron surface and weakly interacting ligands has been advanced and particles with magnetizations approaching that of bulk iron have been achieved. It is hoped that the search for ligands which could offer improved magnetizations will continue, as enhanced magnetic moment nanoparticles could benefit a number of applications.

Bibliography

- [1] S.D. Bader, Rev. Mod. Phys. **78**, 1 (2006).
- [2] D.E. Speliotis, J. Magn. Magn. Mater. **193**, 29 (1999).
- [3] B.D. Terris, T. Thomson, J. Phys. D: Appl. Phys. **38**, R199 (2005).
- [4] R.A. McCurrie, *Ferromagnetic Materials Structure and Properties*, Academic Press, London, 1994.
- [5] D.L. Huber, E.L. Venturini, J.E. Martin, P.P. Provencio, R.J. Patel, J. Magn. Magn. Mater. **278**, 311 (2004).
- [6] J.L. Dormann, D. Fiorani, E. Tronc, Adv. Chem. Phys. **98**, 283 (1997).
- [7] M.C. Bautista, O. Bomati-Miguel, X. Zhao, M.P. Morales, T. Gonzalez-Carreno, R.P. de Alejo, J. Ruiz-Cabello, S. Veintemillas-Verdaguer, Nanotechnology **15**, S154 (2004).
- [8] E.R. Flynn, H.C. Bryant, Phys. Med. Biol. **50**, 1273 (2005).
- [9] R.K. Gilchrist, R. Medal, W.D. Shorey, R.C. Hanselman, J.C. Parrott, C.B. Taylor, Annals of Surgery **146**, 596 (1957).
- [10] M. Gonzales, K.M. Krishnan, J. Magn. Magn. Mater. **293**, 265 (2005).
- [11] A. Hoffman, Chung, S. H., Bader, S. D., Makowski, L. Chen, L., *Biomedical Applications of Nanotechnology*, Wiley, New York, 2006.
- [12] Q.A. Pankhurst, J. Connolly, S.K. Jones, J. Dobson, J. Phys. D: Appl. Phys. **36**, R167 (2003).
- [13] N.L. Adolphi, D.L. Huber, H.C. Bryant, T.C. Monson, D.L. Fegan, J. Lim, J.E. Trujillo, T.E. Tessier, D.M. Lovato, K.S. Butler, P.P. Provencio, H.J. Hathaway, S.A. Majetich, R.S. Larson, E.R. Flynn, Phys. Med. Biol. **55**, 5985 (2010).
- [14] N.L. Adolphi, D.L. Huber, J.E. Jaetao, H.C. Bryant, D.M. Lovato, D.L. Fegan, E.L. Venturini, T.C. Monson, T.E. Tessier, H.J. Hathaway, C. Bergemann, R.S. Larson, E.R. Flynn, J. Magn. Magn. Mater. **321**, 1459 (2009).

- [15] H.C. Bryant, N.L. Adolphi, D.L. Huber, D.L. Fegan, T.C. Monson, T.E. Tessier, E.R. Flynn, *J. Magn. Magn. Mater.* **323**, 767 (2011).
- [16] H. Hathaway, K. Butler, N. Adolphi, D. Lovato, R. Belfon, D. Fegan, T. Monson, J. Trujillo, T. Tessier, H. Bryant, D. Huber, R. Larson, E. Flynn, *Breast Cancer Research* **13**, R108 (2011).
- [17] R.M. Taylor, D.L. Huber, T.C. Monson, A.M.S. Ali, M. Bisoffi, L.O. Sillerud, *J. Nanopart. Res.* **13**, 4717 (2011).
- [18] B.D. Cullity, *Introduction to Magnetic Materials*, 2nd ed., John Wiley & Sons, Inc., Hoboken, 2009.
- [19] A.H. Morrish, *The Physical Principles of Magnetism*, IEEE Press, New York, 1972.
- [20] R.M. Bozorth, *Ferromagnetism*, D. Van Nostrand Company, Inc., Princeton, 1961.
- [21] R.L. Fink, G.A. Mulhollan, A.B. Andrews, J.L. Erskine, G.K. Walters, *J. Appl. Phys.* **69**, 4986 (1991).
- [22] X.L. Zhou, C. Yoon, J.M. White, *Surf. Sci.* **203**, 53 (1988).
- [23] N.A.D. Burke, H.D.H. Stover, F.P. Dawson, *Chem. Mater.* **14**, 4752 (2002).
- [24] D. Farrell, S.A. Majetich, J.P. Wilcoxon, *J. Phys. Chem. B* **107**, 11022 (2003).
- [25] D.L. Huber, *Small* **1**, 482 (2005).
- [26] G. Kataby, M. Cojocaru, R. Prozorov, A. Gedanken, *Langmuir* **15**, 1703 (1999).
- [27] G. Kataby, Y. Koltypin, A. Ulman, I. Felner, A. Gedanken, *Appl. Surf. Sci.* **201**, 191 (2002).
- [28] T. Smith, D. Wychick, *J. Phys. Chem.* **84**, 1621 (1980).
- [29] O. Margeat, F. Dumestre, C. Amiens, B. Chaudret, P. Lecante, M. Respaud, *Prog. Solid State Chem.* **33**, 71 (2005).
- [30] J.P. Chen, C.M. Sorensen, K.J. Klabunde, G.C. Hadjipanayis, *Phys Rev B* **51**, 11527 (1995).
- [31] N. Cordente, M. Respaud, F. Senocq, M.J. Casanove, C. Amiens, B. Chaudret, *Nano Lett.* **1**, 565 (2001).

- [32] F. Dumestre, B. Chaudret, C. Amiens, M.C. Fromen, M.J. Casanove, P. Renaud, P. Zurcher, *Angewandte Chemie-International Edition* **41**, 4286 (2002).
- [33] O. Margeat, D. Ciuculescu, P. Lecante, M. Respaud, C. Amiens, B. Chaudret, *Small* **3**, 451 (2007).
- [34] J.P. Wilcoxon, E.L. Venturini, P. Provencio, *Phys Rev B* **69**, (2004).
- [35] S.E. Apsel, J.W. Emmert, J. Deng, L.A. Bloomfield, *Phys. Rev. Lett.* **76**, 1441 (1996).
- [36] I.M.L. Billas, A. Chatelain, W.A. deHeer, *J. Magn. Magn. Mater.* **168**, 64 (1997).
- [37] J.P. Bucher, D.C. Douglass, L.A. Bloomfield, *Phys. Rev. Lett.* **66**, 3052 (1991).
- [38] K.J. Klabunde, *Introduction to Nanotechnology*, in: K. Klabunde (Ed.) *Nanoscale Materials in Chemistry*, Wiley Interscience, New York, 2001, pp. 1.
- [39] G.B. Sergeev, *Usp. Khim.* **70**, 915 (2001).
- [40] R. Goldfarb, F. Fickett, *Units for Magnetic Properties—NBS special publication 696*, National Bureau of Standards, U.S. Government Printing Office, 1985.
- [41] P. Weiss, *C.R. Acad. Sci.* **143**, 1136 (1906).
- [42] H.J. Williams, R.M. Bozorth, W. Shockley, *Phys. Rev.* **75**, 155 (1949).
- [43] F. Bloch, *Z. Phys.* **74**, 295 (1932).
- [44] J. Frenkel, J. Dorfman, *Nature* **126**, 274 (1930).
- [45] W.C. Elmore, *Phys. Rev.* **54**, 1092 (1938).
- [46] C. Kittel, *Phys. Rev.* **70**, 965 (1946).
- [47] J. Beeteson, *Vizimag* 3.03. 2004, www.vizimag.com.
- [48] L. Neel, *C.R. Acad. Sci.* **224**, 1488 (1947).
- [49] E.C. Stoner, E.P. Wohlfarth, *Philos Trans R Soc Ser-A* **240**, 599 (1948).
- [50] W.F. Brown, *Phys. Rev.* **130**, 1677 (1963).
- [51] W.F. Brown, *PHYSICA B&C* **86**, 1423 (1977).
- [52] C. Bean, J. Livingston, *J. Appl. Phys.* **30**, 120S (1959).

- [53] C.P. Bean, J. Appl. Phys. **26**, 1381 (1955).
- [54] C.P. Bean, I.S. Jacobs, J. Appl. Phys. **27**, 1448 (1956).
- [55] I. Jacobs, C. Bean, *Fine Particles, Thin Films and Exchange Anisotropy (Effects of Finite Dimensions and Interfaces on the Basic Properties of Ferromagnets)*, in: G.T. Rado, H. Suhl (Eds.) *Magnetism*, Academic Press, New York and London, 1963, pp. 271.
- [56] A. Aharoni, *Introduction to the Theory of Ferromagnetism*, 2nd ed., Oxford University Press, Oxford, 2007.
- [57] S. Chikazum, *Physics of Ferromagnetism*, Oxford University Press, Oxford, 1997.
- [58] H.J. Elmers, G. Liu, U. Gradmann, Phys. Rev. Lett. **63**, 566 (1989).
- [59] J.A.C. Bland, R.D. Bateson, B. Heinrich, Z. Celinski, H.J. Lauter, J. Magn. Magn. Mater. **104**, 1909 (1992).
- [60] G. Lugert, G. Bayreuther, S. Lehner, G. Gruber, P. Bruno, Magnetic Order and Structure of Ultrathin Films and Multilayers, in: T. Suzuki, Y. Sugita, B. Clemens, K. Ouchi, D.E. Laughlin (Eds.) *Materials Research Society, Magnetic Materials : Microstructure and Properties Symposium*, 1991, pp. 97.
- [61] C.L. Wooten, J. Chen, G.A. Mulhollan, J.L. Erskine, J.T. Markert, Phys Rev B **49**, 10023 (1994).
- [62] O. Eriksson, A.M. Boring, R.C. Albers, G.W. Fernando, B.R. Cooper, Phys Rev B **45**, 2868 (1992).
- [63] A.J. Freeman, R.Q. Wu, J. Magn. Magn. Mater. **100**, 497 (1991).
- [64] C.S. Wang, A.J. Freeman, Phys Rev B **24**, 4364 (1981).
- [65] R.Q. Wu, A.J. Freeman, Phys Rev B **47**, 3904 (1993).
- [66] M.R. Press, F. Liu, S.N. Khanna, P. Jena, Phys Rev B **40**, 399 (1989).
- [67] M.L. Tiago, Y.K. Zhou, M.M.G. Alemany, Y. Saad, J.R. Chelikowsky, Phys. Rev. Lett. **97**, (2006).
- [68] C.Y. Yang, K.H. Johnson, D.R. Salahub, J. Kaspar, R.P. Messmer, Phys Rev B **24**, 5673 (1981).

- [69] C. Binns, M. Maher, Q. Pankhurst, D. Kechrakos, K. Trohidou, Phys Rev B **66**, 184413 (2002).
- [70] C. Binns, K.N. Trohidou, J. Bansmann, S.H. Baker, J.A. Blackman, J.P. Bucher, D. Kechrakos, A. Kleibert, S. Louch, K.H. Meiwes-Broer, G.M. Pastor, A. Perez, Y. Xie, Journal of Physics D-Applied Physics **38**, R357 (2005).
- [71] J. Bansmann, S.H. Baker, C. Binns, J.A. Blackman, J.P. Bucher, J. Dorantes-Davila, V. Dupuis, L. Favre, D. Kechrakos, A. Kleibert, K.H. Meiwes-Broer, G.M. Pastor, A. Perez, O. Toulemonde, K.N. Trohidou, J. Tuillon, Y. Xie, Surf. Sci. Rep. **56**, 189 (2005).
- [72] H.A. Durr, S.S. Dhesi, E. Dudzik, D. Knabben, G. van der Laan, J.B. Goedkoop, F.U. Hillebrecht, Phys Rev B **59**, R701 (1999).
- [73] K.W. Edmonds, C. Binns, S.H. Baker, S.C. Thornton, C. Norris, J.B. Goedkoop, M. Finazzi, N.B. Brookes, Phys Rev B **60**, 472 (1999).
- [74] G.S. Coyne, *The Laboratory Companion*, John Wiley & Sons, Inc., New York, 1997.
- [75] Innovative Technology, Inc., PureLab HE 2GB Glovebox System, in: www.gloveboxes.com.
- [76] C.H. Griffiths, M.P. Ohoro, T.W. Smith, J. Appl. Phys. **50**, 7108 (1979).
- [77] K.D. Humfeld, A.K. Giri, S.A. Majetich, E.L. Venturini, Ieee Transactions on Magnetics **37**, 2194 (2001).
- [78] K.S. Suslick, M.M. Fang, T. Hyeon, J. Am. Chem. Soc. **118**, 11960 (1996).
- [79] H.C. Mireles, J.L. Erskine, J. Appl. Phys. **93**, 7139 (2003).
- [80] R.L. Fink, G.A. Mulhollan, A.B. Andrews, J.L. Erskine, G.K. Walters, Phys Rev B **45**, 9824 (1992).
- [81] J.M.D. Coey, *Magnetism and Magnetic Materials*, Cambridge University Press, Cambridge, 2010.
- [82] M. McElfresh, *Fundamentals of Magnetism and Magnetic Measurements*, Quantum Design, Inc., 1994.
- [83] ASTM E394-00, *Standard Test Method for Iron in Trace Quantities Using the 1,10-Phenanthroline Method*, in: Annual Book of ASTM standards, 2000.

- [84] D.R. Lide, *CRC Handbook of Chemistry and Physics*, 82nd ed., CRC Press, Boca Raton, FL, 2001.
- [85] J. Souletie, J.L. Tholence, *Phys Rev B* **32**, 516 (1985).
- [86] V.B. Barbeta, R.F. Jardim, P.K. Kiyohara, F.B. Effenberger, L.M. Rossi, *J. Appl. Phys.* **107**, (2010).
- [87] M.F. Hansen, P.E. Jonsson, P. Nordblad, P. Svedlindh, *J Phys-Condens Mat* **14**, 4901 (2002).
- [88] L. Neel, *C.R. Acad. Sci.* **228**, 664 (1949).
- [89] J.L. Dormann, L. Bessais, D. Fiorani, *J Phys C Solid State* **21**, 2015 (1988).
- [90] J.A. Mydosh, *Spin Glasses: An Experimental Introduction*, Taylor & Francis, London, 1993.
- [91] C. Djurberg, P. Svedlindh, P. Nordblad, M.F. Hansen, F. Bodker, S. Morup, *Phys. Rev. Lett.* **79**, 5154 (1997).
- [92] J. Stöhr, H.C. Siegmann, *Magnetism From Fundamentals to Nanoscale Dynamics*, Springer, Berlin, 2006.
- [93] Argonne National Laboratory, Advanced Photon Source, in: <http://www.aps.anl.gov>.
- [94] V. Petkov, Y. Peng, G. Williams, B.H. Huang, D. Tomalia, Y. Ren, *Phys Rev B* **72**, (2005).
- [95] T. Egami, S.J.L. Billinge, *Underneath the Bragg Peaks*, Pergamon Press, Amsterdam, 2003.
- [96] D.A. Keen, *J. Appl. Crystallogr.* **34**, 172 (2001).
- [97] G.G. Sumner, H.P. Klug, L.E. Alexander, *Acta Crystallographica* **17**, 732 (1964).
- [98] V. Petkov, *J. Appl. Crystallogr.* **22**, 387 (1989).
- [99] T. Proffen, S.J.L. Billinge, *J. Appl. Crystallogr.* **32**, 572 (1999).
- [100] M. Newville, *Fundamentals of XAFS*, Consortium for Advanced Radiation Sources, University of Chicago, 2004.
- [101] D.E. Sayers, E.A. Stern, F.W. Lytle, *Phys. Rev. Lett.* **27**, 1204 (1971).

- [102] S.D. Kelly, D. Hesterberg, B. Ravel, *Analysis of Soils and Minerals Using X-ray Absorption Spectroscopy*, in: A.L. Ulery, L.R. Drees (Eds.) *Methods of Soil Analysis Part 5 - Mineralogical Methods*, Soil Science Society of America, Madison, 2008, pp. 387.
- [103] B. Ravel, E.E. Carpenter, V.G. Harris, *J. Appl. Phys.* **91**, 8195 (2002).
- [104] J.J. Rehr, R.C. Albers, *Rev. Mod. Phys.* **72**, 621 (2000).
- [105] E.A. Stern, *Phys Rev B* **10**, 3027 (1974).
- [106] E.A. Stern, *Contemp. Phys.* **19**, 289 (1978).
- [107] E.A. Stern, S.M. Heald, *Basic principles and applications of EXAFS*, in: E.E. Koch (Ed.) *Handbook of Synchrotron Radiation*, North-Holland, New York, 1983, pp. 995.
- [108] M. Newville, *Journal of Synchrotron Radiation* **8**, 322 (2001).
- [109] B. Ravel, M. Newville, *Journal of Synchrotron Radiation* **12**, 537 (2005).
- [110] L.C. Varanda, M. Jafelicci, P. Tartaj, K. O' Grady, T. Gonzalez-Carreno, M.P. Morales, T. Munoz, C.J. Serna, *J. Appl. Phys.* **92**, 2079 (2002).
- [111] M. Mikami, I. Nakagawa, Shimanou.T, *Spectrochimica Acta Part a-Molecular Spectroscopy A* **23**, 1037 (1967).
- [112] K. Nakamoto, A. Ruby, A.E. Martell, P.J. McCarthy, *J. Am. Chem. Soc.* **83**, 1066 (1961).
- [113] S.N. Slabzhennikov, O.B. Ryabchenko, L.A. Kuarton, *Russian Journal of Coordination Chemistry* **29**, 484 (2003).
- [114] M. Newville, P. Livins, Y. Yacoby, J.J. Rehr, E.A. Stern, *Phys Rev B* **47**, 14126 (1993).
- [115] A. Anspoks, A. Kuzmin, A. Kalinko, J. Timoshenko, *Solid State Commun.* **150**, 2270 (2010).
- [116] K. Page, T. Proffen, H. Terrones, M. Terrones, L. Lee, Y. Yang, S. Stemmer, R. Seshadri, A.K. Cheetham, *Chem. Phys. Lett.* **393**, 385 (2004).
- [117] F. Bodker, S. Morup, *Nuclear Instruments & Methods in Physics Research Section B-Beam Interactions with Materials and Atoms* **108**, 413 (1996).

- [118] S. Ostanin, J.B. Staunton, S.S.A. Razee, C. Demangeat, B. Ginatempo, E. Bruno, *Phys Rev B* **69**, (2004).
- [119] S.A. Majetich, M. Sachan, *Journal of Physics D-Applied Physics* **39**, R407 (2006).
- [120] J. Vanwonderghem, S. Morup, S.W. Charles, S. Wells, J. Villadsen, *Phys. Rev. Lett.* **55**, 410 (1985).
- [121] G. de Vries, D.W. van Geest, R. Gersdorf, G.W. Rathenau, *Physica* **25**, 1131 (1959).

Vita

Todd Monson was born in Philadelphia, Pennsylvania in 1975. He graduated from Rutherford High School in Panama City, Florida during 1993 and entered the U.S. Naval Academy in Annapolis, MD. Todd graduated with distinction from the Naval Academy with a B.S. in Physics in 1997 and cross commissioned into the United States Air Force. During more than seven years in the Air Force, Todd served on three different assignments. In his first assignment, he served as a research physicist at the Air Force Research Laboratory Munitions Directorate, Advanced Guidance Systems Division on Eglin Air Force Base, Florida. Next, Todd was sent to earn a master's degree from the University of Texas at Austin under the supervision of Dr. James Erskine (M.A. 2001 – Physics). Upon completion of his M.A., Todd served as an instructor in the U.S. Air Force Academy Physics Department. In 2005, Todd separated from the Air Force and took a position as member of the technical staff at Sandia National Labs in the Nanomaterials Sciences Department, where he remains today.

Permanent address: 1127 Narcisco St. NE, Albuquerque, NM 87112

This dissertation was typeset by the author.